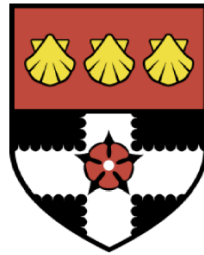


THE UNIVERSITY OF READING



The predictability of convective storms
over the ocean

Peter William Lean

A thesis submitted for the degree of Doctor of Philosophy

Department of Meteorology

April 2006

Declaration

I confirm that this is my own work and the use of all material from other sources has been properly and fully acknowledged.

Peter Lean

Abstract

The predictability of individual convective storms over the mid-latitude ocean is investigated by quantifying the divergence of pairs of perturbed forecasts in a cloud-resolving model. The Met Office non-hydrostatic Unified Model is used in an idealised configuration to simulate moist convection initiating under homogeneous destabilisation. All convection is represented explicitly since a convective parameterisation scheme is not used.

The growth of potential temperature perturbations at a single height is quantified as a function of time and spatial scale. The perturbations are found to grow in two distinct stages. Firstly, changes in the regime diagnosed by the boundary layer parameterisation scheme lead to rapid but limited perturbation growth before growth by convective instability becomes dominant. Both error growth mechanisms are found to contribute independently to the total error growth in the forecast.

The range of predictability in this perfect model framework is quantified for different spatial scales and initial condition error. The upper limit (provided by 0.002K perturbations) is shown to be around 200 minutes at scales of 10km. Initial condition perturbations of similar magnitude to those of typical analysis errors (i.e. of order 1K) were found to saturate almost immediately at all scales. The short time taken for the forecasts to become uncorrelated in all cases indicates that individual showers will always be unpredictable beyond approximately four hours.

The asymmetry in the evolution of initially equal and opposite perturbations highlights the non-linear nature of the growth, which could prove problematic for convective scale data assimilation and the design of ‘optimal’ perturbations for convective scale ensemble forecasting.

Acknowledgements

There are many who have contributed to the completion of this thesis. Thanks must first go to my supervisors, Suzanne Gray and Peter Clark. Sue kindly stepped in on day one of my PhD when George Craig left our shores. I am sincerely grateful for all her guidance and help, especially the time she took during maternity leave to read the chapters of this thesis and give me much needed feedback. Pete's many meteorological insights and discussions have proved invaluable to this work, even if it did sometimes take me a while to catch up!

This project would not have been possible without the sponsorship of the Natural Environment Research Council and the Met Office, and the use of the high performance computing facilities provided by Computer Services for Academic Research. Thanks, of course, must go to the little fluffy clouds for being so interesting. I would also like to recognise my thesis committee of David Stephenson and Alan Thorpe who always helped me to see the bigger picture and provided honest comments which gave me the motivation to dig deeper and get more from the results. Others in the department I must thank include Lois Steenman-Clark, Chang Gui-Wang, Bob Plant and all the people who have helped me (knowingly or not) and made the department such a pleasant place to work.

My family have, as always, been a source of continual encouragement. Finally, I would like to thank Una. Her support has got me through the last three and a bit years; thankyou.

Why is it that showers and even storms seem to come by chance,
so that many people think it quite natural to pray for rain or fine weather,
though they would consider it ridiculous to ask for an eclipse in prayer?

Jules Henri Poincaré (1912) : Science and Method

I hate quotations. Tell me what *you* know.

Ralph Waldo Emerson (1803 - 1882): diary, May 1849

Contents

1	Introduction	1
1.1	Motivation	1
1.2	Specification of the problem	2
1.3	Thesis aims	6
1.4	An introduction to deterministic ‘chaos’	6
1.5	Brief review of convective instability	13
1.6	Representation of convection within high resolution numerical models	19
1.7	On error growth in numerical weather forecasts	20
1.8	Thesis outline	33
2	Description of an idealised simulation of convection in a cold air outbreak	34
2.1	Description of the idealised Unified Model	34
2.2	Description of convective initiation in this case study	44
2.3	Description of the convective storms formed in this case study	51
2.4	Chapter Summary	56
3	Identification of the dominant perturbation growth mechanisms	58
3.1	Experiment methodology	58
3.2	Perturbation strategy	59
3.3	Overview of results from experiment MAIN	67
3.4	Chapter Summary	81
4	Attribution of two perturbation growth mechanisms to total perturbation growth	83
4.1	Perturbation growth variability between different storms	84
4.2	Formation of hypotheses to explain the storm-to-storm perturbation variability	87
4.3	Testing the hypotheses	88
4.4	Chapter summary	98
5	Quantification of the perturbation growth as a function of spatial scale	100
5.1	Fourier analysis of the perturbations	101
5.2	Overview of the perturbation growth curves	103

5.3	Quantification of the initial perturbation growth rate as a function of spatial scale	106
5.4	Super-exponential growth at large spatial scales	108
5.5	Quantification of the linearity of the perturbation evolution	111
5.6	Chapter Summary	115
6	Quantification of the error saturation timescale	117
6.1	Definition of error saturation	118
6.2	Definition of the initial amplitude of the perturbations	120
6.3	Methodology of experiment ‘AMP’	122
6.4	Results	124
6.5	Examination of saturated perturbation structure	131
6.6	Chapter summary	132
7	Conclusions and discussion of the implications	133
7.1	Conclusions	134
7.2	Discussion of the implications of the results	136
7.3	Discussion of the limitations of this work	138
7.4	Directions for future work	143
A	Linearisation of the logistic map	148
B	The linear theory of moist convection	150
B.1	Momentum equations	150
B.2	Linearising the momentum equations	152
B.3	Thermodynamic equation	154
B.4	Continuity equation	156
B.5	Describing the circulation	157
C	Summary of experiments	161
D	Understanding the meaning of τ	162

CHAPTER ONE

Introduction

1.1 Motivation

It has long been recognised that the evolutions of some deterministic systems exhibit extreme sensitive dependence on their initial states (Poincaré, 1914). The atmosphere is often cited as an example of such a system. Atmospheric instabilities cause errors in the initial conditions upon which a forecast is based to grow and eventually result in the forecast losing all skill after a finite time. Since the birth of numerical weather prediction (NWP) in the 1950s atmospheric predictability has been an active area of research. Quantitative knowledge of the rate at which forecasts lose accuracy is essential to understand where the errors come from and how to use the forecasts most appropriately.

The limitations of computational power have dictated the grid lengths and complexity of numerical models. Until recently, most operational forecast models have used grid lengths capable of representing only the synoptic and mesoscale structures explicitly. The effects of moist convection have usually been parameterised, taking advantage of the high statistical predictability of a large sample of convective cells. Therefore, nearly all predictability studies have concentrated on error growth in medium-range forecasts associated with barotropic and baroclinic instabilities. However, the steady increase in computer speed has allowed the grid length of some operational limited area forecast models to become sufficiently small to represent individual convective storms explicitly. Interest is now turning to the accuracy of explicit forecasts of convective features (and specifically their initiation) made by these models.

To date, little research has been done on the predictability of convective storms. A quantitative understanding of the nature of error growth in explicit forecasts of convective storms would be useful for convective scale data assimilation and ensemble forecasting. Moreover, the high precipitation rates, damaging hail, strong winds and turbulent flying conditions often associated with convective storms make information on the likely accuracy of forecasts of these features essential for suitable decision-making based on high resolution NWP output.

1.2 Specification of the problem

In this section the problem to be investigated in this thesis is posed.

1.2.1 Definition of ‘predictability’

In a thesis concerned with atmospheric predictability, it seems appropriate to first define exactly what is meant by the word **predictability**. Lorenz (1975) described two types of predictability:

- **Predictability of the first kind:** a measure of the extent to which the future state of a system may be known *explicitly* in advance.
- **Predictability of the second kind:** a measure of the extent to which the *statistics* of the future state may be known in advance.

The weather forecasting problem, where explicit predictions of the atmospheric state at a given time and location are attempted, is thus primarily concerned with the first kind of predictability of the atmosphere and is strongly dependent on knowledge of the initial state of the system. Climate forecasting however, is concerned with the second kind of predictability of the atmosphere, since attempts are made to predict statistics such as the change in annual mean temperatures or cyclone frequency caused by changing boundary conditions.

However, the difference between the two types of forecast is often not distinct. For example, a typical weather forecast may say ‘a band of raining clearing the London area at noon followed

by scattered light showers'. The forecast of the band of rain is explicit whereas only the statistics of the showers are forecast with no attempt made to predict the arrival and duration of individual showers.

The reason for this is that convective showers are understood to have a low predictability of the first kind, but a higher predictability of the second kind. This high predictability in the second sense of the word has allowed convective parameterisation schemes to predict (with reasonable accuracy) the mean effects that a large population of shower clouds within a grid box have on the larger scales, given the forcing imposed at the grid scale. However, as the resolution of numerical models increases and individual convective storms can be forecast explicitly, interest is turning to the first kind of predictability of convective storms. While their predictability in this sense is known to be low, little research has been done to quantify the level of this predictability.

This thesis aims to quantify the first kind of predictability of convective storms using a relatively high resolution mesoscale model in which convection is represented explicitly by the model dynamics allowing explicit forecasts of individual storms to be made. Such models are already starting to be used for operational forecasting of convective features. An appreciation of the factors leading to the growth of initial condition errors at convective scales in these models would be useful for those developing the models and using their forecasts.

1.2.2 Type of convection to be studied

Convective instability results in a broad spectrum of different features in the Earth's atmosphere. Small convective circulations occur in the unsaturated air above a candle, shallow moist convection confined to the boundary layer (cumulus humilis) is a common feature of a summer sky, rolls of convection occur frequently in boundary layers with a vertical shear of the horizontal wind, *deep moist convection* which reaches the tropopause (cumulonimbus) frequently produces showers; similarly large multicellular clusters of convective storms (Mesoscale Convective Systems) are often accompanied by thunder and lightning.

A single thesis cannot cover the nature of error growth associated with all of these different varieties of convective clouds, therefore only one type is investigated here. Mesoscale models with grid lengths in the range 1-10km are capable of representing only the largest convective clouds

explicitly and so **single cell cumulonimbus clouds** are selected for the purposes of this study. The larger Mesoscale Convective Systems were not chosen since their accurate simulation is more problematic (Weisman *et al.*, 1997) compared with the simpler single cell storms.

Particular interest lies in forecasts of the initiation of convective storms. Convective initiation can be divided into two categories. *Primary initiation* refers to the formation of the first convective clouds in a region due to some forcing mechanism. *Secondary initiation* occurs when an existing convective cloud triggers the initiation of new ‘daughter’ cells nearby. This usually occurs when a convective cloud develops a downdraught due to evaporative cooling which spreads out at the surface as a cold pool; new cells are then triggered along the convergence at the outflow boundary. As one of the first studies into error growth associated with convection it is appropriate to study the simplest case to begin with, i.e. **primary convective initiation**.

Many different mechanisms lead to the primary initiation of deep moist convection. Convergence lines, orography, upper level potential vorticity anomalies, land surface contrasts, gravity waves and cities have all been shown to trigger convective storms (e.g. Wilson and Schreiber (1986), Roberts (2000b) and Houze (1993)). However, in this thesis interest will focus on the simple scenario of **homogeneous destabilisation**, as is found in a ‘cold air outbreak’ over the ocean. In these situations cold air from the poles is advected equatorward over a relatively warm ocean surface which is slow to cool down. The imbalance between the advection of cold air aloft and the fluxes of heat and moisture from the surface into the boundary layer leads to conditional instability and convective initiation. Figure 1.1 is a satellite image of a typical example of a cold air outbreak over the ocean. These situations occur frequently in the cold sector of mid-latitude cyclones and the resulting convection is widespread. The case study to be investigated here will be an idealised representation of such a situation, free from the complexities of actual case studies where other effects may make the results harder to interpret.

Finally, it must be stressed that initial condition errors are not the only source of forecast error. Numerical models used to make forecasts are not perfect and so even given perfect initial conditions the forecast would diverge from the true evolution of the atmosphere with time. However, this thesis is concerned only with the contribution of initial condition errors to errors in the forecast and so a **perfect model framework** is adopted.

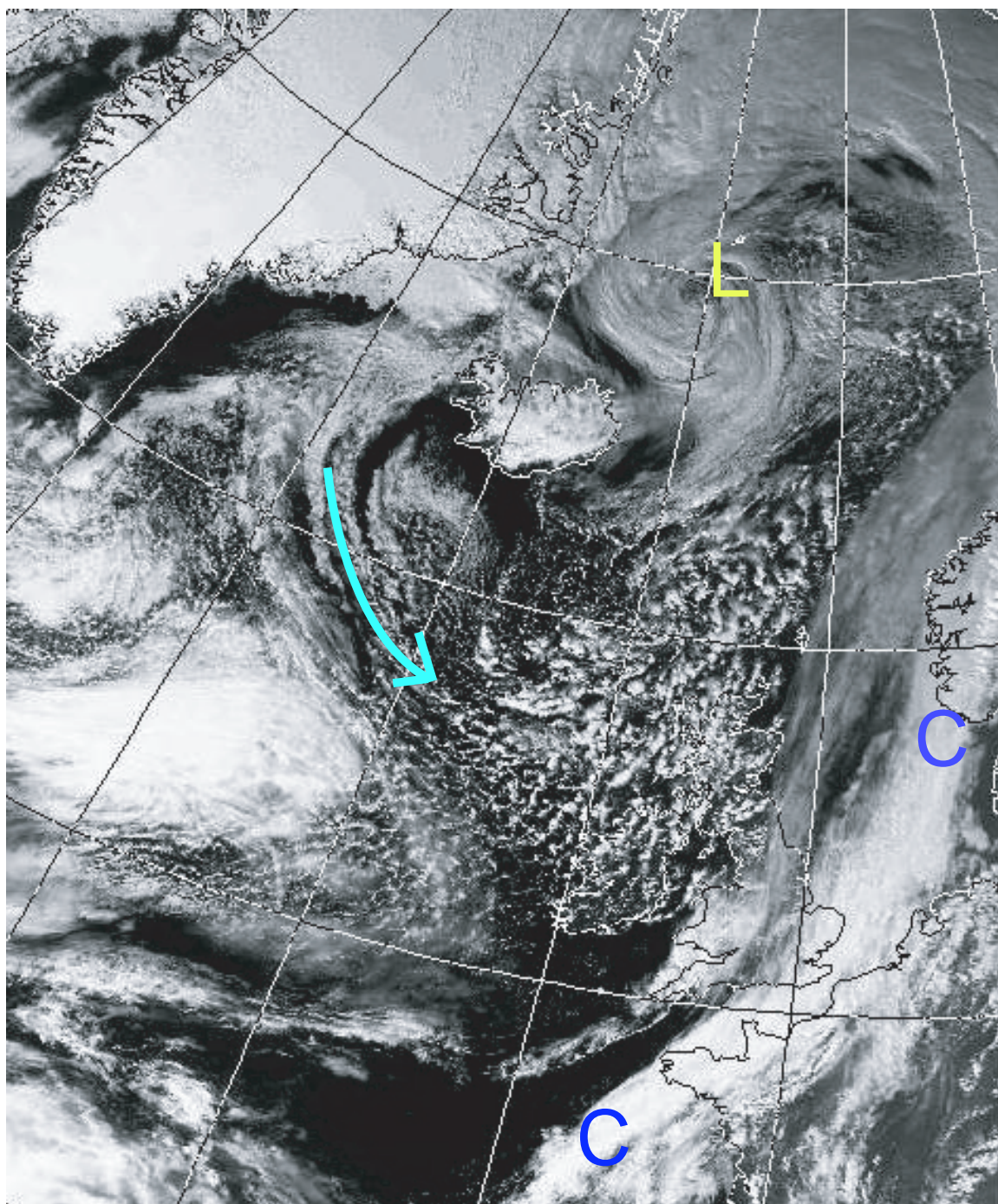


Figure 1.1: NOAA High Resolution Picture Transmission (HRPT) channel 1 image (visible light) on 04/04/05 at 14:49Z showing an example of a cold air outbreak. A cold front (marked *CC*) associated with a low pressure centre NE of Iceland (marked *L*) is moving southeastwards introducing cold polar maritime air over the relatively warm Atlantic ocean. Widespread deep convection can be seen in the cold sector. [Image courtesy of the NERC funded Dundee Satellite Receiving Station]

1.3 Thesis aims

This thesis investigates the first kind of predictability of convective showers through an examination of the growth of initial condition errors during the primary initiation of explicitly represented deep moist convection in idealised conditions of homogeneous destabilisation over the ocean in a mesoscale model.

Specifically, this study aims to:

1. understand the dominant *mechanisms* acting to grow initial condition errors in the first 3 hours of the forecast,
2. quantify the *growth rate* of initial condition errors in the forecast as a function of spatial scale,
3. quantify the timescale over which initial condition errors lead to forecasts with no skill (*error saturation timescale*) as a function of spatial scale and initial error amplitude.

This chapter provides some necessary background to the problem. Firstly, the subjects of predictability and chaotic systems are introduced. The importance of instability to the development of ‘chaotic’ behaviour is demonstrated with the aid of a simple non-linear deterministic system known as the logistic map. The theory of convective instability is then presented along with a linearisation of the governing equations to show the expected scale dependence of the growth rate of small perturbations. A literature review of research quantifying the growth of forecast errors, from the early studies to the state of the art, provides the context for this new research. Finally, an outline of the thesis is presented.

1.4 An introduction to deterministic ‘chaos’

The doctrine of *determinism* states that everything that happens in the future is determined by a necessary chain of causation i.e. the conditions in the present dictate all future events. Determinism has dominated scientific thought since Newton (1687) first set out the laws of motion. While research into quantum effects have shown that at the atomic level determinism doesn’t hold, at

the scales dealt with in everyday life these effects can be considered negligible (Guillemin, 2003, p.118). All deterministic systems are *in principle* completely predictable; given exact knowledge of the current state of the system it is possible to calculate the evolution of that system indefinitely. However, in the last one hundred years it has become generally accepted that certain deterministic systems are *in practice* unpredictable after a certain time, due to the sensitivity of the future evolution to their initial conditions and the inability to take perfect measurements of those conditions. These have become known popularly as *chaotic systems*. The atmosphere has widely been described as an example of such a system. It is however worth noting that many argue that the atmosphere cannot be described as deterministic due to known quantum effects and the influence of humans and animals with ‘free will’.

In this section a simple deterministic system is presented as an analogue of the atmosphere to demonstrate some fundamental properties of ‘chaotic’ systems.

1.4.1 Introducing the logistic map

The *logistic map* is the discrete form of a differential equation known as the logistic equation and is described by,

$$X_{n+1} = \alpha X_n (1 - X_n), \quad (1.1)$$

where α is a parameter of the system. It describes a discrete sequence of numbers, $X_0, X_1, X_2, X_3, \dots, X_n, \dots, X_N$ where each number in the sequence depends on the value preceding it, i.e. the logistic map is deterministic. For example, the sequence of numbers resulting from $\alpha = 0.5$ and $X_0 = 0.2$ is 0.2, 0.08, 0.0368, etc. Sequences resulting from starting values in the range, $0 \leq X_0 \leq 1$ and $0 \leq \alpha \leq 4.0$, are bounded between 0 and 1. Starting values outside that range are not bounded and, for the purposes of this study, will not be included. The sequence above tends towards zero; however, other regimes of behaviour are displayed for different values of the parameter α . Figure 1.2a shows the values of X_n in the range $1000 \leq n \leq 1500$ as a function of α with a starting value of $X_0 = 0.2$. The different regimes of behaviour can be broadly designated as follows:

1. Stationary regime ($0.00 \leq \alpha < 3.00$): all sequences tend towards a stationary solution.
2. Periodic regime ($3.00 \leq \alpha < 3.57$): all sequences tend towards a periodic solution except those that start on the stationary solution.
3. Non-periodic regime (existing in the range $3.57 \leq \alpha \leq 4.00$): sequences do not repeat unless the starting value is a periodic or stationary solution.

It must be noted that at some values of α within the range designated as the ‘non-periodic’ regime the system reverts to periodic behaviour, but the number of regime transitions are too numerous to note here.

The solutions oscillating between two points seen in the range $3.00 \leq \alpha \leq 3.45$ (at 3 significant figures precision), become periodic about four points between $3.45 \leq \alpha \leq 3.54$. At increasing values of α the number of points about which the solutions oscillates increases by a factor of two (8, 16, 32 etc.) until at $\alpha = 3.57$ the solution becomes *non-periodic*. This apparently random behaviour observed in many non-linear deterministic systems (including the atmosphere) led them to become known as *chaotic* systems. Further detail is revealed in Figure 1.2b where the intricacies of the bounded non-periodic solutions become apparent.

Strictly, the solutions in a computer where values of X_n are held to a finite level of precision can never be non-periodic since roundoff error will always eventually cause numbers to repeat and begin a periodic cycle. However, the high level of precision used in modern computers means that

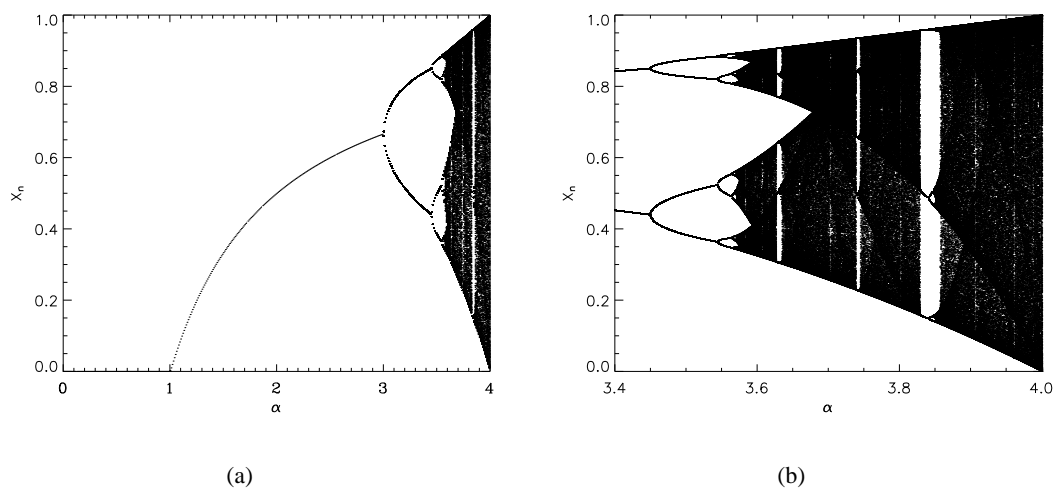


Figure 1.2: X_n for $1000 \leq n \leq 1500$ with different values of the parameter α with $X_0 = 0.2$. The chaotic regime can be seen in the range (a) $0 \leq \alpha \leq 4$ and (b) $3.65 \leq \alpha \leq 4.00$.

the repeat interval is likely to be so large that in practice the numerical solutions can be considered non-periodic. In these calculations, repeating solutions were not found after 10,000 iterations of the equation.

The stationary solutions can be found analytically. Let $X_{n+1} = X_n$ and substitute into equation 1.1. This gives:

$$\begin{aligned}\alpha X_n (1 - X_n) &= X_n \\ \alpha X_n - \alpha (X_n)^2 - X_n &= 0\end{aligned}$$

$$X_n = 0, 1 - \frac{1}{\alpha}.$$

e.g. $\alpha = 2$, $X_0 = \frac{1}{2}$, gives, $X_n = \frac{1}{2}, \frac{1}{2}, \frac{1}{2} \dots$

Similarly, solutions periodic about m points can be found which satisfy,

$$X_{n+m} = X_n$$

However, the non-periodic solutions can only be found through numerical integration.

1.4.2 Stability of the logistic map and error growth

The growth of initial condition errors in a system can be studied using so-called *identical twin* experiments. Two solutions are integrated forward in time from slightly different initial conditions using the same governing equations. The first of these solutions, X , represents the *truth* while the other, X^f , represents the *forecast*. The initial *perturbation*, δX_0 , added to the true initial state represents the *error* in the estimate of the initial conditions used to generate the forecast,

i.e. $X_0^f = X_0 + \delta X_0$. In this thesis the terms ‘error’ and ‘perturbation’ are used interchangeably depending on the context in which they occur. The evolution of the difference between the two solutions can then be thought of as representing the growth of errors in a forecast due to initial condition errors.

If the truth evolves as in equation 1.1, then the (error containing) forecast evolves as,

$$X_{n+1}^f = \alpha X_n^f (1 - X_n^f)$$

$$(X + \delta X)_{n+1} = \alpha (X + \delta X)_n (1 - (X + \delta X)_n).$$

As a measure of the ‘difference’ between two states, the *mean square difference* (MSD) or *root mean square difference* (RMS) are often used as they are both related to the distance in phase space between the two solutions. In this simple model with only one degree of freedom the RMS difference corresponds to the magnitude of the perturbation, $|\delta X|$.

The stability properties of the logistic map in the different regimes are illustrated in Figure 1.3. Figure 1.3a shows that in the ‘stationary’ regime two sequences starting from different values tended towards the same solution with increasing n . Conversely, Figure 1.3b shows that in the ‘non-periodic’ regime two sequences starting from values only 0.001 apart became increasingly different with time. Lorenz (1963) noted that non-periodic behaviour always occurred in unstable systems where the solutions were bounded. While periodic solutions do still exist in the ‘non-periodic’ regime, they can never be reached (unless X_0 equals the periodic solution) as the instability prevents any convergence. Therefore, **instability in a system with bounded solutions leads to non-periodic (chaotic) behaviour and poor predictability of the first kind.**

1.4.3 Linear theory of the logistic map

A linearisation of the non-linear map can be used to estimate the growth of perturbations that can be considered small. This is achieved by defining a background state, X^b , about which a small

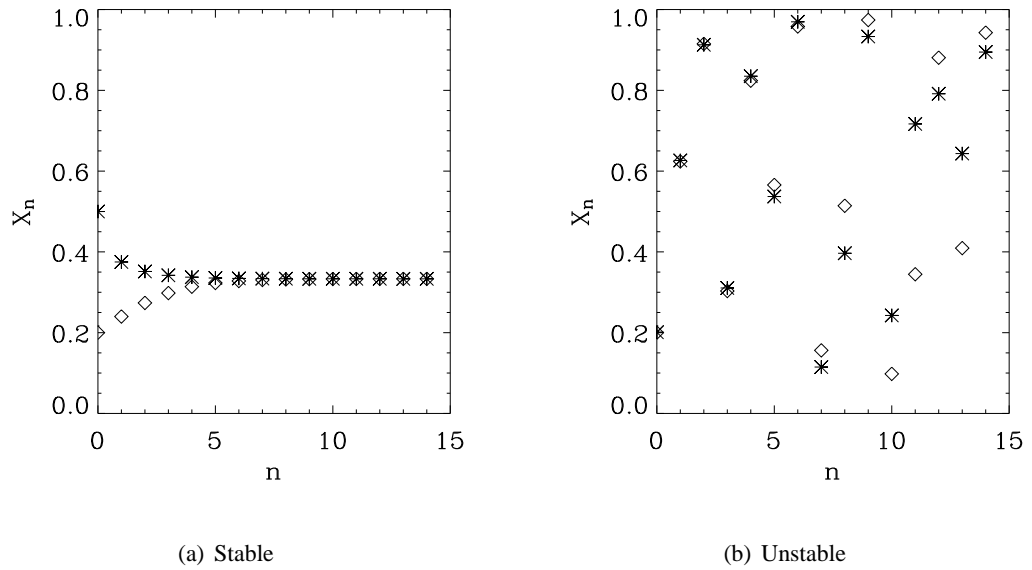


Figure 1.3: The sequences X_n (diamonds) and $(X + \delta X)_n$ (stars) for $0 \leq n \leq 15$ with $\alpha = 1.5$ and $X_0 = 0.2$ and $\delta X_0 = 0.3$ (left). The same for $\alpha = 3.9$ and $X_0 = 0.2$ and $\delta X_0 = 0.001$ (right).

perturbation, δX , grows. Hence,

$$X_{n+1}^b + \delta X_{n+1} = \alpha \left(X_n^b + \delta X_n \right) \left(1 - \left(X_n^b + \delta X_n \right) \right)$$

which after removing the small terms of order $(\delta X_n)^2$ gives,

$$\delta X_{n+1} = -\alpha \delta X_n \left(2X_n^b - 1 \right).$$

For a full derivation see Appendix A.

A comparison of the magnitude of the perturbations, $|\delta X|$, with those expected from linear theory is shown in Figure 1.4. Initially, the linear equations produce a good estimate of the actual perturbation growth. However, for $n \geq 40$ the error growth becomes non-linear in nature. Perturbation growth during the period when linear theory provides a good approximation of the observed error growth is known as the *linear regime*. During this time, the error growth is exponential.

In a sequence bounded within the range $X^{\min} \leq X_n \leq X^{\max}$, the error in the forecast of X_n can

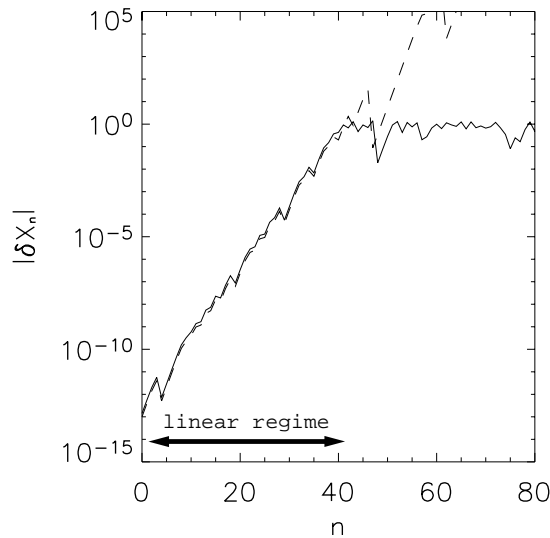


Figure 1.4: δX_n for full non-linear (solid) and linear (dashed) equations with $\delta X_0 = 1 \times 10^{-13}$.

be no larger than $(X^{max} - X^{min})$. This results in a limit above which the errors can become no larger. When errors reach this amplitude, non-linearities become significant and *error saturation* occurs. When forecast errors become this large, the forecast is as different from the truth as two random realisations are from each other, i.e. the prediction is no better than a guess.

1.4.4 Two kinds of predictability of the logistic map

It can be seen that in a system with bounded non-periodic behaviour, given observational error, accurate *explicit* predictions of the value of X to a desired level of accuracy are unachievable beyond a certain range, i.e. in the non-periodic regime, this system has a low predictability of the first kind. A forecast can be defined as ‘successful’ if the difference between the forecast state and the actual is state is below a prescribed threshold. The time over which an explicit prediction is successful can be called the *range of predictability*.

The range of predictability in this example may be increased by reducing the amplitude of the initial error. Indeed, the predictability may be extended to any desired range by reducing the initial error sufficiently.

However, the variation in the point density seen in Figure 1.2b illustrates that the probability of any given possible value occurring is not equal. The climate of the system can be defined as the probability density function of the possible system states. It becomes apparent that it is possible to

predict some information about the statistics of the future state of the system since some states are more likely to occur than others, i.e. in the non-periodic regime, this system does have a degree of predictability of the second kind.

1.5 Brief review of convective instability

1.5.1 Convective instability in the context of other atmospheric instabilities

The previous section showed that instability in a system with bounded solutions leads to ‘chaotic’ behaviour. The atmosphere exhibits a number of different instability mechanisms. Barotropic instability resulting from the interaction of edge waves along a vorticity gradient can allow small waves to amplify and dominate synoptic and planetary scale motions. Similarly, baroclinic instability can occur in the presence of a meridional temperature gradient in thermal wind balance, allowing waves to grow into mid-latitude cyclones. At smaller scales, instability mechanisms which have faster growth rate at small wavelengths dominate. Symmetric instability (which can be released in the absence of inertial and convective instability) is observed to be active at the mesoscale. Kelvin-Helmholtz (shear) instability can cause small waves to grow along a strong velocity gradient. Similarly, convective (static) instability occurs in an unsustainable vertical density gradient with faster growth rates at small scales. In general these hydrodynamical instabilities cause small perturbations to grow by extracting energy from their environment which in turn acts to remove the unsustainable gradients that created them.

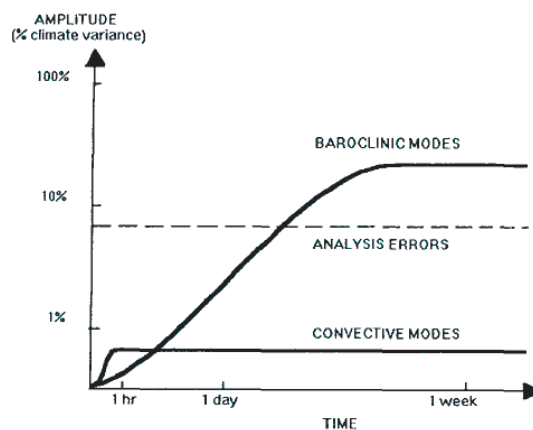


Figure 1.5: Schematic of the time evolution of the RMS amplitude of the convective and baroclinic modes. An indication of the analysis errors is also displayed. [Reproduced from Toth and Kalnay (1993)]

The small scale features associated with convective instability grow more rapidly, but saturate at a lower amplitude than the larger scale features associated with the barotropic and baroclinic instabilities, e.g. a thunderstorm grows more rapidly, but is ultimately smaller than a mid-latitude cyclone. Therefore, short-range forecasts tend to be dominated by errors associated with convective instability, before the effect of the larger scale instability mechanisms begin to dominate in the medium-range (see Figure 1.5). As will be seen in section 1.7, most previous predictability studies have concentrated on error growth in medium range forecasts associated with barotropic and baroclinic instabilities at synoptic scales. This thesis is concerned with convective instability and so concentrates on the first few hours of the forecast.

This section provides a brief outline of the theory of convection in dry air and in the presence of moisture, along with the definitions of terms used throughout this thesis. A linearisation of the governing equations is used to demonstrate that the growth rate of features by convective instability is faster if their spatial scale is smaller. This is followed by a discussion of the representation of convection in mesoscale models.

1.5.2 Definition of convection

Convection can be defined as the transfer of heat by the movement of a fluid. Usually in meteorology, the term convection is used to describe only the *vertical* heat transfer with the horizontal transfer known as *advection*. The strongest vertical motions in the atmosphere are associated with eddies which can be mechanically driven in conditions of shear instability (*forced convection*), or buoyancy driven in a convectively unstable environment (*free convection*). The *Richardson number*, Ri , describes the ratio of buoyant production to mechanical production of eddies. This thesis is concerned with buoyancy driven convective circulations.

1.5.3 Buoyancy

Buoyancy arises when lateral density contrasts exist in a fluid. A fluid can be considered in terms of a horizontally homogenous *environment* (or *basic state*) with density, $\bar{\rho}(z)$, and a perturbation from that environment described as a *parcel*, $\rho'(x, y, z)$. A net upward buoyant force is experienced by the parcel, equal to the weight of environmental fluid displaced by that parcel, since the pressure

of the environment acting on its lower surface is greater than that pushing down on its top surface. If an imbalance exists between the upward buoyant force and the downward force of gravity then the parcel undergoes acceleration. This acceleration due to the net force (often simply termed *buoyancy*, b'), is described by,

$$b' = g \frac{\bar{\rho} - \rho'}{\rho'}$$

where g is the acceleration due to gravity. Buoyancy provides the acceleration for convective instability. It is worth noting that a horizontally homogenous unstable environment at rest will not convect freely (without forced vertical displacement) as the buoyant acceleration is zero. Although, this condition of horizontal uniformity is never present in the atmosphere, it can occur in numerical simulations.

1.5.4 Dry static stability

The temperature, T , of a parcel of dry air displaced from its initial level (LI) will adjust adiabatically to the pressure, p , of its new environment according to the equation of state for an ideal gas,

$$p = \rho RT \tag{1.2}$$

where R is the gas constant. In parcel theory, it is assumed that the parcel does not affect the environment and so the system is linear. If after upward displacement a parcel is less dense than its surroundings then it will continue to accelerate upwards. This instability of a dry parcel to small vertical displacements is known as *dry static instability*. The static stability parameter, N^2 , of a dry atmosphere is defined,

$$N^2 = \frac{g}{\theta_0} \frac{\partial \bar{\theta}}{\partial z}$$

where the potential temperature of the air, θ , (i.e. the temperature that would result from an adiabatic adjustment to a pressure of 1000hPa) can be thought of as composed of the environment profile, $\bar{\theta}$, and a perturbation from that basic state (the parcel), θ' ,

$$\theta(x, y, z) = \bar{\theta}(z) + \theta'(x, y, z).$$

θ_0 is a representative potential temperature for the location at which the static stability parameter is being calculated and z is the height. $N^2 < 0$ describes a statically unstable atmosphere, $N^2 > 0$ a statically stable atmosphere and $N^2 = 0$ describes neutral stability. Potential energy arising from an unbalanced mass distribution in the environment is converted into kinetic energy in the perturbation from the basic state allowing that perturbation to grow.

1.5.5 Moist static stability

Air containing water vapour is different from dry air in two respects. Firstly, latent heat release associated with the condensation of water vapour changes the lapse rate of a rising parcel. Secondly, the density of water vapour is less than that of dry air meaning that the density of air is a function of both its temperature and its mixing ratio. The virtual potential temperature, θ_v , describes the potential temperature that dry air would have if its pressure and density were equal to that of a given sample of moist air. Therefore, the buoyancy of a moist parcel of air is determined by the difference between its virtual potential temperature and that of its surroundings.

In the presence of moisture, an unsaturated parcel of air will, upon lifting, eventually reach a height where saturation occurs (known as the *lifting condensation level, LCL*). A saturated parcel of air releases latent heat associated with condensation of water vapour. This results in the lapse rate (the decrease in temperature with height) for saturated air being *less* than that for dry air. This means that a given environment may be stable for an unsaturated parcel of air, but unstable for a saturated parcel. This *conditional instability* (i.e. unstable on the condition that the air is saturated) is the instability responsible for allowing large convective storms to grow from initially small rising plumes of air. When determining the environmental conditions in which this instability exists it helps to define a thermodynamic variable that is conserved during condensation. Thus,

the *equivalent potential temperature*, θ_e , can be defined as the potential temperature that a parcel of air would have if all of its moisture were condensed and the resultant latent heat used to warm the parcel (Holton, 2004, p.290). Similarly, θ_e^* can be defined as the hypothetical equivalent potential temperature that the air would have if water vapour were added until saturated. Conditional instability exists if the environmental lapse rate of θ_e^* is negative:

$$\frac{\partial \overline{\theta_e^*}}{\partial z} < 0.$$

A given parcel (either unsaturated or saturated) will be unstable if its θ_e is greater than the environmental θ_e^* .

1.5.6 Convective Available Potential Energy

A parcel will spontaneously convect if it is less dense than the environment at that level. The level at which a parcel when lifted becomes less dense than the environment is known as its *level of free convection* (LFC). If a lifted parcel reaches this height it will accelerate upwards until it reaches its *level of neutral buoyancy* (LNB) at which the parcel has the same density as its environment. Above the LNB, the parcel will experience a downward acceleration which will act to return the parcel to the LNB. The energy available for conversion from potential energy to kinetic energy is equal to the *positive area*, PA, on a thermodynamic diagram,

$$PA = \int_{z_{LFC}}^{z_{LNB}} b' dz = \frac{w_{max}^2}{2}$$

where w_{max} is the maximum vertical velocity reached by a non-entraining parcel.

However, an unstable environment cannot exist for long since convective overturning results in the creation of a convectively neutral atmosphere. At mid-latitudes in the Earth's atmosphere it is common for large scale motions to cause adiabatic descent and warming of air from mid-levels to create a temperature inversion near the surface. Therefore, it is often the case that a *negative area*

(NA) exists on a thermodynamic diagram where a parcel if lifted from its initial level (LI) remains more dense than its environment,

$$NA = - \int_{z_{LI}}^{z_{LFC}} b' dz.$$

In the presence of this *convective inhibition* (CIN), free convection of a parcel will only happen if work is done to lift the parcel to its LFC.

Following Emanuel (1994) p.171, the *Convective Available Potential Energy* (CAPE) can be defined as,

$$CAPE = PA - NA$$

$$CAPE = \int_{z_{LI}}^{z_{LNB}} b' dz.$$

It is worth noting that the values calculated will be different depending on if the moist adiabatic processes are considered to be reversible or irreversible.

1.5.7 Linear theory of moist convection

Linear theory can be used to predict the expected growth rate of small perturbations from the basic state. The momentum equations are linearised along with the continuity and thermodynamic equations. These are then used to solve the vorticity equation in the x-z plane (see Appendix B for full derivation) to give,

$$\frac{\partial^2}{\partial t^2} \left(\frac{\partial^2 \psi}{\partial z^2} + \frac{\partial^2 \psi}{\partial x^2} \right) = -N_m^2 \frac{\partial^2 \psi}{\partial x^2} \quad (1.3)$$

where N_m^2 is the moist static stability parameter in a saturated atmosphere and ψ is the streamfunction.

This has solutions of the form,

$$\psi = \psi_0 e^{i(kx+mz)+\sigma t},$$

where k is the horizontal wavenumber, m is the vertical wavenumber and σ is the growth rate. This can then be substituted into 1.3 to find the growth rate, σ , as a function of N_m^2 and $\beta = \frac{k}{m}$; the aspect ratio of the convective cells,

$$\sigma = \sqrt{-\frac{N_m^2 \beta^2}{1 + \beta^2}}.$$

This results shows that with a positive moist static stability, σ becomes imaginary describing a solution that oscillates with frequency N_m (the *Brunt-Väisälä* frequency), i.e. a gravity wave in a statically stable environment. However, in a moist statically unstable environment ($N_m^2 < 0$) σ is real and the perturbation grows exponentially with time i.e. a growing convective circulation. Moreover, $\sigma \rightarrow \Re(N_m)$ as $\beta \rightarrow \infty$ and $\sigma \rightarrow 0$ as $\beta \rightarrow 0$. i.e. tall, narrow cells grow faster than short, wide ones. Therefore, for a convective cell with a height scale imposed by a stable layer (e.g. the top of the boundary layer or the tropopause) cells with small horizontal scale will grow faster than those with a larger horizontal scale.

1.6 Representation of convection within high resolution numerical models

The best way of representing convection in numerical models depends strongly on the grid length of the model. With long grid lengths ($\sim 100\text{km}$) individual convective clouds cannot be resolved and so changes in the grid box mean variables associated with the net fluxes of heat, moisture and momentum resulting from a large ensemble of convective clouds are parameterised. This is possible due to the relatively high predictability of the second kind for convection. Conversely, in *large eddy simulation* where very short grid lengths ($\sim 100\text{m}$) are used, individual convective

clouds can be represented explicitly by the model's dynamics with only the isotropic turbulence being parameterised (Petch *et al.*, 2002).

However, between these two extremes a 'grey area' exists where the best method for representing convection is not so clear. The predictability of the second kind for convection reduces as the grid boxes become smaller and contain fewer convective clouds (Petch, 2004). Mesoscale models with 10km grid lengths cannot resolve most convection and so parameterisation schemes are used even though the theoretical conditions for their use are not necessarily met. Therefore a partitioning exists with some convection represented by the parameterisation scheme and the remainder represented explicitly (Done, 2003). As the grid length decreases to under 10km (as is the case in this thesis where a 4km grid length is used) the applicability of ensemble based parameterisation schemes is reduced still further. The best method of dealing with this problem remains an active area of research (e.g. Gerard and Geleyn (2005)). However, this problem is not the subject of this thesis and so no attempt is made to resolve it here. Instead, in the absence of a suitable alternative, the numerical model used in this study represents all convection explicitly with no parameterisation scheme employed. It is recognised that since 4km grid lengths are not capable of resolving all atmospheric convective eddies explicitly, this model will differ from the real atmosphere. Therefore, all results should be taken in the context of this model and care taken before applying them to the atmosphere. However, despite this recognition, work by Roberts (2003) has shown that when running the model used here with grid lengths of 4km, realistic convective storms can be reproduced.

1.7 On error growth in numerical weather forecasts

Quantifying the growth of errors in weather forecasts is at the core of research into atmospheric predictability. Understanding of the causes and nature of this error growth has come a long way in the past fifty years using a variety of different approaches. A review of some significant studies in this field is presented in this section, highlighting the different methodologies used and the error growth mechanisms involved. This review helps to provide the context for this new research.

1.7.1 Recognition of chaotic behaviour in the atmosphere

Although the work of Lorenz (1963) is popularly conceived to have been the first in the field of atmospheric predictability, many had recognised the problem that instabilities cause in weather forecasting, some time before.

Newtonian mechanics is based on the doctrine of determinism; however, as early as the first decade of the twentieth century it had become apparent that some deterministic systems exhibit extreme sensitivity to their initial conditions. Henri Poincaré investigated the stability of the solar system by studying the orbits of three bodies (the Sun and two planets) moving under mutual gravitational attraction. His work demonstrated that simple, non-linear systems could exhibit complicated behaviour over long periods, with the future state being highly sensitive to the initial conditions. In a later publication (Poincaré, 1914, p.68), it was noted that:

‘it may happen that small differences in the initial conditions produce very great ones in the final phenomena’.

In a further discussion it was suggested that the atmosphere also exhibited sensitive dependence on its initial conditions:

‘The meteorologists see very well that the equilibrium is unstable, that a cyclone will be formed somewhere, but exactly where they are not in a position to say; a tenth of a degree more or less at any given point, and the cyclone will burst here and not there, and extend its ravages over districts it would otherwise have spared. If they had been aware of this tenth of a degree, they could have known it beforehand, but the observations were neither sufficiently comprehensive nor sufficiently precise’.

Major advances in dynamical meteorology were made by (among others) Bjerknes, Rossby, Charney and Eady in the first half of the twentieth century. Analytical solutions of linearisations of approximated forms of the equations of motion (normal modes) showed that small perturbations could produce waves or exponential growth. The implications of the existence of this instability for the weather forecasting problem were noted by Eady (1951), p.464:

‘The practical significance of a demonstration that the motion is unstable is clear, for in practice, however good our network of observations may be, the initial state of motion is never given precisely and we never know what small perturbations may exist below a certain margin of error. Since the perturbation may grow at an exponential rate, the margin of error in the (final) state will grow exponentially as the period of the forecast is increased, and this possible error is unavoidable whatever our method of forecasting. After a limited time interval, which, as we shall see, can be roughly estimated, the possible error will become so large as to make the forecast valueless.’

1.7.2 The ‘dynamical’ approach to atmospheric predictability

It was around this time that the first experiments in numerical weather prediction (NWP) were taking place (Charney *et al.*, 1950). Interest inevitably turned to the accuracy of the forecasts produced by these models. These new nonlinear General Circulation Models (GCMs) allowed the issue of atmospheric predictability to be approached as an *initial value problem* in the form of ‘identical twin’ experiments. The divergence of two forecasts differing only in their initial conditions can be thought to be representative of the divergence of a forecast from the true state of the atmosphere.

This approach, later named the ‘dynamical’ approach (Lorenz, 1969b), was first used to quantify error growth in a GCM by Thompson (1957). Motivated by the possibility of improved forecasts brought about by an increase in observation density, two forecasts differing in their initial stream-function were made with a quasi-nondivergent model based on the quasi-geostrophic equations. Experiments were conducted in a single-level model where errors grew associated with barotropic instability and also in a two-level model where baroclinic instability was found to increase the error growth rate. Quasi-geostrophic models are incapable of representing convective instability and boundary layer turbulence. About seven days into the forecast the two atmospheric states were as different from each other as two states selected at random. Diminishing returns in forecast skill were found with increased observation density.

Several years after Thompsons work, Lorenz (1963) used the same approach in a two dimensional model of dry convective rolls consisting of three interdependent ordinary nonlinear differential equations. It was shown that forced, non-conservative hydrodynamical systems could exhibit

both periodic solutions (found analytically) and non-periodic solutions (found through numerical integration) even if the forcing remained constant. The main point of the paper was that the non-periodic flows were unstable to small perturbations. Steady state and periodic solutions did exist, but were unstable and so could never be approached by the other solutions causing the apparently chaotic behaviour. The discovery that deterministic chaos could exist in simple systems governed by ordinary nonlinear differential equations was significant. It took some years before the implications of this research were recognised outside of the atmospheric sciences. However, now nonlinear dynamics is a major area of research and is applied to systems as diverse as the stock market and the human heart beat.

This work was followed up by Lorenz (1965) using a model based on a two level geostrophic model containing only 28 variables. The initial growth rate of small errors was highly variable and depended on the circulation at that time. It was shown that the perturbations with the most rapid growth, in a linear sense, over a finite time were the eigenvectors of the product of the tangent linear model with its adjoint. These singular vectors have since been used to great advantage in operation ensemble weather prediction (Molteni *et al.*, 1996). This model, although simple, gave surprisingly similar results to GCMs with a range of predictability of less than one month.

As part of the Global Atmospheric Research Program (GARP) several more studies (Smagorinsky, 1963; Mintz, 1964; Leith, 1965) were commissioned to measure the growth of perturbations within the latest GCMs using the dynamical approach. These models were more sophisticated than that used by Thompson (1957) in that between them they included parameterisations of radiation, convection and the diffusion of heat and momentum by turbulent eddies. Although the models were multi-level, the coarse horizontal grid lengths used (up to 1000km in the case of Mintz (1964)) still made it debatable whether they could adequately resolve the unstable baroclinic modes. The growth of small amplitude sinusoidal temperature perturbations was investigated in each case. The somewhat varied results were summarised concisely by Charney *et al.* (1966). Leith (1965) found that the perturbations failed to grow significantly, which was attributed to the excessive eddy viscosity parameter required to provide computational stability. However, in the other two models, after an initial period of adjustment, exponential growth occurred before error saturation. The doubling time for perturbations during the quasi-exponential growth phase was found to be about 5 days. The range of deterministic predictability in these models (after which perturbations were as large as the difference between two random flows) was calculated to be between 19 to 29 days.

Smagorinsky (1969) continued the work using a primitive equation model with nine vertical levels, higher resolution (with grid lengths of 275km) and representation of moist processes. In agreement with the earlier studies, the synoptic scales had a predictability range of around 3 weeks. However, at this time Lorenz (1969a) was already highlighting deficiencies of the dynamical method's ability to quantify atmospheric predictability.

1.7.3 Scale interactions and the intrinsic limit of predictability

The dynamical approach discussed in the previous section finds the predictability of the model in question. However, numerical models are far from perfect representations of the real atmosphere. Since the predictability of the *atmosphere* (i.e. not the model) is the subject of the research, the limitations of the dynamical approach must be recognised.

Lorenz (1969b) described two alternative approaches to understand atmospheric predictability. The *empirical* approach involves finding occasions where the atmospheric state is very similar (an analogue) and calculating the rate of the subsequent divergence of the true states. This method has the advantage that it involves direct observations of the real atmosphere, unfortunately the disadvantage is that no good analogues have yet been found. The final approach, called the *dynamical-empirical* approach involved calculating error growth in statistical turbulence models where all scales of motion were represented explicitly with the spectrum of scales determined by coefficients based on the real atmosphere.

In a landmark paper Lorenz (1969a) adopted the dynamical-empirical approach to show that the atmosphere may be considerably less predictable than GCM studies involving the dynamical method suggest. The previous results implied that while forecasts did lose skill rapidly with time, the range of predictability could be extended indefinitely by reducing the initial errors sufficiently. However, it was argued that this would not be the case in the atmosphere where coupling exists between structures at different spatial scales. Even if the scales resolved by the model grid could be represented without any errors, then errors associated with unresolved features would induce errors in the larger scales which would then grow as before. Since smaller scale eddies grow more rapidly, the upscale error cascade rate increases as the scale decreases. Therefore, if errors are confined to increasingly small scales the range of predictability will tend asymptotically towards an *intrinsic limit of predictability* beyond which the skillful forecasts can never be made no mat-

ter how small (if not zero) the initial error. This led to the conclusion that certain deterministic systems are observationally indistinguishable from indeterministic systems.

While the *effects* of sub-grid scale processes on the larger scales were represented in GCM parameterisation schemes, the *uncertainty* associated with those effects were not included. Therefore the unresolved scales in these models were always error-free. Consequently, Lorenz (1969b) argued that the ranges of predictability found in Smagorinsky (1963), Mintz (1964), Leith (1965) and Smagorinsky (1969) were overestimates of that of the real atmosphere. The model used by Lorenz (1969a) to demonstrate this, although barotropic and dry, was in certain important respects more representative of the real atmosphere than GCMs in that scales of motion between 40m and 40,000km were represented explicitly (compared to GCMs where features cannot be represented explicitly below the grid scale). The results confirmed that provided the spectrum of scales followed a k^{-3} power law or less (where k is the wavenumber) then the model had an intrinsic limit of predictability. Figure 1.6 shows the spectrum of a perturbation evolving upscale with time (thin lines) and the atmospheric spectrum used (thick line).

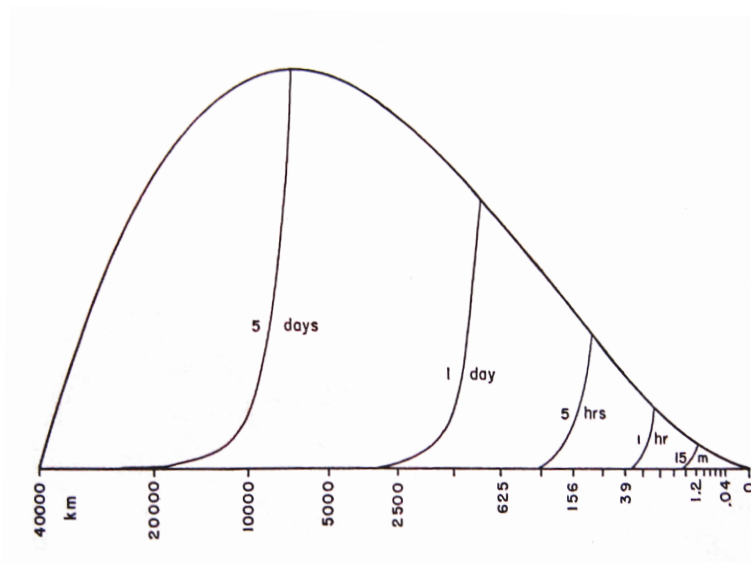


Figure 1.6: Basic energy spectrum (thick curve), and error-energy spectrum (thin curves) at 15 minutes, 1 hour, 5 hours, 1 day and 5 days for perturbations initially confined to the smallest resolvable scales. Vertical co-ordinate is energy per unit logarithm of wave length, divided by fourth root of wavelength. [Reproduced from Lorenz (1969a)].

Observations show that the atmospheric spectrum follows a $k^{-\frac{5}{3}}$ power law at scales below around 100m associated with the inertial subrange of isotropic three dimensional turbulence (e.g. Garratt (1992)). There is also evidence of a $k^{-\frac{5}{3}}$ power law in the mesoscale. However, synoptic scales tend to be dominated by a k^{-3} power law (Gage, 1979; Lilly, 1983). This leads to the question

of whether or not the range of predictability in the atmosphere can be extended indefinitely or instead has an intrinsic limit of predictability. Leith and Kraichnan (1972) addressed this issue using a turbulence model to examine error growth in both the $k^{-\frac{5}{3}}$ power and k^{-3} power inertial ranges. In both cases it was found that errors initially confined to high wavenumbers spread towards lower wavenumbers indicating the presence of an intrinsic limit of predictability. With initial errors made to approximate those that might be achieved using satellite observations, the saturation timescale at synoptic scales was found to be around 10-12 days.

1.7.4 Quantification of forecast errors using analysis cycles

A decade after the work of Leith and Kraichnan (1972), Lorenz (1982) used forecast and analysis data from the European Centre for Medium Range Weather Forecasts (ECMWF) to quantify the error growth in their operational forecasts. In this study, a different approach was adopted. Since the difference between a one day forecast and its verifying analysis is usually very small, it can be thought of as a perturbation. The growth of this perturbation after 24 hours can be found by looking at the difference between the two and one day forecasts. The further evolution can be found by calculating the difference between the three and two day forecasts etc. Similarly, the growth of slightly larger perturbations can be found by starting off with the difference between the analysis and the two day forecast. This was repeated for all operational forecasts out to 10 days over a 100 day period using the root mean square (RMS) difference in the 500hPa height field as a measure of difference (see Figure 1.7). This method implicitly includes error growth from all instability mechanisms (including those at the sub-grid scale) since the analysis reflects structures in the real atmosphere grown by all instabilities.

This provided a set of error growth curves for perturbations of different initial amplitude. An attempt was then made to fit curves to the data to allow the growth to be extrapolated to perturbations of very small amplitude giving an upper bound on the range of predictability. The curve used was a first order differential equation with a linear term to represent the growth and a negative quadratic term to create error saturation. The results showed that ‘better than guesswork’ forecasts were possible up to only two weeks in advance, i.e. less than the earlier dynamical method GCM studies. This work was carried further by Dalcher and Kalnay (1987) who parameterised the error growth as a function of wavenumber and later by Stroe and Royer (1993) who compared the previously used error growth curves.

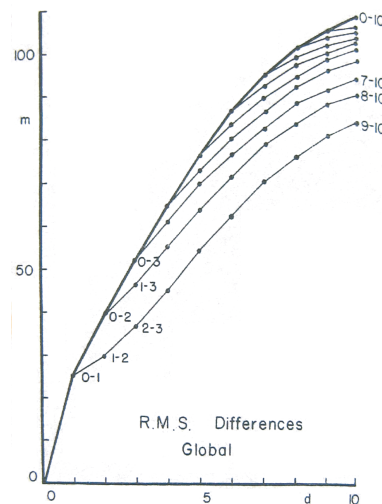


Figure 1.7: Global root-mean-square 500hPa height differences in metres between j -day and k -day forecasts made by ECMWF operational model for the same day, for $j < k$, plotted against k . Values of (j,k) are shown beside some of the points. Heavy curve connects differences of forecasts on day k from their verifying analyses. Thin curves connect differences for constant $k-j$. [Reproduced from Lorenz (1982)].

1.7.5 Non-modal growth

The growth of normal modes (e.g. Eady (1951)) is exponential. However, most perturbations (unless specifically designed otherwise) do not project solely onto a single normal mode, but also have other components. The dynamical method was used by Lacarra and Talagrand (1988) to show that in a barotropic model the growth rate of small perturbations in the early stages of a forecast could *exceed* the subsequent quasi-exponential growth rate. Figure 1.8 shows schematically how over a finite time a random perturbation (described by its components along two non-orthogonal decaying eigenvectors) can have a growth rate exceeding the growth rate of the eigenvectors. In this case, even though both eigenvectors are *decaying*, over a finite time the perturbation has *grown*, i.e. the perturbation growth rate exceeds that of the normal modes. Therefore, the perturbations that have maximal growth in a finite time are not the normal modes of the system. However, if evolving linearly, with increasing time the eigenvector component with the largest eigenvalue will increasingly dominate and the growth tends towards exponential.

The faster initial growth rates present during non-modal or ‘transient’ growth was confirmed in further work by Farrell (1989) who showed that perturbations in baroclinic flow could also grow significantly faster than their exponential rates. Research into techniques of finding perturbations

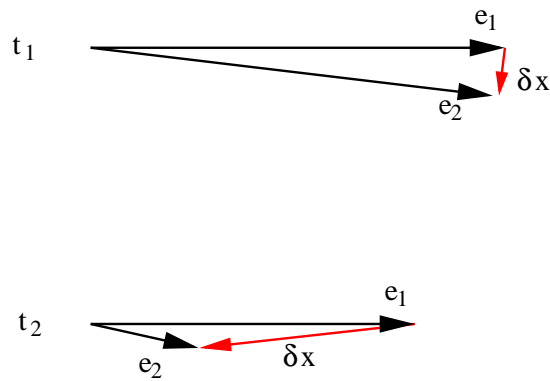


Figure 1.8: A schematic to illustrate the growth of a perturbation, δx , resulting from two eigenvectors with eigenvalues < 1 . ($t_2 > t_1$).

which are *optimal*, in the sense that their growth over a finite time is maximal (by some measure), has been motivated by the potential benefits for ensemble forecasting. The singular vector technique described by Lorenz (1965) finds those perturbations which have maximal growth in a tangent linear model. Alternatively, the ‘error breeding’ technique (Toth and Kalnay, 1993, 1997) uses the increasing dominance of the leading eigenvector with time to evolve a random perturbation towards the fast-growing direction of phase space. The proponents of this method argue that it has an advantage over singular vectors in that it uses the full non-linear model rather than a tangent linear approximation. However, there is still much controversy as to the appropriateness of this method for finding fast growing perturbations (Errico and Langland, 1999a; Toth *et al.*, 1999; Errico and Langland, 1999b; Kalnay *et al.*, 2002).

While the existence of early sub-exponential growth (i.e. decreasing growth rate with time) has been shown to exist, other work has indicated the presence of super-exponential growth, i.e. early growth rate *less* than the subsequent growth. Schubert and Suarez (1989) quantified the average error growth in an ensemble of perturbations in a two level GCM. During the first week of the forecast, super-exponential error growth was observed at the large scales. It was suggested that the reason for this was that the errors inserted were unsaturated at the small scales, allowing an interaction with the large scales to take place. As the errors in the small scales grew, they seeded errors in the large scales increasing the growth rate. After small scale error saturation had occurred, the growth rate at the large scales remained constant.

Recently, Gilmour *et al.* (2001) examined the question of how long the linear approximation holds in a forecast motivated by the linear techniques used in optimal perturbation generation for ensemble forecasting. By comparing the symmetry in the evolution of two equal but oppositely signed

perturbations, the degree of linearity was assessed in the ECMWF and NCEP operational forecasting models. The results indicated that at synoptic scales the linear regime often lasted for less than a day and never more than two days. However, these hydrostatic models were not capable of representing convective instability explicitly and so gave no information about the linearity of the perturbation evolution in the early stages of the forecast associated with convection.

1.7.6 Error growth in mesoscale models: the importance of moist convection

While the majority of research into predictability has concentrated on error growth in medium range forecasts, the increased operational use of limited area mesoscale models by forecasting agencies has prompted new research into error growth in short range forecasts associated with smaller scale processes.

The importance of considering uncertainty in the lateral boundary conditions of a limited area model was highlighted in the first work in this field by Anthes *et al.* (1985). In this study, identical twin experiments were carried out in a limited area model (including parameterised convection, precipitation and boundary layer fluxes). Surprisingly, the perturbations did not grow appreciably in the first 72 hours of the forecast providing hope that mesoscale forecasts may have more success than anticipated. However, a subsequent paper by Errico and Baumhefner (1987) found several explanations for this lack of error growth. Firstly, the perturbations used by Anthes *et al.* (1985) partly projected onto gravity waves which by their nature did not grow. Secondly, the lateral boundary conditions used in the experiment were fixed (implying that the large scales contained no errors). This meant that forecast fields with no errors were continually being advected into the domain, while forecast errors developed by the mesoscale model were swept out of the domain. Finally, horizontal diffusion was found to dissipate forecast differences at small scales. Individual forecast fields contained energy at small scales but since these were forced by the large scales both perturbed and unperturbed forecasts developed almost identically.

Further work by Vukicevic and Errico (1990) showed that when the boundary conditions were also perturbed the error growth rate in the limited area domain were similar to those in a global model experiment. In addition, errors only grew at synoptic scales, suggesting that no new error growth mechanism was acting in this 20km grid length model. Ehrendorfer and Errico (1995) found similar results when calculating the singular vectors of a mesoscale model which did not

include moist processes. The fastest growing perturbations had baroclinic structures (as is the case in global models). Also, the growing perturbations represented only 0.25% of all possible degrees of freedom indicating that a random perturbation was unlikely to project onto a growing direction and would therefore decay.

The previous results failed to reveal any distinct error growth mechanism acting at the mesoscale. However, Ehrendorfer and Raeder (1999) showed that in the presence of moisture, errors could grow considerably faster at the mesoscale in the early stages of a forecast. In this study the singular vectors of a limited area model that included moist processes were calculated. The structure of these was different from the dry singular vectors. This indicated that a new error growth mechanism involving moisture was acting at the mesoscale. A similar result was found in Zhang *et al.* (2002) where the effect of removing data from a single radiosonde ascent from the analysis on the subsequent forecast of a large snowstorm was investigated. It was found that the small initial difference between this and the control forecast grew considerably at scales under 500km in a region confined to the Gulf of Mexico which after 24 hours changed the mesoscale structure of precipitation bands within the synoptic scale cyclone. Further simulations excluding latent heat release as well as the sonde observation showed less differences from the control forecast indicating that moist processes were responsible for most of the error growth in this case (see Figure 1.9).

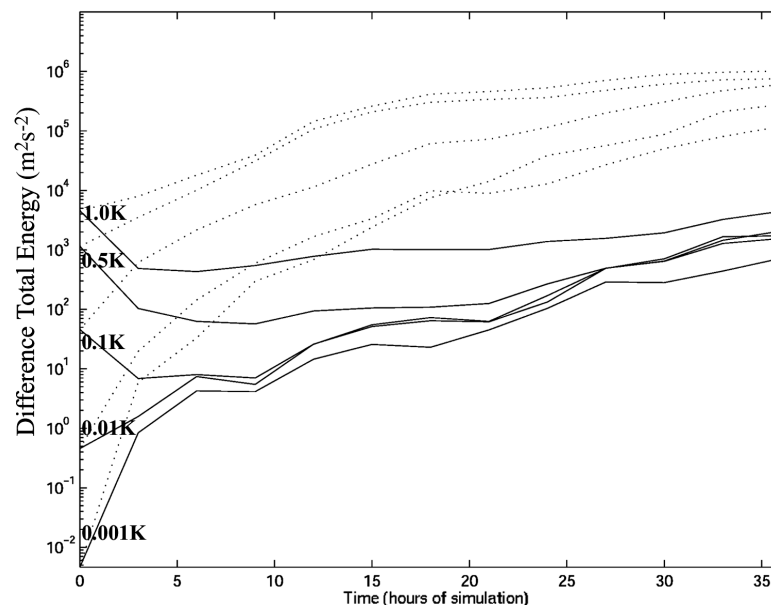


Figure 1.9: Error growth curves for perturbations with different initial amplitude. Results from the experiment using a model including latent heat release (dotted lines) and in the ‘dry’ experiment (solid lines). [Reproduced from Zhang *et al.* (2003)].

More recently, in a follow up paper (Zhang *et al.*, 2003) the researchers examined the issue in more detail using a mesoscale model run with horizontal grid lengths of 3.3km and 30km. It was hypothesised that moist convection was responsible for the rapid error growth in the previous paper. This was confirmed in the results. In the 30km model the most rapid error growth was associated with differences arising when model fields lay close to critical thresholds in the convective parameterisation scheme. In the 3.3km resolution model the errors were primarily in the timing and location of the explicitly represented convective storms. Perturbations with a smaller initial amplitude grew more rapidly, providing evidence of an intrinsic limit of predictability in the atmosphere. Also, an upscale transfer of error energy was seen which led the authors to conclude that the accuracy of mesoscale forecasts was constrained by error growth at convective scales. In addition, it was suggested that linear assumptions will quickly fail at these scales due to the rapid growth of errors to significant amplitude. The results of Zhang *et al.* (2003) were confirmed and generalised in Tan *et al.* (2004) where error growth due to moist convection in an idealised baroclinic wave with a conditionally unstable environment was quantified.

Therefore, moist convection has been identified as an important error growth mechanism acting at the mesoscale. Surprisingly, few studies have had the predictability of moist convection as the subject of their study. Petch (2004) examined the sensitivity of domain mean properties to initial temperature conditions in a high resolution two dimensional large eddy model. However, this investigation was into the second kind of predictability of moist convection.

The work of Zhang *et al.* (2003) and Tan *et al.* (2004) encountered error growth associated with moist convection from the perspective of synoptic scale forecasting. The moist convection proved to be the source of errors at larger scales. However, in both cases the moist convection took place in regions of strong baroclinic instability meaning that both mechanisms contributed to the total error growth. This thesis examines error growth associated only with moist convection with no baroclinic or barotropic instabilities present. In addition, the features of interest in this thesis are the convective storms themselves rather than their influence on larger scale systems.

1.7.7 Summary of literature review

- The existence of chaotic behaviour in the atmosphere and its implication for weather prediction were recognised long before the first predictability studies in GCMs (Poincaré, 1914; Eady, 1951).
- The dynamical approach to predictability involving the measurement of the divergence of two forecasts from slightly different initial conditions was used in both simple models by Lorenz (1963, 1965) and GCMs by Smagorinsky (1963), Mintz (1964), Leith (1965) and Smagorinsky (1969) to understand the growth rates of errors associated with barotropic and baroclinic instabilities.
- However, the dynamical approach was found to have limited applicability to the atmosphere when used in GCMs due to problems representing errors associated with unresolved scales. Further work by Lorenz (1982) and Dalcher and Kalnay (1987) employed a different method where the divergence of forecasts from the verifying analysis was measured. These studies revealed faster error growth rates in accordance with the upscale transfer of error from the unresolved scales.
- Lacarra and Talagrand (1988) demonstrated that while the growth of normal modes is exponential, the growth rate of random perturbations during the early stages of a forecast may exceed the subsequent exponential growth.
- In mesoscale models, moist processes have been found to increase the error growth rate and reduce the dominant spatial scales of the errors (Zhang *et al.*, 2003). However, no studies have isolated moist convective processes from large scale instabilities to quantify the error growth arising from moist convection alone.

1.8 Thesis outline

The numerical model used in this thesis is described in Chapter 2 along with details of the nature of the convective cells and their initiation in the idealised case study. Chapter 3 outlines the ‘dynamical’ methodology adopted in these predictability experiments. This is followed by an analysis of the evolution of the perturbation structure in order to fulfill the first aim of understanding the mechanisms acting to grow the perturbations (see thesis aims in section 1.3). The results reveal two error growth mechanisms which dominate in the first three hours of the forecast. An attempt is then made in Chapter 4 to separate the relative contributions of these two mechanisms to the total error growth. The second aim of quantifying the error growth rates in the forecast as a function of spatial scale is addressed in Chapter 5 using a Fourier analysis of the growing perturbations. The final aim of quantifying the error saturation timescale is met in Chapter 6. Finally, the thesis conclusions and implications of the results are discussed in Chapter 7 along with an acknowledgement of the limitations of the work.

CHAPTER TWO

Description of an idealised simulation of convection in a cold air outbreak

The problem posed in Chapter 1 dictated that a high resolution numerical forecast model should be used to quantify error growth in an idealised representation of a cold air outbreak. A full description of the model used to fulfill the thesis aims, along with a description of the idealised case study and the initiation of moist convection within it are presented in this Chapter.

2.1 Description of the idealised Unified Model

The model used in this thesis is an idealised configuration of the United Kingdom Met Office's numerical forecast model, the *Unified Model* (version 5.3). This section provides a description of the model dynamics and physical parameterisation schemes used in this idealised configuration of the model which differs from the operational setup in several respects.

2.1.1 Prognostic variables

This section details the prognostic variables in the model, i.e. those that are *predicted* by the model. Three components of the wind, u, v and w represent the westerley, southerley and vertical

components respectively. The potential temperature, θ , of the air is also predicted along with the air density, ρ .

The air pressure in the model is defined in terms of an ‘Exner pressure’, Π ,

$$\Pi = \left(\frac{p}{p_0}\right)^\kappa$$

where p is the pressure, p_0 a reference pressure (1000hPa) and $\kappa = \frac{R_{dry}}{c_p}$, with R_{dry} the gas constant for dry air and c_p the specific heat at constant pressure for dry air.

Moisture in the atmosphere is represented as specific quantities (*kg per kg* of moist air) of either water vapour, q , cloud liquid water, q_{cl} or cloud ice, q_{cf} . The cloud scheme uses these prognostic variables to determine the *total water content*, q_t , which is composed of the *cloud water content*, q_c , and *specific humidity for water vapour*, q .

$$q_t = q + q_c.$$

where,

$$q_c = q_{cl} + q_{cf}.$$

The total water content is therefore conserved during changes in phase within clouds and during the formation and decay of clouds, i.e. it is a ‘cloud-conserved’ variable.

2.1.2 Model dynamics

The model is formulated around the non-hydrostatic equations of motion for a deep atmosphere. A full description of the dynamical core of the model is provided by Davies *et al.* (2005) and expanded upon by Staniforth *et al.* (2003). The use of governing equations with so few approximations allows a wide range of dynamical atmospheric phenomena to be represented. Barotropic and baroclinic waves and instabilities are well resolved and represented. Unlike in quasi-geostrophic

models, gravity waves remain unfiltered. The compressible nature of the model allows the existence of sound waves. The use of non-hydrostatic dynamics allows modelling of small spatial scales where the hydrostatic approximation does not hold in the atmosphere. Crucially, the small grid lengths possible in this model allow convective storms to be represented explicitly making growth by convective instability possible.

Following Davies *et al.* (2005), the governing equations written in spherical polar co-ordinates, (λ, ϕ, r) , (where λ is the longitude, ϕ is the latitude and r is the radius of the Earth) are,

$$\frac{Du}{Dt} - f_r v + f_\phi w - \frac{uv \tan \phi}{r} + \frac{uw}{r} + \frac{c_p \theta_v}{r \cos \phi} \frac{\partial \Pi}{\partial \lambda} = P^u$$

$$\frac{Dv}{Dt} + f_r u - f_\lambda w + \frac{u^2 \tan \phi}{r} + \frac{vw}{r} + \frac{c_p \theta_v}{r} \frac{\partial \Pi}{\partial \phi} = P^v$$

$$\frac{Dw}{Dt} - f_\phi u + f_\lambda v - \frac{u^2 + v^2}{r} + g + c_p \theta_v \frac{\partial \Pi}{\partial r} = P^w.$$

Semi-Lagrangian advection is used and so the material derivative remains in the UM.

The coriolis terms are $(f_\lambda, f_\phi, f_r) = (0, 2\Omega \cos \phi, 2\Omega \sin \phi)$, where Ω is the Earth's angular velocity. The P terms on the right hand side are tendencies in each component of the velocity resulting from parameterised processes.

The continuity equation for dry air is,

$$\frac{\partial \rho_{dry}}{\partial t} + \nabla \cdot (\rho_{dry} \mathbf{u}) = 0.$$

The equation,

$$\frac{DX}{Dt} = P^X$$

describes the change in a variable X , which can be either the potential temperature or a moisture variable, due to physical processes, where P are the tendency terms coming from the physics parameterisation schemes. For $X = \theta$ this becomes the internal energy equation. For example, latent heating by condensation is represented as a tendency in the temperature from the cloud parameterisation scheme when condensation is diagnosed.

Finally, the equation of state can be re-written in terms of the model variables as,

$$\kappa \Pi \theta_v \rho = \frac{p}{c_p}.$$

Semi-implicit time integration used in conjunction with semi-Lagrangian advection allows longer timesteps to improve efficiency while maintaining computational stability in the presence of sound waves (Davies *et al.*, 2005).

2.1.3 Model grid

A regular latitude-longitude grid in both the North-South and East-West directions is used in the horizontal. The variables are staggered on an Arakawa C-grid, with Π and ρ held at the same locations and u and v held at intermediate points.

In the vertical, a height based hybrid co-ordinate, η , is employed which is terrain following near the surface and constant height at upper levels (however, since this simulation is over the ocean, there is no orography and hence all η levels are constant in height). $\eta = 0$ at the surface and $\eta = 1$ at the upper boundary. The variables are staggered on a Charney-Phillips grid in the vertical with θ_v and w stored on the same levels (' θ levels') and u, v, ρ and Π held on intermediate levels (see Figure 2.1).

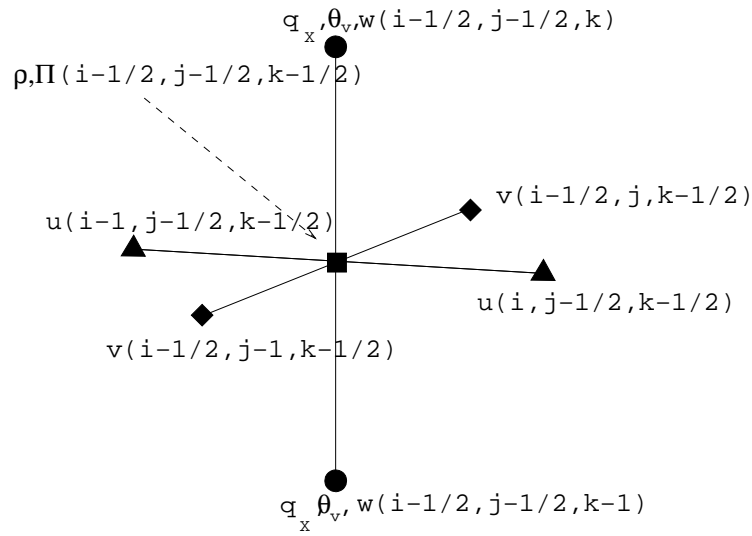


Figure 2.1: Schematic of the three dimensional staggering of the variables on the model grid used in the Unified Model. i, j and k are position indices for the grid. [Adapted from Staniforth *et al.* (2003)].

2.1.4 Cloud and precipitation schemes

Cloud and precipitation in the Unified Model are treated by separate parameterisation schemes. A full description of these schemes is provided by Smith (1990) and Wilson and Ballard (1999).

The cloud scheme calculates the cloud amount and cloud water content in each grid box by assuming a sub-grid scale variability of moisture about the grid box mean. This sub-grid scale variability of q_t is represented by a simple triangular distribution (Smith, 1990). Clouds form when the specific humidity at a location is greater than the saturation specific humidity, q_{sat} . Therefore, the amount of cloud in a grid box (and its associated cloud water content) is determined by the fraction of the distribution where $q_t > q_{sat}$ (see Figure 2.2). The ice cloud fraction is determined from the ice water content, q_{cf} . The *bulk cloud amount* describes the total cloud amount in a grid box, both liquid and frozen. The tendency of θ_v associated with the release of latent heat, P^{θ_v} , is then calculated by the cloud scheme.

The critical relative humidity, RH_{crit} , is the grid box mean relative humidity where the upper extreme of the moisture distribution is saturated. RH_{crit} can be specified for each model level. Increasing RH_{crit} has the effect of narrowing the distribution of q_t about the mean, i.e. for a narrower distribution with $max(q_t) = q_{sat}$, the mean of the distribution is higher.

The precipitation scheme determines the transfer of water between its different phases (Wilson

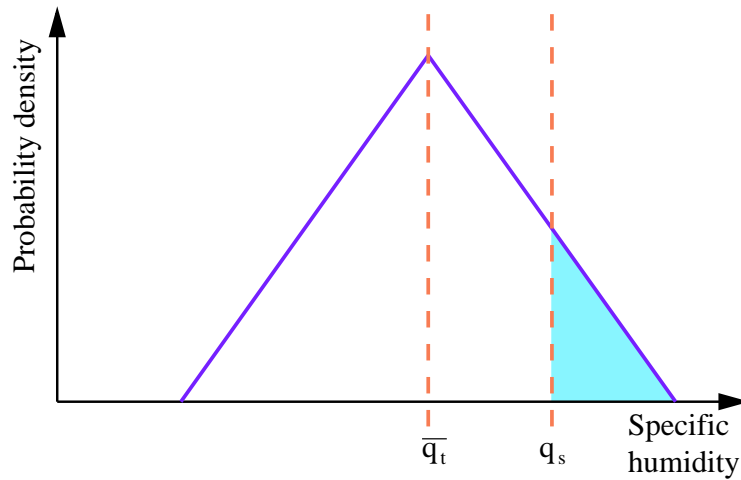


Figure 2.2: Schematic to illustrate the symmetric triangular distribution function used to represent the sub-grid variability of q_t about its grid box mean, \bar{q}_t . The cloud amount and cloud water content are determined by the fraction of the distribution that is supersaturated, i.e. $q_t > q_{sat}$. [Adapted from Smith (1990)].

and Ballard, 1999). The transfer of water between the different phases is based on microphysical processes. Figure 2.3 shows the mechanisms represented in this scheme. The precipitation scheme starts at the highest model level and calculates any transfer between water phases and associated change in temperature due to latent heating. Any precipitating ice or water is then released to the next level down and the calculations are repeated for that level. At the end of the process, the ice or rain which reaches the surface is removed from the atmosphere as precipitation.

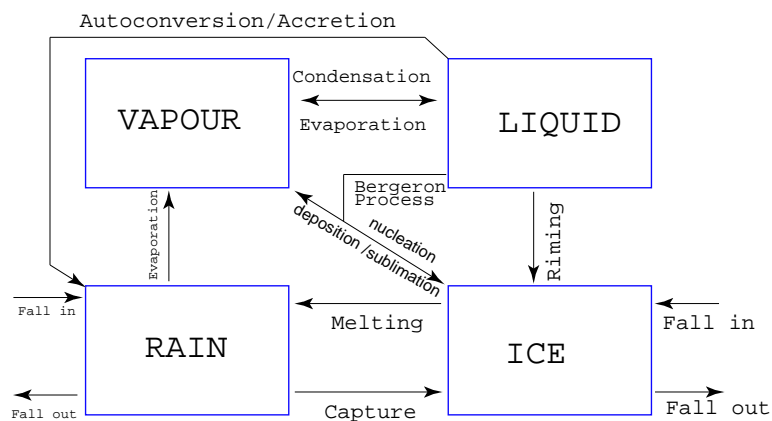


Figure 2.3: A schematic to illustrate the water phases held in the precipitation scheme and the modelled microphysical transfer processes between them. [Reproduced from Wilson and Ballard (1999)].

2.1.5 Boundary layer parameterisation scheme

The fluxes of heat, moisture and momentum due to sub-grid scale turbulent boundary layer eddies are parameterised. A full description of the scheme is given by Lock *et al.* (2000). Mixing is determined by the local Richardson number in stable layers, but is ‘non-local’ in unstable layers, i.e. the mixing at a given height is determined by the stability of the entire unstable layer and not just the stability at that specific height. This scheme uses the cloud-conserved variable, q_t , as well as another cloud-conserved variable, θ_l , the *liquid-frozen water potential temperature*; the potential temperature that the air would have if all the liquid and frozen water were evaporated. These variables are unaffected by phase changes and so mixing profiles can be specified continuously through any cloud and sub-cloud layers.

Firstly, the presence of any unstable surface driven layers is diagnosed by constructing a parcel based on θ_l and q_t at 10m with a temperature increase applied based on the surface buoyancy flux. This is then lifted until neutrally buoyant (if below the LCL) or until it has maximum buoyancy (if above the LCL) with that height taken to be the top of the surface based mixed layer. Then the type of boundary layer is diagnosed based on the mean gradients of the profiles of θ_l . Mixing profiles are then assigned depending on the boundary layer type.

The boundary layer type can be identified as either (i) stable, (ii) stratocumulus over a stable near-surface layer, (iii) well mixed, (iv) decoupled stratocumulus not over cumulus, (v) decoupled stratocumulus over cumulus or (vi) cumulus capped boundary layer. The mixing profiles associated with each boundary layer type are shown in Figure 2.4.

Cumulus is diagnosed if the gradient of q_t is greater than the mean gradient below the LCL multiplied by a threshold. In the presence of cumulus, the top of the surface mixed layer is set to the LCL so that the model dynamics is responsible for mixing in cumulus through explicit convection. It should be noted that this boundary layer scheme was designed for use with a mass flux convective parameterisation scheme, but in this study convection is being represented explicitly. The presence of unstable layers driven from the cloud top is identified in a similar way by moving a second parcel down from cloud top in areas where the cloud fraction is greater than a threshold value. If the surface-driven and cloud top-driven unstable layers do not meet then the cloud is diagnosed to be decoupled.

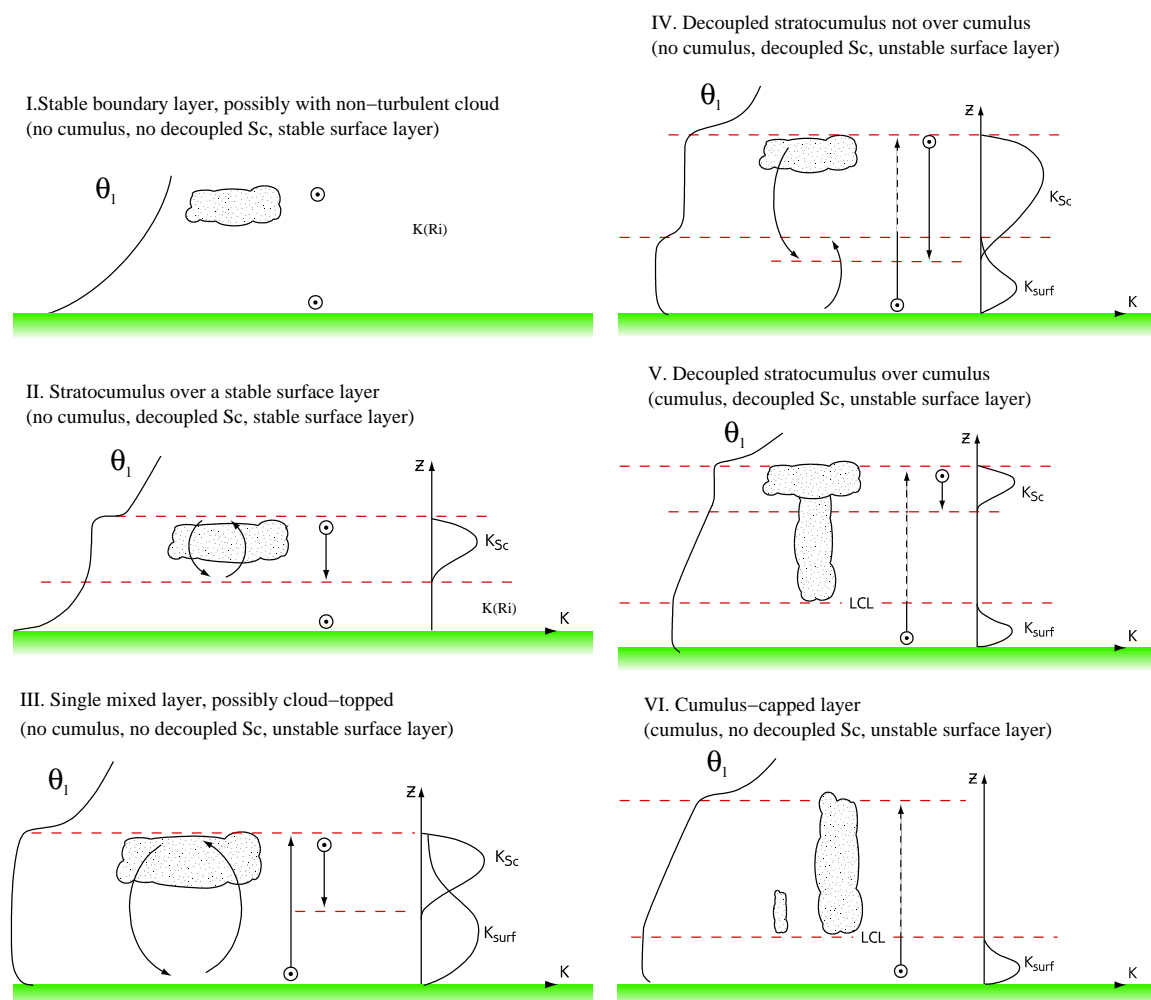


Figure 2.4: Schematic representation of the six boundary layer types represented by the parameterisation scheme. θ_l is the liquid water potential temperature. Profiles of eddy diffusivity, K , are shown for surface forced and stratocumulus forced mixed layers. The eddy diffusivity of stable layers is determined by the local Richardson number (Ri) (reproduced from Lock *et al.* (2000)).

2.1.6 Specifics of this idealised setup

The domain was chosen to be located entirely over the ocean at the equator. This removes the potentially complicating influences of land surface inhomogeneities and the Coriolis force from the system in order to keep this problem as simple as possible (as described in Chapter 1). The domain size was required to be large enough to accommodate a reasonable sample of convective clouds (~ 10 's of clouds) while still allowing the smallest grid length possible given the computational cost of the experiments being performed. In the end a grid of 64×64 points was used in the horizontal with a grid length of 4km. It would be preferable to have a shorter horizontal grid length, but the number of experiments being performed and the use of ensembles of forecasts made this unfeasible given the computational expense. In the vertical, the operational configuration of 38 unevenly spaced η levels was used which provides increased resolution in the boundary layer.

A timestep of 30 seconds was found to be computationally stable given the grid length used. While the model was designed to be used without explicit numerical diffusion, in practice some is required to avoid numerical difficulties. In the setup of the model used here, horizontal diffusion of heat, momentum and moisture is applied. The horizontal diffusion coefficient of $2.8 \times 10^4 \text{ m}^{-2}\text{s}^{-1}$ was chosen to damp features at the grid scale over two timesteps.

Bi-periodic lateral boundary conditions are used together with a free-slip lower boundary. A sponge layer is used at the upper boundary to reduce reflections.

As mentioned in Chapter 1, the model is run here without the use of a convective parameterisation scheme. Therefore, all deep convection in this model is represented explicitly by the model dynamics, cloud and precipitation schemes. However, it must be remembered that small boundary layer convective eddies are parameterised in the boundary layer scheme.

In this idealised setup, the radiation parameterisation schemes are replaced by an imposed tropospheric cooling profile and a fixed temperature at the lowest model vertical level. A cooling rate of 8K/day is imposed between the surface and 400hPa with a linear decrease to zero cooling at 200hPa. This cooling rate, although far higher than that caused by radiation in clear air, was chosen as a proxy for thermal advection during a cold air outbreak where cooling of this magnitude can occur. This cooling, combined with a fixed temperature of 300K in the first model level leads to convective destabilisation with time as the vertical temperature gradient increases. The choice

of temperature at the first model level is arbitrary as it is the *gradient* in temperature rather than the absolute values that influence the stability of the air.

2.1.7 Initialising the model

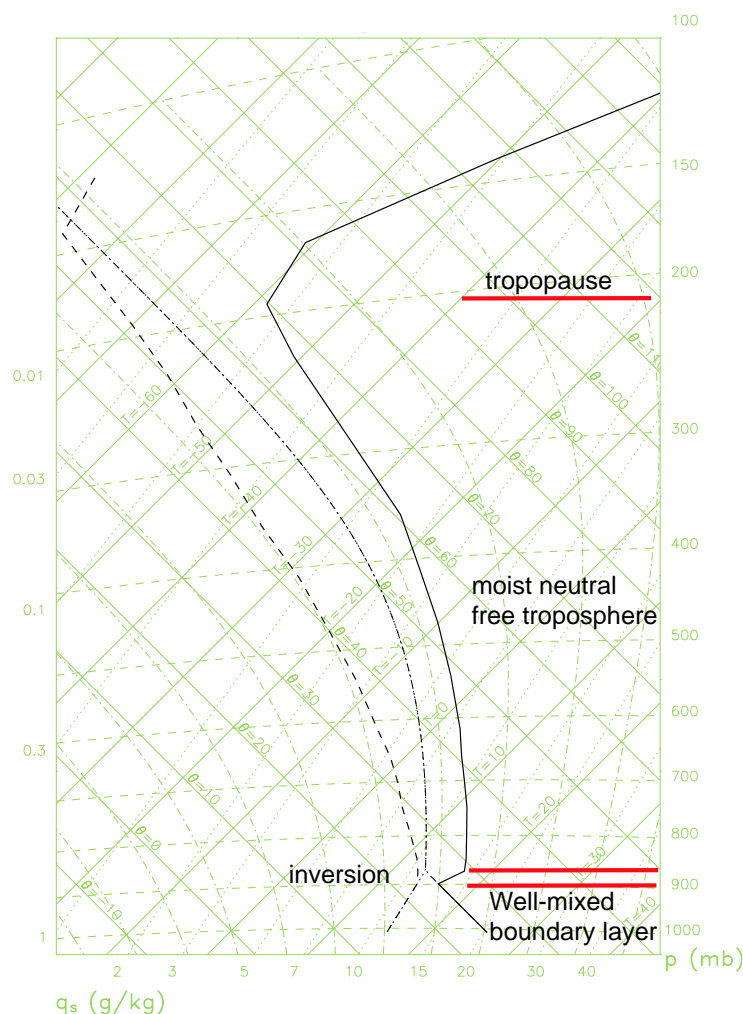


Figure 2.5: Tephigram to show the profile used to initiate the model at 00:00. Temperature is shown by the solid line, dew point is shown by the dashed line. The dot-dash line shows the profile created by the ascent of a non-entraining surface parcel.

This thesis investigates error growth during convective initiation. Therefore, the initial conditions of the simulation are designed such that deep convection will initiate several hours into the forecast. The profiles of temperature and moisture used to initialise the model are shown in Figure 2.5. A well mixed boundary layer (i.e. constant θ ; constant q) exists between the surface and 900hPa. This is capped by a temperature inversion between 900hPa and 850hPa. Above this the temperature profile follows a moist adiabat (i.e. constant θ_e^*) and the moisture asymptotes towards zero.

A tropopause is marked by a strong inversion above 200hPa. This profile is conditionally neutral, however there is a large Negative Area (see section 1.5.6) to be overcome. The cooling of the troposphere described in the previous section will result in conditional instability shortly after the model is initialised. The initial wind is specified as zero everywhere in the domain to ensure that all circulations that develop are associated with convection. These conditions of no wind-shear are conducive to the formation of single celled convective storms (Houze, 1993, p.285).

The initial conditions of the model specified by this profile are horizontally homogeneous; however, for convection to initiate, lateral density contrasts must exist to provide buoyancy. Therefore, in the lowest model level random white noise is inserted into the temperature field (the temperature and density of air being related by the equation of state) with an amplitude of 0.1K (as is common practice in the initialisation of large eddy simulations (e.g. Petch (2004))).

2.2 Description of convective initiation in this case study

The model was initialised at 00:00 (model time). Figure 2.6 shows a series of vertical cross-sections of vertical velocity and bulk cloud amount (i.e. both ice and liquid cloud) to illustrate the initiation of deep convection within the model. It can be seen that shallow circulations are present in the boundary layer as early as 01:00 which develop in-situ until scattered deep moist convection initiates between 09:00 and 10:00. The cumulonimbus which form then reach the tropopause after 10:20 with the anvils from different cells merging together to form a cirrus shield after 11:00. In this section the details of the initiation process are presented. It is shown that the initial white noise added to provide buoyancy at 00:00 determines the locations of the boundary layer circulations and subsequent deep convection over nine hours later.

2.2.1 Detailed description of convective initiation

Further detail on the exact sequence of events leading to the initiation of deep convection is provided by the tephigrams in Figure 2.7. The cooling of the troposphere which acts to erode the capping inversion at the top of the boundary layer is clearly evident. Also, the increase in dew point of the boundary layer air caused by the evaporation of moisture from the sea surface (evi-

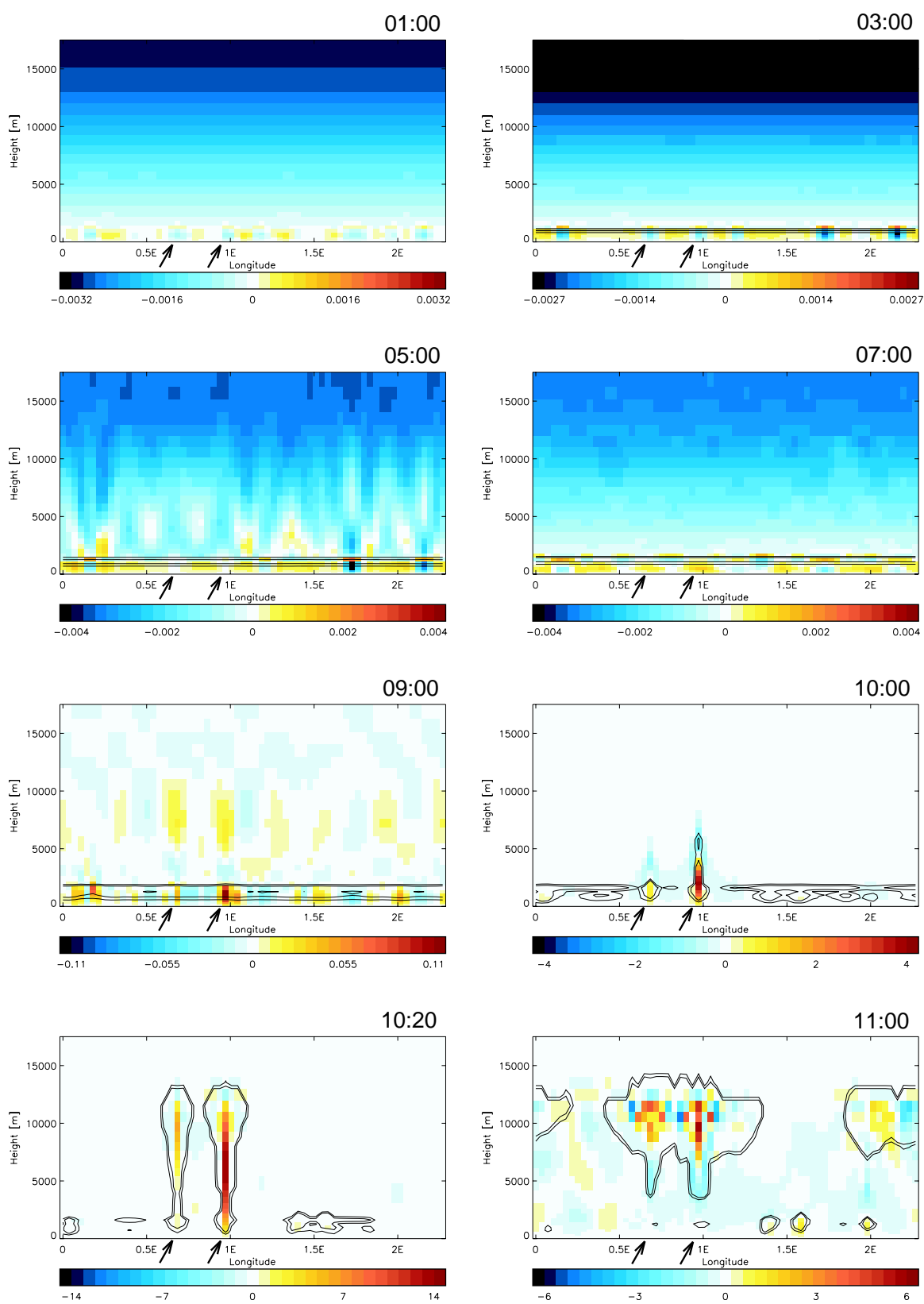


Figure 2.6: Cross-sections of vertical velocity (shaded) [$m s^{-1}$] and bulk cloud fraction (i.e. ice and liquid cloud), contoured at 0.2 and 0.4, at latitude 1.16N. The locations of the initiation of deep convection cells are marked by arrows.

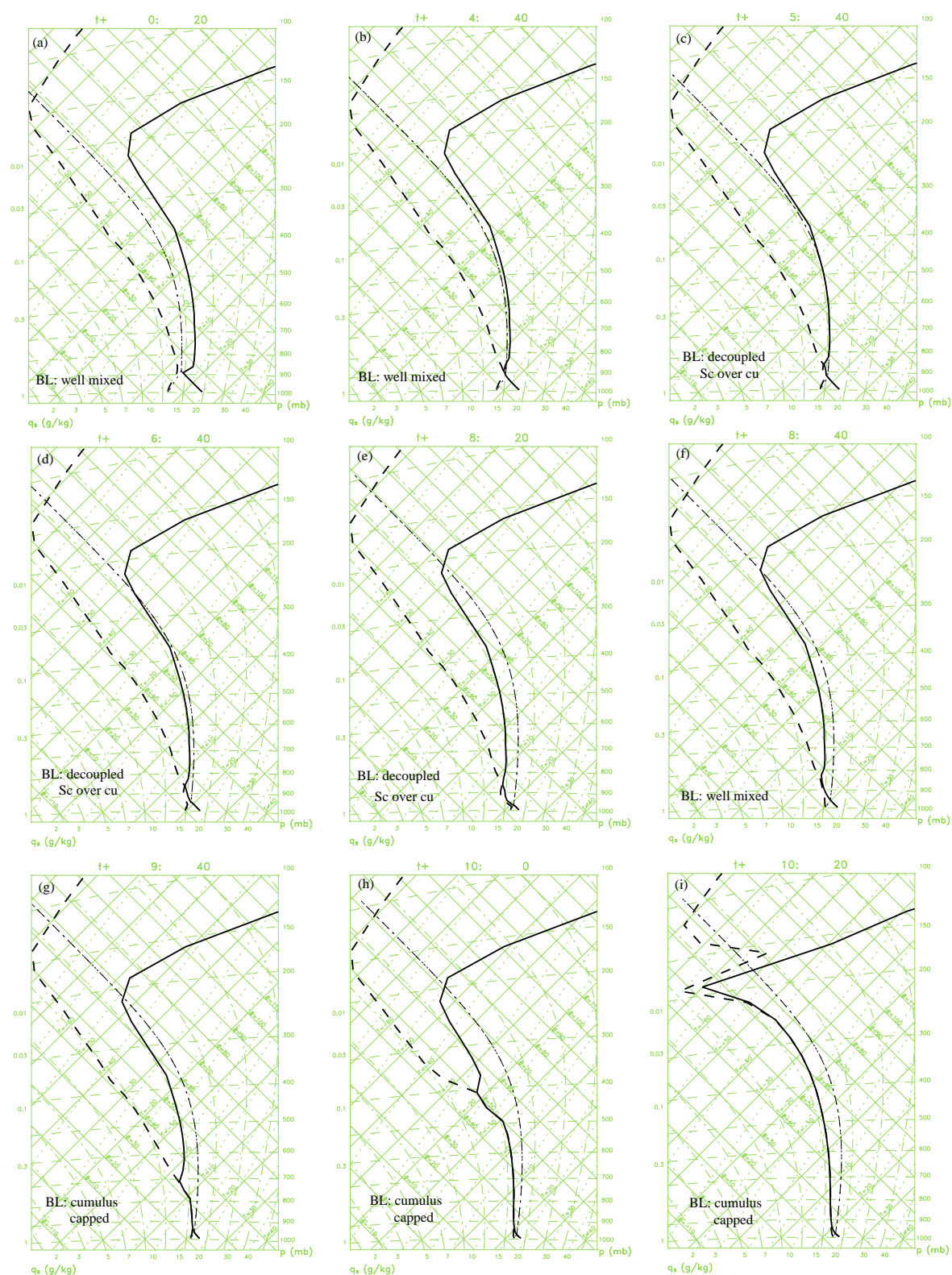


Figure 2.7: A sequence of tephigrams taken through the first storm to initiate (right arrow in Figure 2.6), (a)00:20, (b)04:40, (c)05:40, (d)06:40, (e)08:20, (f)08:40, (g)09:40, (h)10:00, (i)10:20. The temperature (solid line) and dew point (dashed line) of the environment is shown along with that of a hypothetical parcel lifted from the surface (dot-dash line). The model diagnosis of the boundary layer type at each time is also indicated.

dent by the high near-surface latent heat flux in Figure 2.8) can be seen to be responsible for the formation of the layer of cloud at the top of the boundary layer.

In this model, the surface fluxes are determined by the surface exchange coefficient which is governed by a velocity scale. This velocity scale is given by $\sqrt[3]{u^{*3} + w^{*3}}$, where u^* is the velocity scale of the shear-driven turbulence and w^* is the velocity scale of static instability-driven turbulence. In an unstable boundary layer it is therefore possible to have a non-zero surface exchange coefficient even in a no-wind setup such as this.

In an equilibrium situation these surface fluxes will balance the imposed cooling. Assuming a 10km well mixed layer, a heat flux of around 450Wm^{-2} is required to balance the 8K/day cooling used in this case. However, it can be seen that in this experiment an equilibrium has not yet been reached since the combined sensible and latent heat flux of 350Wm^{-2} is not enough to balance the cooling, resulting in a further destabilisation of the troposphere.

The moist layer deepens with time as the dew point continues to increase (e.g. from 03:00 to 09:00 in Figure 2.6). Some forced dry ascent can be seen above the rising plume (indicated by the dry adiabatic lapse rate between 720hPa and 780hPa at 09:40 and between 450hPa and 490hPa at 10:00). It is also worth noting that evidence of gravity waves propagating above the boundary layer can be seen in the vertical velocity field after 05:00 (see Figure 2.6).

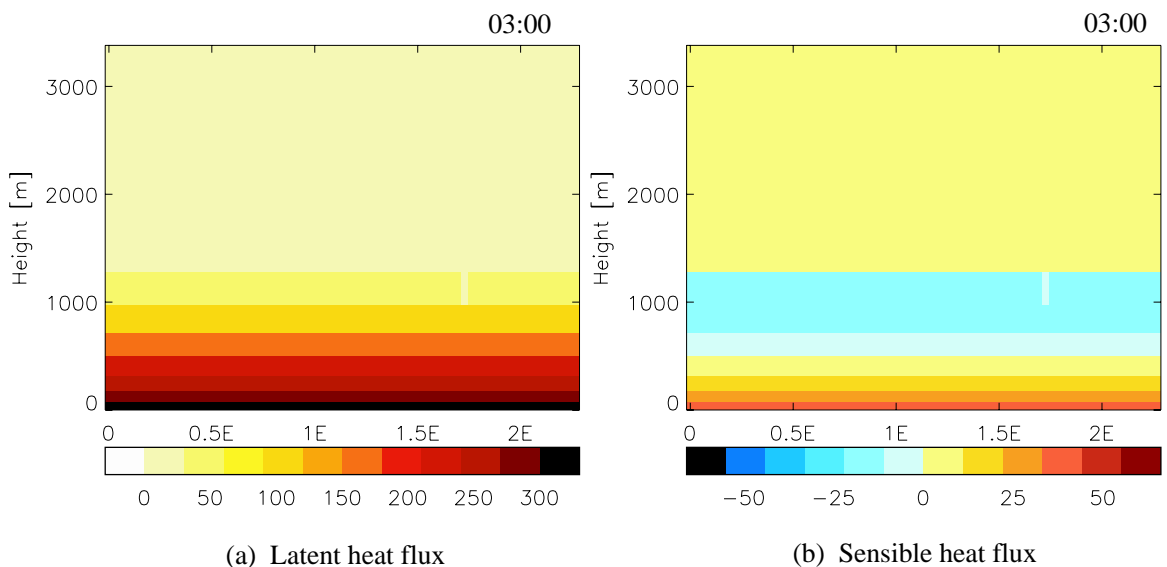


Figure 2.8: Cross sections (1.16N) of boundary layer (a) latent heat and (b) sensible heat flux [Wm^{-2}] at 03:00.

It is important to note that while a Positive Area (PA) appears on the tephigrams at around 05:00 (also shown in Figure 2.9) the convection does not rise above the boundary layer for another four hours. The circulations are so weak that the air, although accelerating due to convective instability, does not travel very far and so is not observed to rise. Figure 2.10 shows the maximum vertical velocity across the domain at a height of 180m. An approximately exponential intensification of the circulations occurs after the formation of a positive area at 06:00, but the maximum vertical velocity does not exceed 0.1ms^{-1} until around 09:00. Therefore, even though convection initiates sometime around 06:00, it is not until 09:40 that the vertical advection of air becomes strong enough to be observed.

In a numerical model with parameterised convection the response to instability is instantaneous. However, in this non-hydrostatic model with all moist convection represented explicitly, the circulations take longer to ‘spin-up’ due to the high effective viscosity of the model.

Once the convective storm tops have risen into the free-troposphere, they quickly accelerate towards the level of neutral buoyancy at the tropopause. Two storms are visible in the vertical cross-section shown in Figure 2.6, however many storms initiate across the domain (as evident in Figure 2.11). Figure 2.12 shows how the number of storms across the domain varies with time.

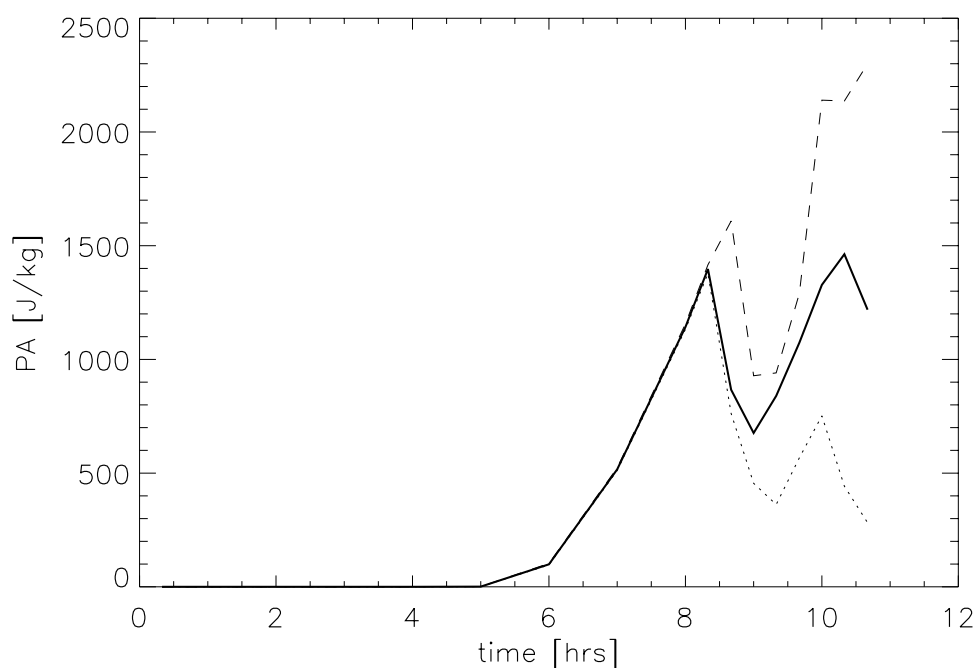


Figure 2.9: Plot to show the evolution of PA for a parcel at 1000hPa lifted to the tropopause. Domain mean PA -solid line, domain maximum PA-dashed line, domain minimum PA -dotted line.

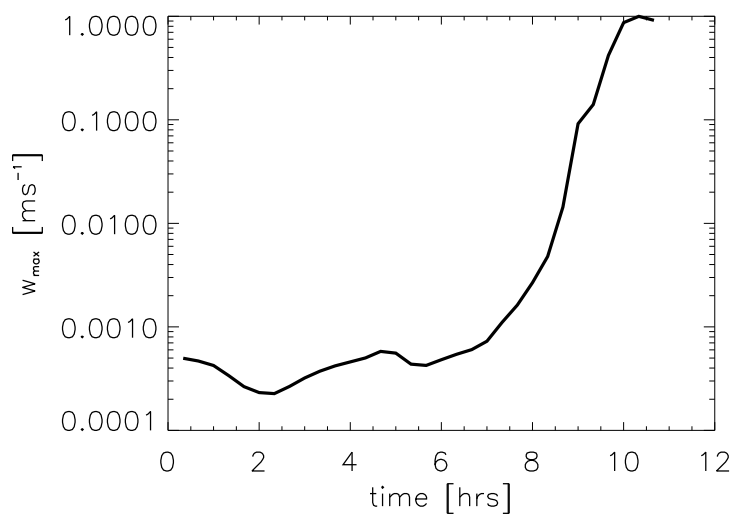


Figure 2.10: Maximum vertical velocity, w_{max} , in the boundary layer (on model level 3) against time.

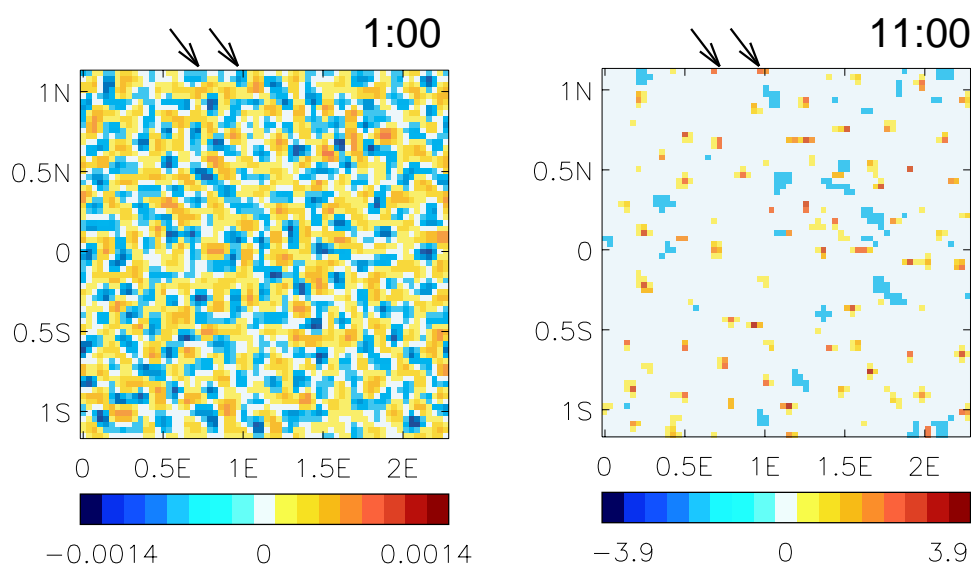


Figure 2.11: Plan views of vertical velocity, w , [ms^{-1}] at level 6 (720m). Arrows indicate the locations of the deep convective cells shown in Figure 2.6.

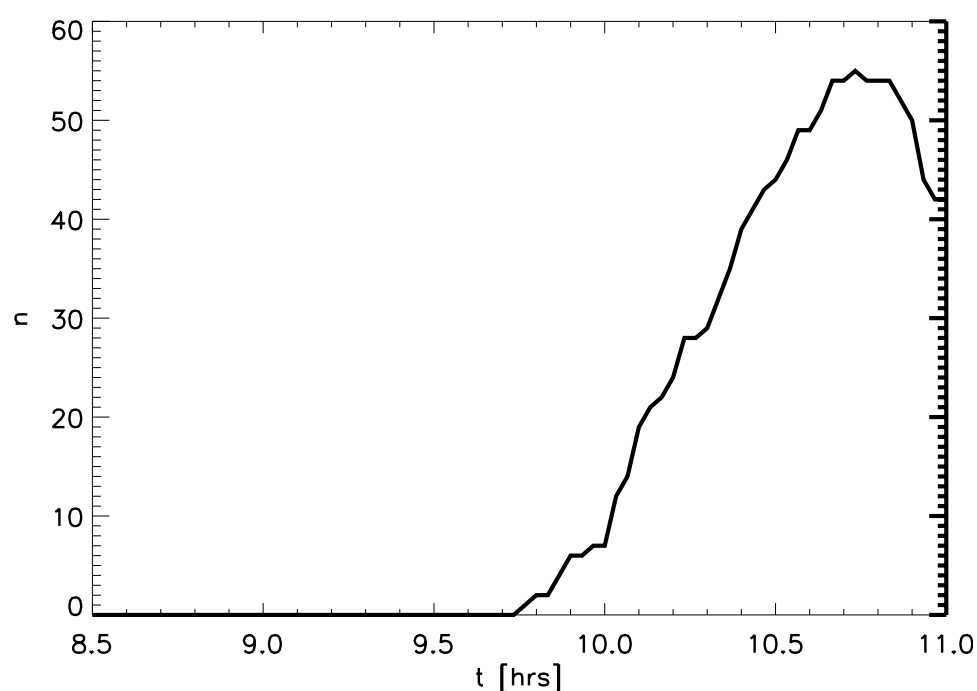


Figure 2.12: The number of storms as a function of time, as measured on level 7 (980m). A storm is defined as a region where w exceeds 3 m s^{-1} .

In this case a ‘storm’ was defined as any adjoining grid points where the vertical velocity, w , exceeded 3 m s^{-1} at 980m. After the initiation of the first storms at 09:30, the number of storms increases rapidly leading to a peak of 55 at 10:40.

2.2.2 Factors determining the location of the convective circulations

A correlation can be found between the random initial temperature inhomogeneities inserted at 00:00 and the vertical velocity in the convective circulations later on. Figure 2.13a shows the correlation coefficient between the vertical velocity and the temperature at different heights at 00:00. A strong negative correlation exists in the lowest two model levels, indicating that the temperature perturbations inserted to provide buoyancy are inducing vertical motion. Similarly, a correlation can be found between the vertical motion at the initial time and that at later times (see Figure 2.13b), i.e. the temperature inhomogeneities inserted at 00:00 induce vertical motions which are long lasting. Therefore, it can be seen that the shallow boundary layer circulations exist in the arrangement that they do because of the initial temperature inhomogeneities inserted. Indeed, this is not a surprising finding since these are the only inhomogeneities present in the initial conditions of the simulation. These circulations then develop as the destabilisation allows

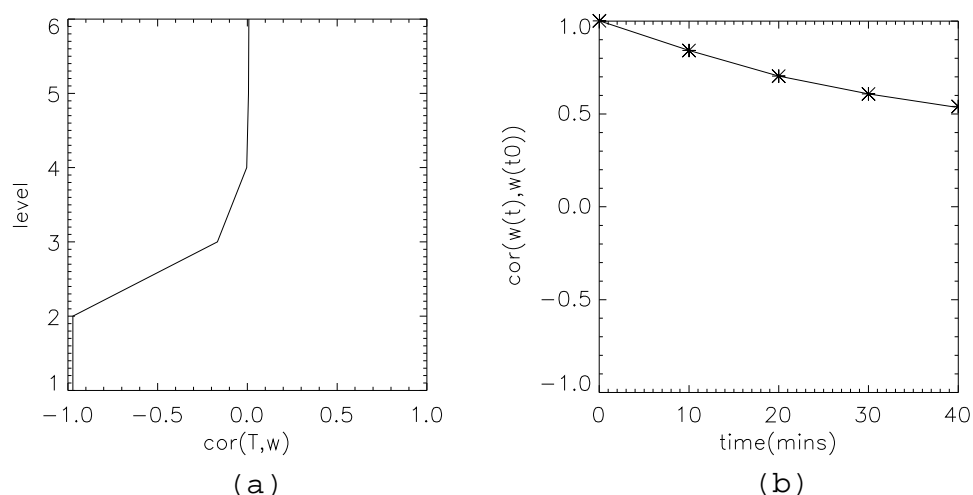


Figure 2.13: (a) The correlation between vertical velocity, w , and temperature, T , as a function of model level at initiation time 00:00. (b) The correlation between w at a given time (t) and the w field at the initial time t_0 at 500m height.

convective instability to increase their intensity.

The fact that these circulations persist for so long in the presence of explicit horizontal diffusion may at first seem surprising. These boundary layer circulations typically have a wavelength of approximately 25km and so should be damped over a timescale on the order of 30 minutes. However, it must be remembered that these circulations formed as a result of convective instability. This instability is acting to grow the circulations while diffusion is acting to dissipate them. The fact that these circulations persist indicates that the growth rate due to convective instability is greater than or equal to the dissipation rate by diffusion. It should be noted that as the horizontal scale of the circulations increases the effect of diffusion is decreased.

2.3 Description of the convective storms formed in this case study

If the results of this study are to have any relevance to the real atmosphere then it must first be established that the storms produced in the model have some similarities to those in the atmosphere. It has been shown that the shape of the clouds during their growth is similar to cumulonimbus clouds (see Figure 2.6 at 10:00, 10:20 and 11:00).

The horizontal scale of the clouds range from 8km to 12km diameter near their bases (these are not ‘grid point’ storms), widening slightly at the freezing level (4500m) since the saturation vapour pressure with respect to ice is less than that with respect to water, allowing air that was previously subsaturated with respect to water to become saturated upon freezing. Above around 8000m the cells widen further and spread out as an anvil at the tropopause at 12,000m. The anvils grow to wider than 50km and in some cases merge together to make a cirrus shield as is common in areas of deep convection in the atmosphere.

Overshooting tops are visible penetrating the tropopause where inertia carries parcels into the stratosphere before negative buoyancy returns them back down to the level of neutral buoyancy at the tropopause. These scales and features are comparable with typical single cell convective storms in the atmosphere.

To aid in the interpretation of different thermodynamic variables from the model data, a simple conceptual model of a single-cell convective storm is presented in Figure 2.14. In this Figure, a growing cumulonimbus cloud is outlined in black with contours of potential temperature (red) and specific humidity (blue) showing positive anomalies within the cloud associated with latent heating and the vertical advection of moist boundary layer air. The flow of the air through the convective circulation is illustrated by the black arrows. Areas of convergence exist near the

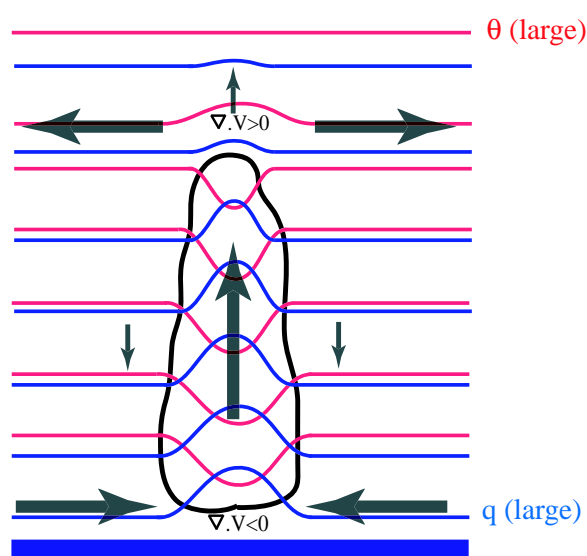


Figure 2.14: A conceptual model of a convective plume. Contours of potential temperature, θ (red) and specific humidity, q (blue) are shown. The outline of the cloud, or 100% relative humidity, is marked (thick black). Wind vectors are shown by the arrows along with areas of convergence and divergence.

cloud base and divergence at the cloud top.

Figure 2.15 shows a vertical cross-section which passes through two convective storms (the first at around 0.7E and the second around 1E). The locations of the storms are clearly marked by the updraughts visible in Figure 2.15a and the high relative humidity in Figure 2.15d. Furthermore, areas of convergence at cloud base and divergence at cloud top can be seen in the horizontal wind field in Figure 2.15b. The specific humidity is also seen to increase locally within the storms in agreement with the conceptual model (see Figure 2.15c).

The mean separation of the storms can be calculated using the number of storms in the domain. At 10:40, the peak of convective activity, there were 55 storms in the domain. This equates to a mean separation of 30km and a cell aspect ratio of 3:1 (horizontal:vertical); slightly closer spaced than those typically found in the atmosphere (Emanuel, 1994, p.206).

Maximum velocities inside the updraughts were typically in the region of 10ms^{-1} with a peak velocity of 31ms^{-1} . Although these values compare well with observations made in strong convective storms (e.g. Cunning *et al.* (1986)), they are slightly larger than might be expected from showers in a cold air outbreak. Also, it must also be remembered that the observed peak velocities mentioned above, only occur over small distances and are unlikely to be maintained over 4km, as is the grid length here. The large updraught velocities in this model are likely to result from the high inertia of the air within each relatively coarse grid box. Roberts (2003) found that in a 4km grid length model, convective circulations took longer to spin up, but became stronger than those in a 1km model. Higher resolution simulations would have a lower effective viscosity allowing convective circulations to spin up more readily and release instability earlier, before it had time to build up. As noted in the Chapter 1, the differences between this model and the real atmosphere must be remembered when drawing conclusions from the model data.

The maximum updraught velocities do not occur at the tropopause (see Figure 2.6) as would be expected for a non-entraining plume since the momentum of the updraught is diffused by the model with time. The updraughts are surrounded by weaker but more widespread subsidence which acts to dry and warm the surrounding atmosphere and create a new capping layer at the top of the boundary layer increasing the CIN. The pre-existing stratocumulus and cumulus clouds surrounding the cumulonimbus cells are evaporated in this subsidence (see Figure 2.6 between 09:00 and 10:20).

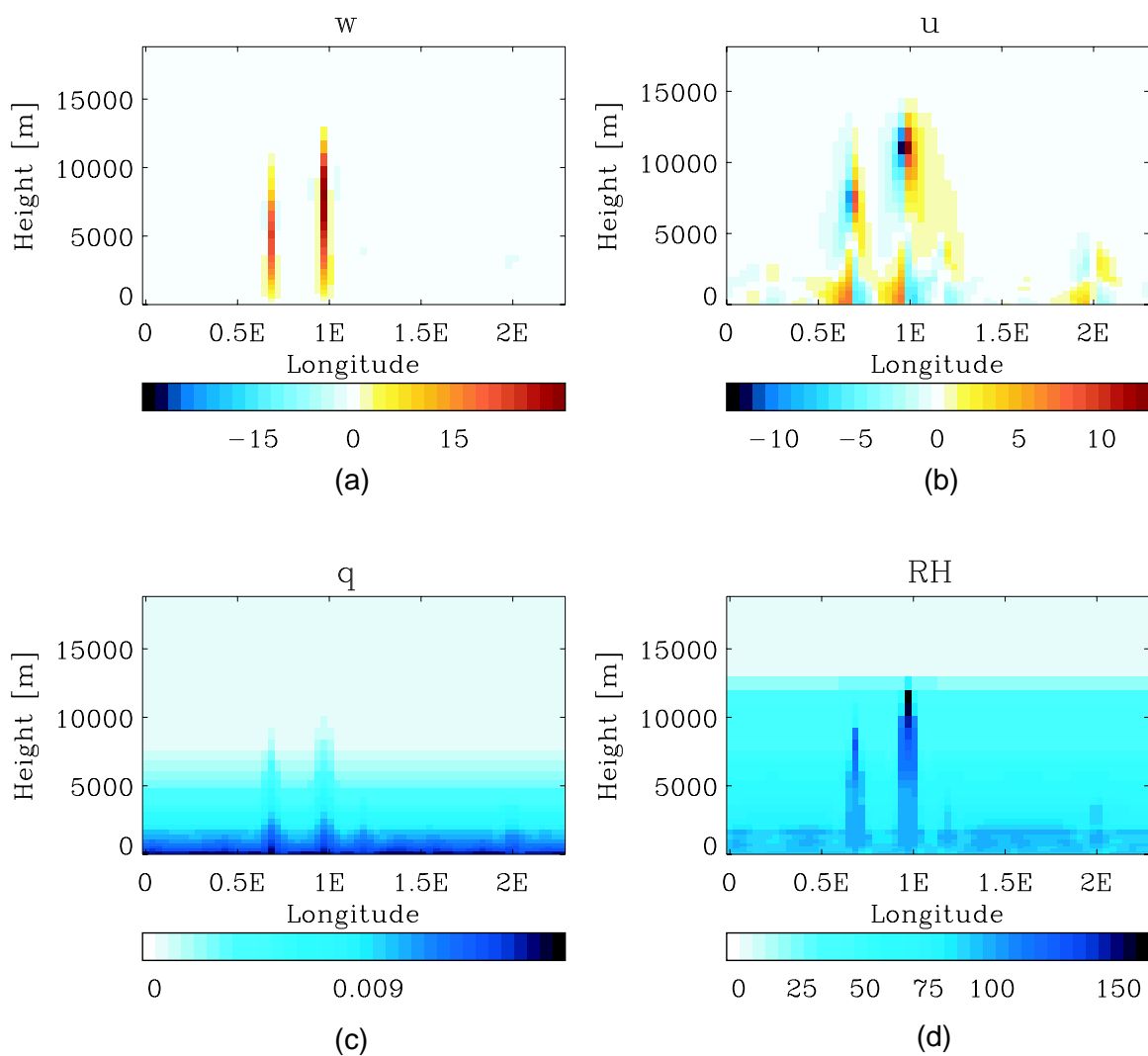


Figure 2.15: Cross-sections (1.16N) at 10:10 of (a) vertical velocity, w [ms^{-1}], (b) horizontal wind, u [ms^{-1}], (c) specific humidity, q [$kgkg^{-1}$] and (d) relative humidity, RH [%] to illustrate the structure of the convective plumes.

The lifetime of single cell thunderstorms should be of the order of the time taken for a parcel to pass through the system (Houze, 1993). With typical column mean updraught velocities of 5ms^{-1} a parcel traveling from the surface to the tropopause would take approximately 40 minutes. The first convection to penetrate the boundary layer does so at 09:30 and reaches the tropopause at 10:15. After this time the cell remains but begins to decay as the instability has been removed by the convective overturning. By 11:00 (90 minutes after formation) the remains of the cell are still present but all cloud below the freezing level (4500m) has evaporated leaving mainly cirriform remnants. This lifetime and lifecycle seem realistic for a convective system of this size.

The boundary layer circulations which led to the initiation of deep convection seem very long-lived for their small sizes. For example the vertical velocity signatures in the area of the first storm to form were present at the initiation of the model (00:00) and lasted until convective initiation at 09:30. However, vertical velocities present in the boundary layer prior to 09:00 are no higher than 0.003ms^{-1} ; at this speed it would take a parcel 93hrs to travel from the surface to the top of the boundary layer. Therefore, it can be seen that the lifetime of these features is in fact no longer than the time taken for a parcel to travel through them.

At the end of the simulation the original storms have decayed considerably with the cirrus shields remaining intact. Some new initiation is still taking place, however most of the convective available potential energy (CAPE) has been removed by the previous storms. It can be expected that if the simulation were extended, the CAPE would again build up due to the imposed destabilisation and cause new storms to initiate.

Although the initiation of all of the storms is not simultaneous (see Figure 2.12), there do not appear to be any cases of secondary initiation, i.e. the initiation of both the first storms to form and those later on, all appear to be due to the imposed destabilisation rather than by mechanisms related to pre-existing convective storms. No evidence can be found for convergence along out-flow boundaries and no storms are observed to propagate. Therefore, any error growth occurring in predictability experiments performed on this case study will be associated with the primary initiation of convection, as required by the thesis aims.

2.4 Chapter Summary

- The Met Office's Unified Model is formulated around the non-hydrostatic, fully compressible, deep atmosphere equations of motion. Fluxes of heat, moisture and momentum associated with unresolved boundary layer eddies are parameterised by a 'non-local' scheme which relies on first diagnosing a boundary layer type. Cloud and precipitation are parameterised by representing an assumed distribution of moisture values within each grid box; the fraction of this distribution which is saturated determines the cloud amount and the associated latent heating of the grid box.
- In this idealised setup of the model, no radiation or convective parameterisation schemes were used. Bi-periodic lateral boundary conditions were placed on the $64 \times 64 \times 38$ domain with a horizontal grid length of 4km.
- The profile used to initiate the simulation consisted of a well-mixed boundary layer capped by a strong inversion and a conditionally neutral free-troposphere. Convective destabilisation was imposed by a tropospheric cooling of 8K/day and a fixed sea surface temperature of 300K. Buoyancy required for convective initiation was provided by inserting random temperature inhomogeneities at the lowest model level.
- Shallow boundary layer convective circulations were generated directly by the buoyancy resulting from the temperature inhomogeneities at the bottom of the atmosphere.
- After the capping inversion had been eroded by the forced destabilisation 5 hours into the simulation the air in these circulations accelerated due to convective instability. Since the initial speed of the air in these circulation was only on the order of a few millimetres per second, it took a further 4 hours for the speed to increase to a point where the tops of the convective circulations rose significantly above the boundary layer.
- Scattered deep convective storms were triggered with the number of storms in the domain peaking at around 55, at 10:40.
- The size, lifetime and other characteristics of these storms are similar to those of single-cell convective storms in the atmosphere.

This case study provides a suitable platform upon which predictability experiments can be conducted. This high resolution mesoscale model represents all convection explicitly. The imposed

destabilisation is homogeneous across the domain and results in the primary initiation of scattered single-cell convective storms. Therefore, the results of predictability experiments performed on this case study will help to address the problem posed in section 1.2. The following Chapter will describe the predictability experiments performed.

CHAPTER THREE

Identification of the dominant perturbation growth mechanisms

The first stated aim of the thesis is to identify the dominant mechanisms acting to grow initial condition errors in the first three hours of the forecast (see section 1.3). It has been established that the idealised case study described in Chapter 2 provides a suitable framework within which experiments designed to address this aim can be performed. In this chapter, an experiment is described in which the divergence of the model states in forecasts differing only in their initial conditions is measured. The structure of these forecast differences is then used to identify the dominant perturbation growth mechanisms acting in the first three hours of the forecast.

3.1 Experiment methodology

The growth of forecast errors resulting from initial condition errors can be found by monitoring the divergence of the model states in two forecasts initiated from slightly different initial states, i.e. the ‘dynamical method’ described in Chapter 1. It must be recognised that this method is inadequate at modelling error growth associated with the representation of the unresolved scales as an implicit assumption is made that the sub-grid scales are error-free. Unfortunately, at the time of writing, convective scale analyses of the atmosphere are not available to allow a comparison of a forecast with reality. Nevertheless, the dynamical method can offer useful insights into the mechanisms acting to grow errors during a forecast and so is adopted here. In this thesis forecast error growth will be investigated by examining the growth of perturbations in the model. The word

perturbation will be used instead of *error* as perturbation growth between two forecasts will not exactly match error growth between a forecast and reality.

Several experiments are conducted in this thesis. To avoid ambiguity, each experiment is given a name so that the results can be compared between experiments clearly and without confusion. A table showing the different perturbation strategies used in each experiment in this thesis is presented in Appendix C. The experiment in this chapter will be known as experiment ‘MAIN’.

3.2 Perturbation strategy

Perturbations are inserted into the control run (described in Chapter 2) and the subsequent evolution of those perturbations is studied. Decisions need to be made regarding where in the domain the perturbations are inserted, to what variable they are made, the timing of insertion and the initial structure and amplitude of those perturbations. The exact methodology used to make these perturbations is described in this section.

A notation convention is adopted in this thesis whereby the vector, \mathbf{x} , describes the entire state of the model (i.e. the value of each prognostic at every grid point). Different model runs are labelled using subscripts and superscripts, e.g. \mathbf{x}_A^+ represents the state of the model in a forecast where perturbations have been *added* using the perturbation field designated ‘A’. Similarly, the values of individual variables can be specified (as opposed to the entire model state), e.g. θ_A^+ which represents the potential temperature field in the forecast described previously.

The unperturbed forecast described in Chapter 2 is known as the *control run*, $\mathbf{x}^c(t)$. Perturbations, \mathbf{x}^p , are then both added to and subtracted from \mathbf{x}^c at time t_0 to produce the initial conditions for two forecasts. i.e.,

$$\mathbf{x}^c(t_0) + \mathbf{x}^p = \mathbf{x}^+(t_0)$$

and,

$$\mathbf{x}^c(t_0) - \mathbf{x}^p = \mathbf{x}^-(t_0)$$

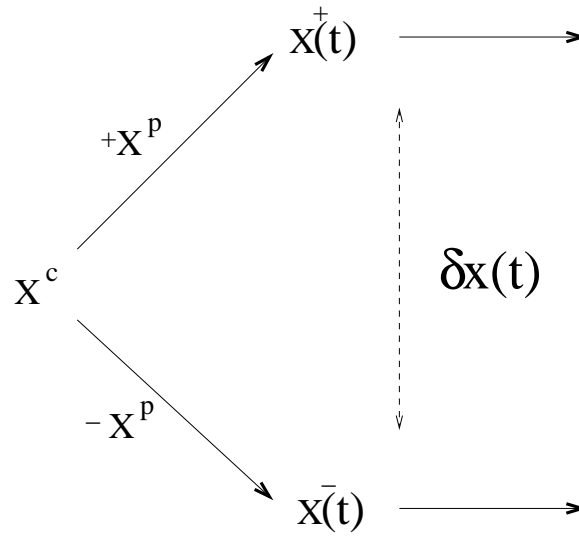


Figure 3.1: Schematic to illustrate the perturbation strategy employed in the experiments in this thesis.

where the forecasts, $\mathbf{x}^+(t)$ and $\mathbf{x}^-(t)$, resulting from those initial conditions evolve with time. The difference between these two forecasts,

$$\delta\mathbf{x}(t) = \mathbf{x}^+(t) - \mathbf{x}^-(t).$$

is then studied. i.e. it is the difference between two perturbed forecasts that is studied as opposed to the difference between a perturbed forecast and the control run (i.e. $\mathbf{x}^+ - \mathbf{x}^c$). Figure 3.1 illustrates this perturbation strategy schematically.

This methodology has certain advantages over measuring the difference between a perturbed run and the control run. For example, the *relative non-linearity* (defined later in section 5.5) uses the difference in evolution between two initially equal and opposite perturbations to measure the linearity of the perturbation growth. Also, this method is advantageous as it means that both forecasts involved ($\mathbf{x}^+(t)$ and $\mathbf{x}^-(t)$) have the same average properties in terms of spectral content, variance and energy.

3.2.1 Designing the perturbation field, \mathbf{x}^P

There are many ways that the initial conditions can be perturbed to produce differences in the forecast. Studies investigating error growth associated with synoptic scale motions often perturb

variables such as the 500hPa geopotential height (e.g. Smagorinsky (1969)). However, it seems likely that perturbations such as these would have a small impact to forecasts involving convection. In order for the perturbations to influence forecasts of moist convection, the perturbations should be made to variables that change the conditional stability of the environment. A parcel of moist air is unstable if its virtual equivalent potential temperature, θ_{ve} , is greater than the hypothetically saturated virtual equivalent potential temperature of its environment, θ_{ve}^* . Therefore, to influence forecasts of convection, θ_{ve} of the parcel or θ_{ve}^* of the environment must be perturbed.

In this model, θ and q are prognostic variables, however θ_{ve} and θ_{ve}^* are not. Therefore, θ_{ve} and θ_{ve}^* must be perturbed indirectly by perturbations to the prognostic model variables. While θ_{ve} is a function of both the potential temperature, θ , and the specific humidity, q , θ_{ve}^* is a function of θ only. Therefore, it was decided that the perturbations would be made to θ in the experiments in this thesis.

The growth of the perturbations is likely to be sensitive to the timing of their insertion. Horizontal diffusion in the model acts to dissipate any variability in the thermodynamic fields in the model with time. If the perturbations are inserted too soon before convective initiation then they may have dissipated completely before the time of interest. Similarly, if perturbations are added after initiation then the subject of this thesis (i.e. error growth during convective initiation) cannot be studied. Considering the long spin-up time of the convective circulations described in section 2.2.1 the exact time of convective initiation is hard to determine. However, the tops of the convective circulations rose above the boundary layer at around 09:30. Therefore, in this experiment perturbations are inserted one hour before this time, at 08:30.

Perturbations are made across the domain at a single height so that the sensitivity of forecasts to analysis errors at different altitudes can be investigated. A random perturbation field with some spatial coherency is constructed using a two dimensional convolution between a Gaussian kernel, $\mathbf{g}(i, j)$, and a random number field, $\mathbf{R}(i, j)$, where i and j represent the longitude and latitude respectively. i.e.,

$$\theta^p(i, j) = \mathbf{g}(i, j) * \mathbf{R}(i, j) = \sum_{j_0} \sum_{i_0} \mathbf{R}(i_0, j_0) \mathbf{g}(i - i_0, j - j_0)$$

where,

$$\mathbf{g}(i, j) = \frac{A}{s\sqrt{2\pi}} \exp^{-\frac{(i-i_0)^2 + (j-j_0)^2}{2s^2}}$$

where the parameter, s , determines the width of the Gaussian bump, A defines its amplitude and i_0 and j_0 define the location of its peak. Essentially, the convolution of the Gaussian kernel acts as a smoothing filter applied to the random number field.

The amplitude of the perturbations should be ‘small’ such that the linear regime of perturbation growth can be maintained for as long as possible. This will yield important information about the perturbation growth mechanisms acting. Therefore, perturbations are constructed in the method described above using θ^p with a maximum amplitude of only 0.001K which results in $\delta\theta$ perturbations of maximum amplitude 0.002K.

The spatial scale of the perturbations can be varied by changing the value of the parameter s . In the experiments in this thesis, s is set to one grid length for all perturbations.

3.2.2 Using a small (‘Lean’) ensemble to obtain more reliable results

In order to obtain more reliable results less prone to sampling uncertainty, an ensemble of three uncorrelated positive/negative pairs of perturbations is considered with each member constructed from different random perturbation fields, \mathbf{x}_A^p , \mathbf{x}_B^p and \mathbf{x}_C^p . Each of these makes a perturbed pair of runs (\mathbf{x}_A^+ and \mathbf{x}_A^- , \mathbf{x}_B^+ and \mathbf{x}_B^- , \mathbf{x}_C^+ and \mathbf{x}_C^-) and the evolution of the three resulting perturbation fields are studied,

$$\delta\mathbf{x}_A(t) = \mathbf{x}_A^+(t) - \mathbf{x}_A^-(t)$$

$$\delta\mathbf{x}_B(t) = \mathbf{x}_B^+(t) - \mathbf{x}_B^-(t)$$

$$\delta\mathbf{x}_C(t) = \mathbf{x}_C^+(t) - \mathbf{x}_C^-(t).$$

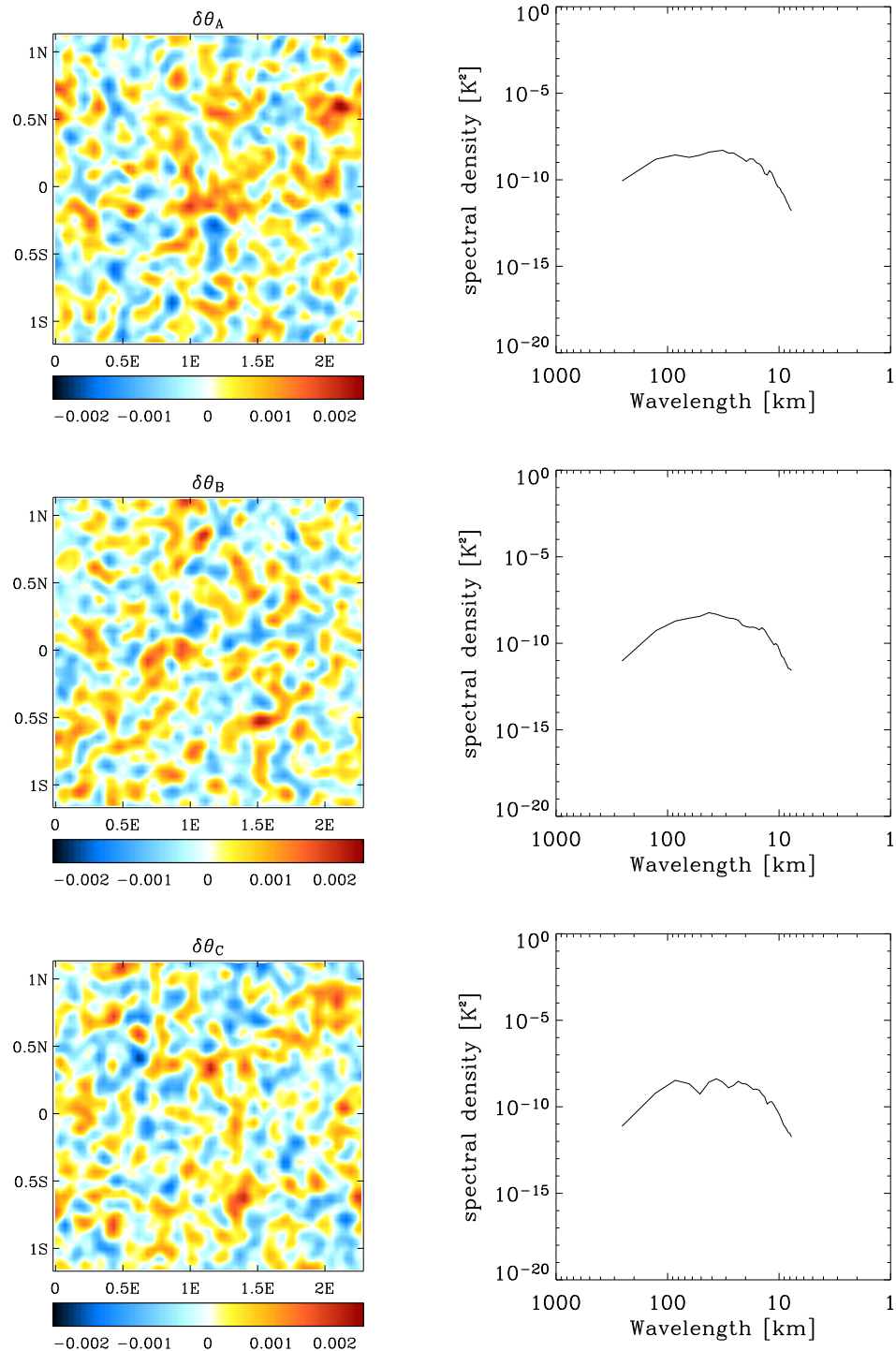


Figure 3.2: The three uncorrelated random perturbation fields, $\delta\theta_A$, $\delta\theta_B$ and $\delta\theta_C$ [K], used in each ensemble member (left) together with their corresponding power spectra (right).

An ensemble including more members would be desirable, but practical considerations including the computational expense of running the simulations and the large volume of data produced, constrain the number of ensemble members used in this study. Figure 3.2 shows the perturbations

at the time of insertion, t_0 . The power spectra of each perturbation is also shown. Table 3.1 and Figure 3.3 provide statistics of the perturbation fields constructed using a Gaussian kernel of amplitude 0.001K. It can be seen that the mean of these perturbations is close to zero (with any deviation from zero resulting from sampling error). The amplitude of the perturbations is also variable due to the random nature of the perturbations and the finite sample of points used. The correlation between the different perturbation fields (shown in table 3.2) is near zero as designed, making the perturbations nearly orthogonal.

	max [K]	min [K]	mean [K]	variance [K^2]
$\delta\theta_A$	0.002411	-0.002045	2.1964×10^{-5}	4.2798×10^{-7}
$\delta\theta_B$	0.002258	-0.001770	1.9699×10^{-5}	3.8287×10^{-7}
$\delta\theta_C$	0.002167	-0.002136	-1.4648×10^{-5}	4.1879×10^{-7}

Table 3.1: Statistics of initial perturbations, $\delta\theta_A$, $\delta\theta_B$ and $\delta\theta_C$.

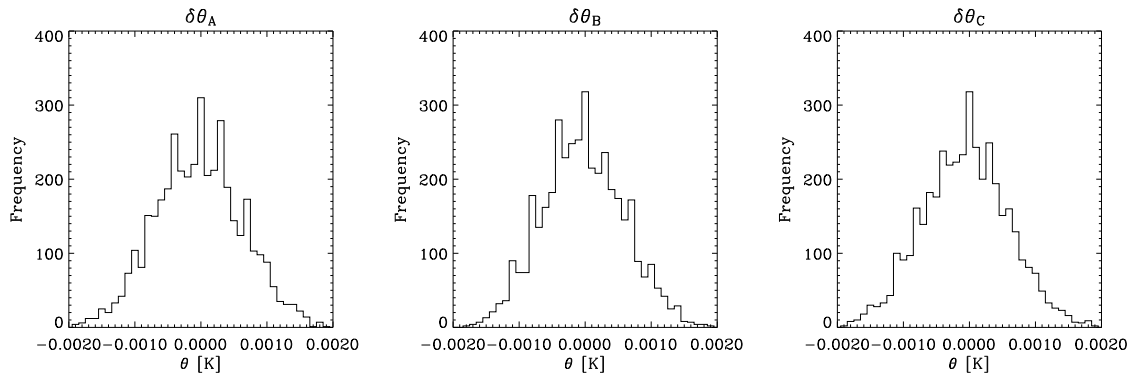


Figure 3.3: The distribution of values in the perturbation fields, $\delta\theta_A$, $\delta\theta_B$ and $\delta\theta_C$.

	$\delta\theta_A$	$\delta\theta_B$	$\delta\theta_C$
$\delta\theta_A$	1.0	-0.00665	-0.01989
$\delta\theta_B$	-	1.0	0.001264
$\delta\theta_C$	-	-	1.0

Table 3.2: The correlation between the perturbations, $\delta\theta$, for each ensemble member (A , B and C).

3.2.3 Determination of the appropriate height of perturbation insertion

The perturbation strategy defined above involves perturbing the potential temperature, θ , at a single height. It is hypothesised that perturbations to the boundary layer will have a greater impact on forecasts of convective storms than perturbations to the upper or mid-troposphere since convective

storms initiate in the boundary layer. Parcels of air rise from the boundary layer to the tropopause within convective storms, therefore perturbations to the potential temperature of the boundary layer will change the buoyancy of the parcels of air for their entire journey through the troposphere. In comparison, a perturbation to the potential temperature of a single layer in the mid-troposphere will only change the buoyancy of a parcel as it passes through that height. Parcels of air at other heights may be expected to be unaffected by those perturbations. However, before making this assumption and perturbing only the boundary layer in all subsequent experiments, an experiment is performed to test this hypothesis. This experiment is known as experiment **LEV**.

To ascertain the height at which forecasts of convective storms are most sensitive to initial condition errors, two ‘Lean’ ensembles of perturbation are constructed. In the first ensemble, perturbations are added in the boundary layer at 500m height. In the second, the perturbations are added in the mid-troposphere at 4500m. The forecasts are then allowed to evolve and the ensemble mean difference between them is measured. The variance of the perturbation fields, $\delta\theta$, can be used as a measure of the ‘size’ of the perturbations to allow their growth to be quantified. Table 3.3 shows the ensemble mean perturbation variance, one hour after perturbation insertion at heights of 500m and 4500m for both ensembles.

It can be seen that the perturbation variance is greater at 500m than at 4500m for both cases. As expected, when perturbations are inserted at 500m height the variance at that level is greater than when the perturbations are inserted at 4500m. However, when perturbations are inserted at 4500m height, after one hour the variance is greater at 500m than at the height of insertion. This result strongly implies that the perturbation growth is initially more rapid in the boundary layer than in the mid-troposphere.

Interestingly, these results also show that perturbations initially confined to a single height in the mid-troposphere spread vertically into the boundary layer. Once perturbations have reached the boundary layer they grow rapidly as if the perturbation had been present at that height initially.

	$var(\delta\theta)$ at 500m [K^2]	$var(\delta\theta)$ at 4500m [K^2]
Perturbations inserted at 500m	3.19×10^{-4}	5.35×10^{-6}
Perturbations inserted at 4500m	1.01×10^{-5}	3.65×10^{-7}

Table 3.3: The ensemble mean potential temperature perturbation variance, $var(\delta\theta)$, in the boundary layer (500m) and mid-troposphere (4500m) at 09:30 for perturbations inserted at different heights at 08:30.

Similarly, perturbations inserted in the boundary layer grow and propagate vertically into the mid-troposphere where the variance is greater than when the perturbations are initially inserted at that height. The mechanism by which this vertical perturbation propagation occurs cannot be advective (since the vertical velocities at this time are near zero) but is more likely to be a wave process, i.e. gravity waves or sound waves. Figure 3.4 illustrates the vertical propagation of the perturbation field in ensemble member A ($\delta\theta_A$) during the first ten minutes after insertion. It can be seen that the spread is rapid. Some evidence of wave structures can be seen at 08:40 in experiment LEV. Changnon and Bannon (2005) also found that acoustic, gravity and Lamb waves were generated when applying a thermal perturbation to a model.

These results demonstrate that (as hypothesised) perturbations have more rapid initial growth in the boundary layer than in the free-troposphere and that these perturbations spread vertically to contaminate the forecast throughout the troposphere. Forecasts of convective storms are therefore especially sensitive to initial condition errors in the boundary layer, as was also found by Crook (1996) and Stirling and Petch (2004). It therefore seems sensible for the perturbations in experiment MAIN to be inserted in the boundary layer.

To summarise, in experiment MAIN random perturbation fields are constructed by the convolution of a random number field with a Gaussian kernel. These perturbation fields are then added to and subtracted from the potential temperature, θ , at 500m height at 08:30 (model time). The difference between the model states in forecasts initiated from positive and negatively perturbed initial conditions is then studied. The initial maximum amplitude of the difference in potential temperature, $\delta\theta$, is 0.002K. An ensemble of three pairs is considered to improve the reliability of the results.

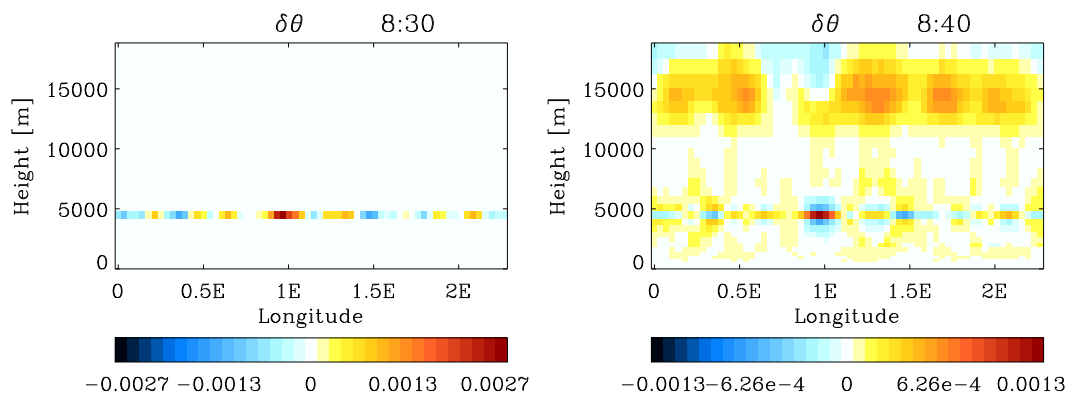


Figure 3.4: Cross-section along 1.16N of $\delta\theta_A$ [K] at 08:30 and 08:40.

3.3 Overview of results from experiment MAIN

To provide an overview of the growth of the perturbations, the *mean square difference*, MSD, in the potential temperature fields at 500m was calculated during the first three hours of the forecast. The MSD is a measure of the distance in phase space between two atmospheric states. In this case, the mean square difference between the potential temperature in the positively and negatively perturbed forecasts is calculated for a single model level. i.e.,

$$MSD = \frac{1}{N} \sum_{i,j} \left(\theta_{i,j}^+ - \theta_{i,j}^- \right)^2.$$

where N is the number of grid points at that model level. The ensemble mean MSD, \overline{MSD} , is then found,

$$\overline{MSD} = \frac{1}{3} (MSD_A + MSD_B + MSD_C).$$

This was calculated at a single height only, to remove complications caused by the vertical growth of the storms. Since the convective cells become taller with time, the arrival of the storm is delayed with height. Figure 3.5 shows the evolution of the ensemble mean MSD with time. It can be seen that for a period of several minutes after the perturbations are inserted they do not grow. Then, at 08:36 there is a step-like jump in the difference between the two forecasts. This difference then remains almost constant, decreasing slightly, for almost an hour before a steady increase in the MSD occurs between 09:20 and 11:00. This growth is initially super-exponential in nature (indicated by the upward curve on the logarithmic y-axis) before tending towards saturation by 11:00. In summary, there are two separate periods of perturbation growth indicating the presence of **two perturbation growth mechanisms dominating** during this time.

The rest of this chapter examines the structure of the perturbations during the period of no growth and during the two periods of growth with an aim of identifying the mechanisms acting in each case.

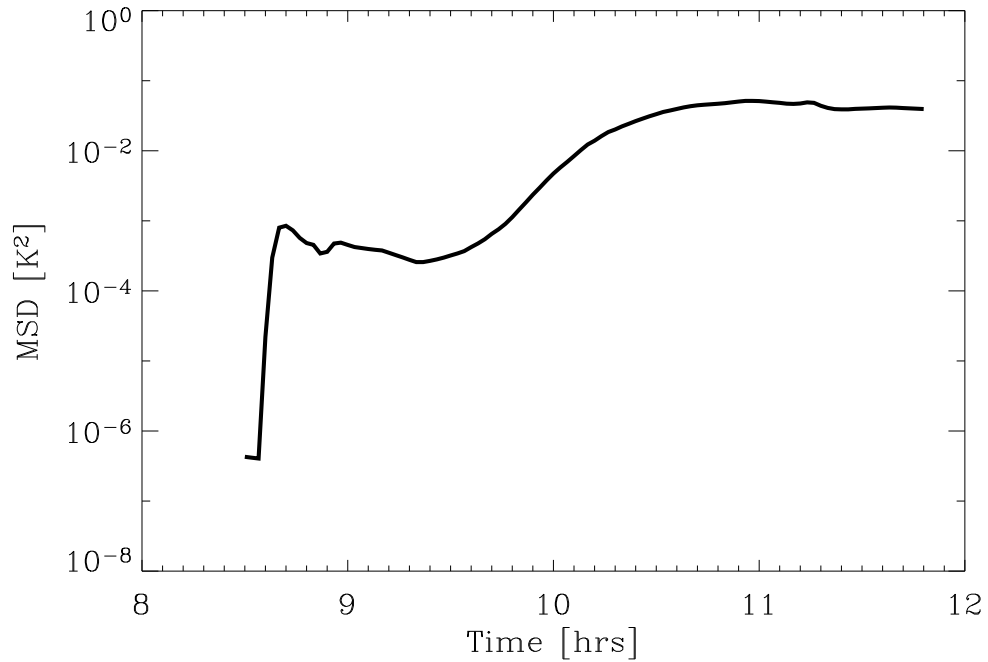


Figure 3.5: The ensemble mean, mean square difference (\overline{MSD}) [K^2], between θ^+ and θ^- at 500m height, as a function of time (in experiment MAIN).

3.3.1 Adjustment of the perturbations by the model

In the first few minutes after the perturbations are inserted, the \overline{MSD} between the forecasts does not grow but decreases slightly (probably due to diffusion in the model). An examination of the structure of the perturbations reveals the perturbations are not unchanging during this time. An adjustment process is observed to take place since the initial θ perturbations are not in hydrostatic balance. It is thought that potential temperature perturbations, $\delta\theta$, change the air density and induce pressure perturbations, δp , through the equation of state. These pressure perturbations then, through the momentum equation, induce vertical motion perturbations, δw , and horizontal motions, δu , which are consistent with the continuity equation. In unsaturated air, moisture acts as a passive tracer meaning that vertical motions advect moist air from the surface upwards and dry air from aloft downwards, creating specific humidity perturbations, δq . If the air becomes saturated then water vapour condenses releasing latent heat causing further potential temperature perturbations, $\delta\theta$.

Figure 3.6 shows the perturbation fields at 08:32 (two minutes after insertion). It can be seen that some of the adjustment takes place almost instantaneously. The initial θ perturbations have been

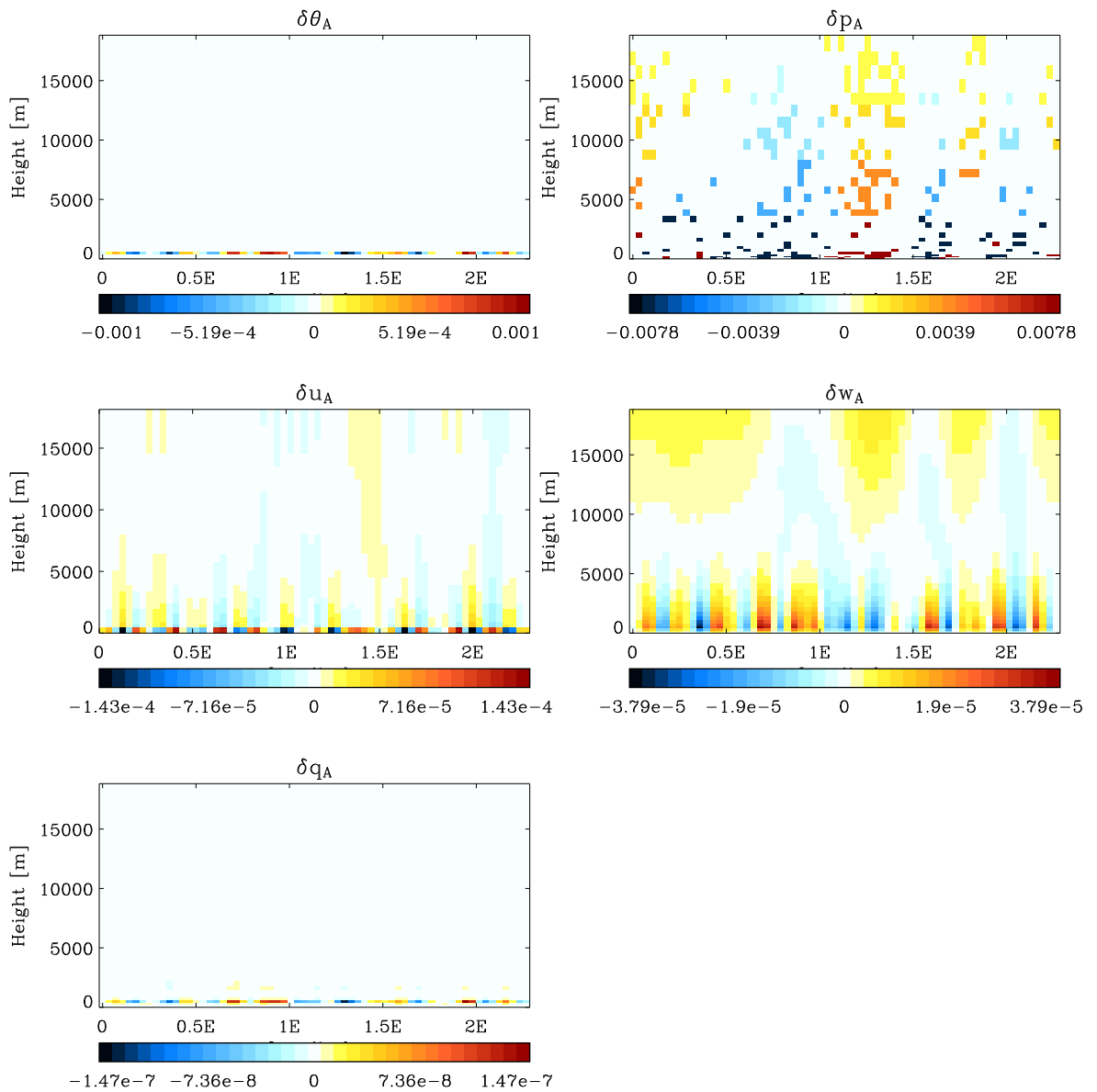


Figure 3.6: Vertical cross-sections along 1.16N latitude at 08:32 (two minutes after perturbation insertion). Perturbation fields of potential temperature ($\delta\theta_A$) [K], pressure (δp_A) [Pa], u-component of wind (δu_A) [$m s^{-1}$], vertical velocity (δw_A) [$m s^{-1}$] and specific humidity (δq_A) [$kg kg^{-1}$]. For θ perturbations of initial amplitude 0.002K inserted at 500m height.

projected onto a number of other variables. The pressure perturbations are so small that the 32 bit precision of the data become evident as large blocks of equal amplitude in the figure.

3.3.2 Investigation of the first perturbation growth mechanism

In Figure 3.5, a step-like increase in the mean square difference was observed to occur at around 08:36. Examination of the structure of the perturbations at this time gives a strong indication as to the likely cause of this abrupt perturbation growth.

Figure 3.7 shows the structure of the potential temperature component of the perturbations, $\delta\theta$, for each ensemble member at 08:30 and 08:40. At the time of insertion (08:30) each ensemble member (A, B and C) has a different random perturbation field with similar amplitude. However, after only 10 minutes it can be seen that significant modification of the perturbations has taken place and all ensemble members exhibit almost identical perturbation structures (although the sign is reversed for member C). In most locations the perturbations have decayed (due to the diffusive nature of the boundary layer and the horizontal diffusion terms in the model) except for a number of grid cells where significant perturbation growth has occurred. The maximum amplitude of the perturbations in these grid cells has increased from 0.002K to around 0.5K in only 10 minutes. These perturbations are only found to grow within the boundary layer (not shown).

It can be shown that the locations of this perturbation growth co-incide with locations where the boundary layer type has been diagnosed differently between the \mathbf{x}^+ and \mathbf{x}^- forecasts by the boundary layer parameterisation scheme (see section 2.1.5). Figure 3.8 shows the boundary layer type as diagnosed by the boundary layer scheme for the \mathbf{x}^+ and \mathbf{x}^- runs at 08:40 in ensemble member A. The lower panel shows the difference between the two. When comparing this difference field with $\delta\theta$ at 08:40 in Figure 3.7 it quickly becomes apparent that the locations of the growing perturbations coincide with grid points in which the boundary layer type is diagnosed differently in the \mathbf{x}^+ and \mathbf{x}^- runs.

The boundary layer parameterisation scheme uses the existing vertical profiles of liquid-frozen water potential temperature, θ_l , and specific total water content, q_t , in the boundary layer to diagnose a boundary layer type (or regime) and hence determine the profiles of mixing in the boundary layer (see section 2.1.5). These results indicate that in the model at certain locations, the diag-

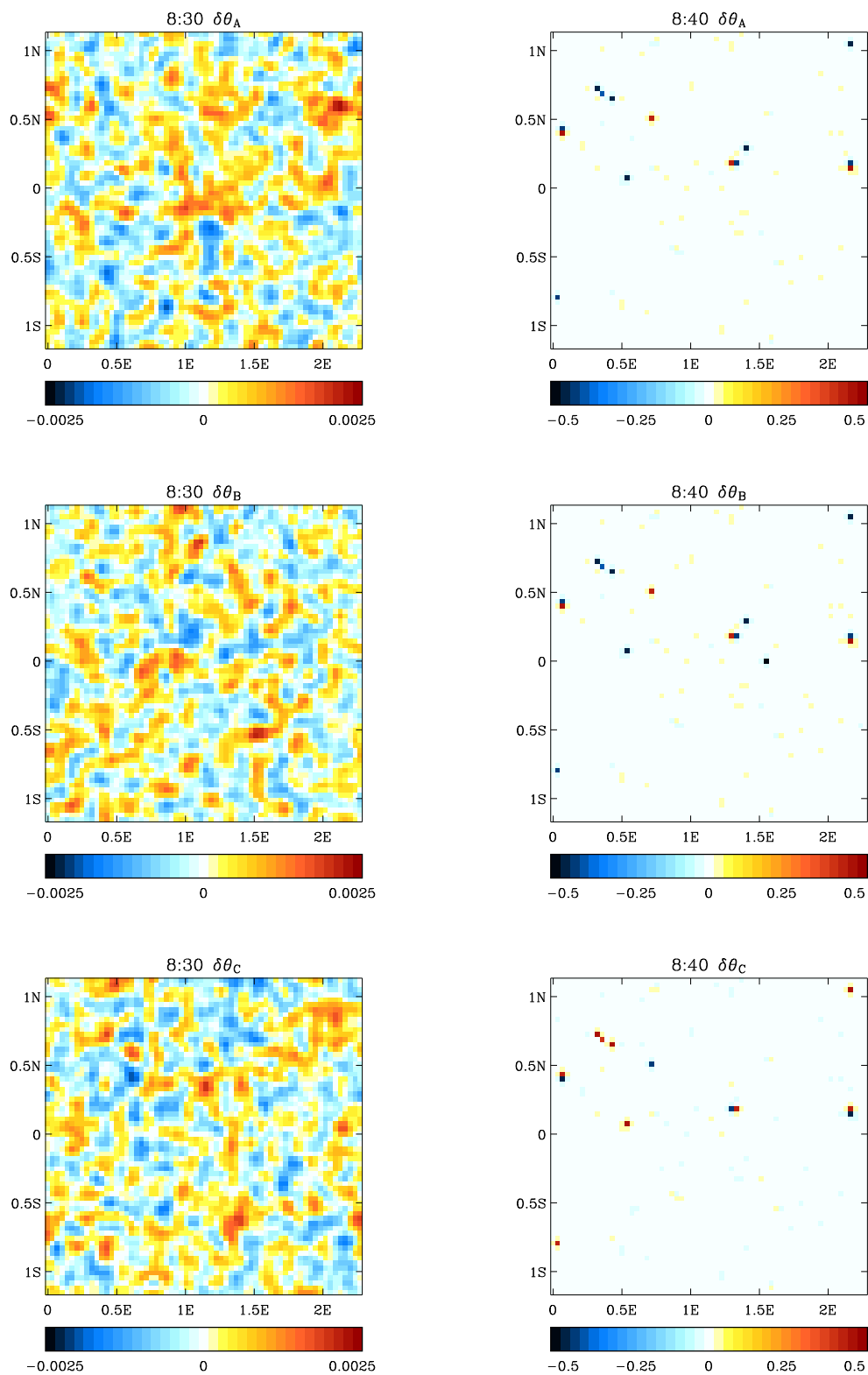


Figure 3.7: Plan views at 500m height of potential temperature perturbations, $\delta\theta$ [K], at time of insertion; 8:30 (left panels) and 8:40 (right panels) for each ensemble member (A, B and C) for perturbations of initial amplitude 0.002K inserted at 500m height. Note that the colour scales used differ between the plots on the left and the right.

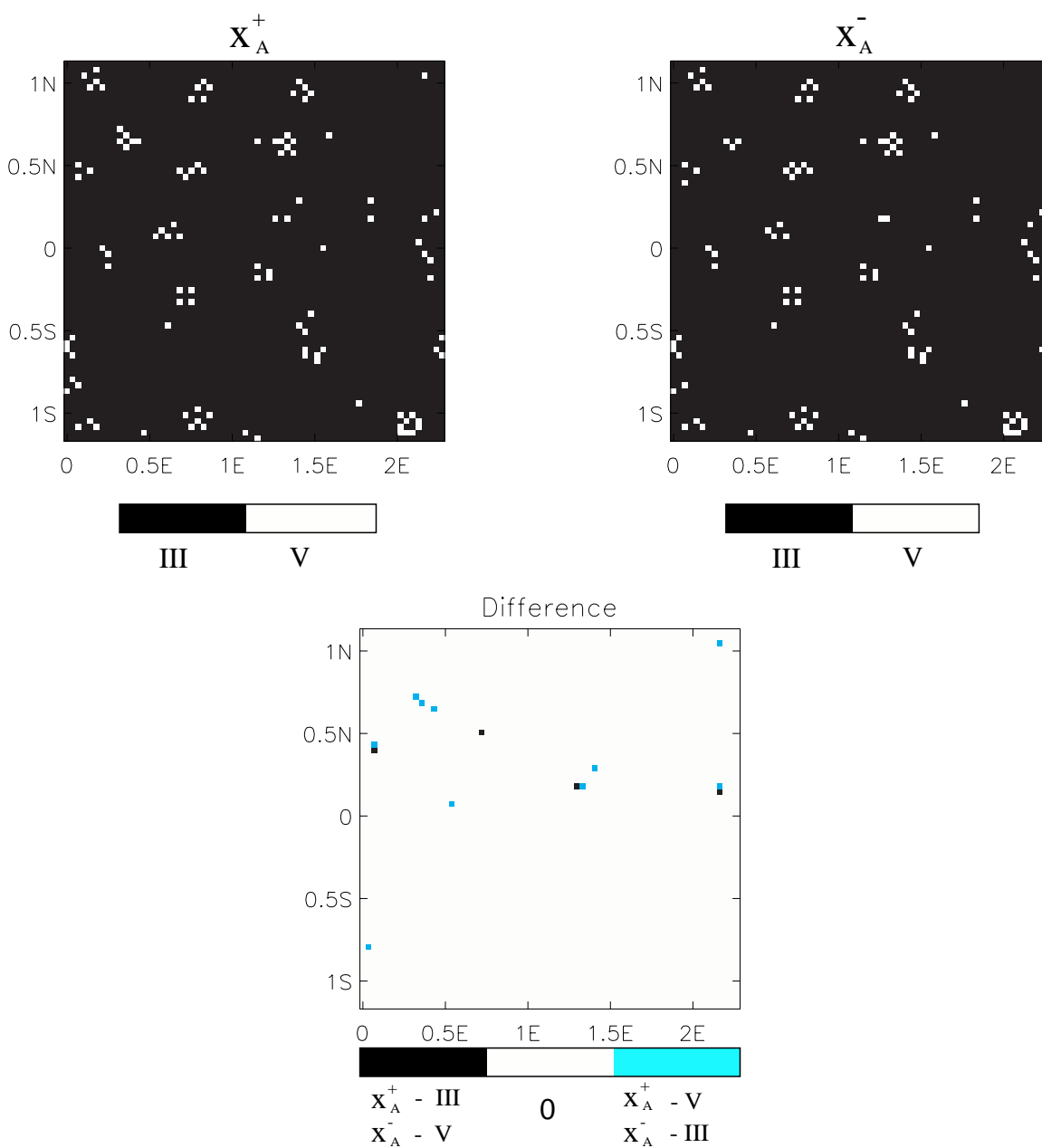


Figure 3.8: Boundary layer type (III-well mixed, V-decoupled stratocumulus over cumulus) in positively perturbed run, x^+ , and negatively perturbed run, x^- , at 8:40 (top panels). Difference of boundary layer type between run x^+ and x^- (lower panel). All results shown for ensemble member A.

nosed boundary layer type is sensitive to small perturbations to the potential temperature within the boundary layer. At these *sensitive boundary layer locations (SBLs)*, the boundary layer type is diagnosed differently between the \mathbf{x}^+ and \mathbf{x}^- forecasts and therefore the evolution of the temperature and moisture structure is also different between the two (due to the different specification of heat and moisture fluxes), resulting in rapid perturbation growth and low predictability. To the author's knowledge this possible error growth mechanism has not been described before. The issue of whether or not this mechanism is simply an artifact of this particular boundary layer parameterisation scheme is discussed in Chapter 7.

In this case, the difference in boundary layer type between the \mathbf{x}^+ and \mathbf{x}^- forecasts is between a 'well-mixed' and a 'decoupled stratocumulus over cumulus' boundary layer (see Figure 3.8). The well-mixed layer is also topped by stratocumulus. Therefore the difference between the two is a layer of cumulus below the stratocumulus deck. In the parameterisation scheme, the depth of the mixed layer is determined by the level of neutral buoyancy of a parcel lifted from the surface. If the mean gradient of q_t with height between the lifting condensation level and the level of neutral buoyancy for the parcel goes above a threshold value then the parameterisation scheme diagnoses a cumulus layer (Lock *et al.*, 2000). Potential temperature perturbations can change the depth of the mixed layer and also induce vertical motions which advect moisture vertically within the boundary layer influencing the mean gradient of q_t leading to the diagnosis of a different boundary layer type. The grid-point nature of these SBLs is probably not a desirable characteristic of the model. However, the conclusion to be drawn from these results regarding the perturbation growth mechanism would not have been different had the areas been more coherent in nature.

Figure 3.9 shows the boundary layer type evolution at one of these SBLs for \mathbf{x}^+ and \mathbf{x}^- . It can be seen that the differences in the boundary layer type between the two forecasts do not happen immediately upon insertion of the perturbations at 08:30. Also the differences are not merely the result of a timing difference in the transition from one boundary layer regime to another; the model states in the two forecasts follow completely different trajectories.

Figure 3.10 compares the potential temperature perturbations (right) with the boundary layer sensible heat flux perturbation (left) to prove that the θ perturbations result from changes to the boundary layer mixing introduced by the parameterisation scheme. Note that the colour scales used to plot $\delta\theta$ have been stretched to allow some of the lower amplitude features to become visible; the colour scale is saturated at either end. It can be seen in the $\delta\theta$ plots (right) that as well as gridpoints

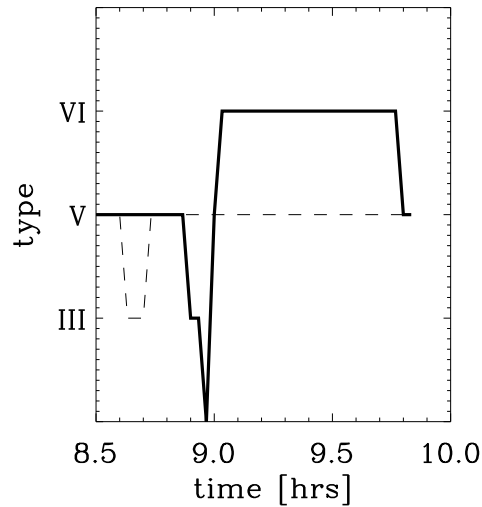


Figure 3.9: Boundary layer type (as diagnosed from the boundary layer scheme) variation with time at a sensitive location where the type varies between the positively perturbed run, x^+ (solid line) and the negatively perturbed run, x^- (dashed line) for perturbations of initial amplitude 0.002K in ensemble member A.

with 0.5K amplitude perturbations associated with boundary layer type differences, perturbations are present with amplitudes of 0.05K which are also associated with boundary layer heat flux perturbations (see plots on left). Further analysis reveals that these locations coincide with locations at which the boundary layer type has been different in x^+ and x^- in the past, but has since become the same again (see Figure 3.11).

In Figure 3.7, it can be seen that the sign of the perturbations in ensemble member C at 08:40 is opposite to those in members A and B. However, the sign of these perturbations is arbitrary and depends on the definition of $\delta\theta$. This can be shown using a simple example; imagine two ensemble members made from two different perturbations fields, x_1^p and x_2^p which are added to and subtracted from the control run, x^c . If the two are equal and opposite, $x_1^p = -x_2^p$, then $x_1^+ = x_2^-$ and $x_1^- = x_2^+$. Therefore it can be seen that the perturbation fields also have opposite sign; $\delta x_1 = -\delta x_2$ i.e. the sign of the perturbation fields is arbitrary and can be different for different initial perturbations.

This new perturbation growth mechanism has been shown to dominate the forecast differences during the first hour of the forecast. The issue of whether or not this perturbation growth mechanism directly influences forecasts of the convective storms is investigated in Chapter 4.

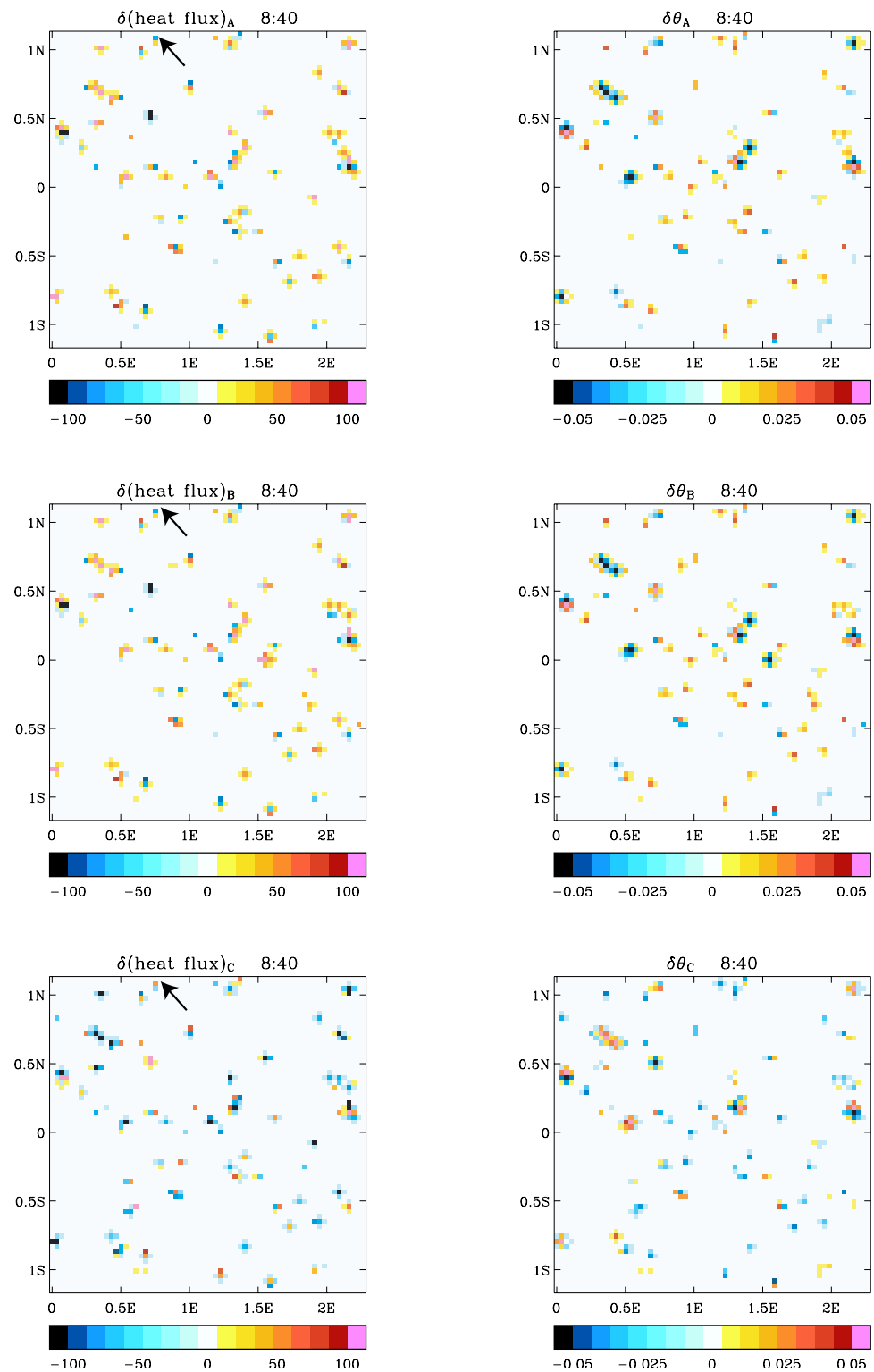


Figure 3.10: Plan views at 500m height of the heat flux perturbation [$W m^{-2}$] for each ensemble member (left) and the potential temperature perturbations, $\delta\theta$ [K], for each ensemble member (right). All plots shown for 08:40. Arrows mark the location of storm B (described in section 4.2). Note that the colour scale used becomes saturated at the highest and lowest values in order to highlight details which would otherwise be obscured.

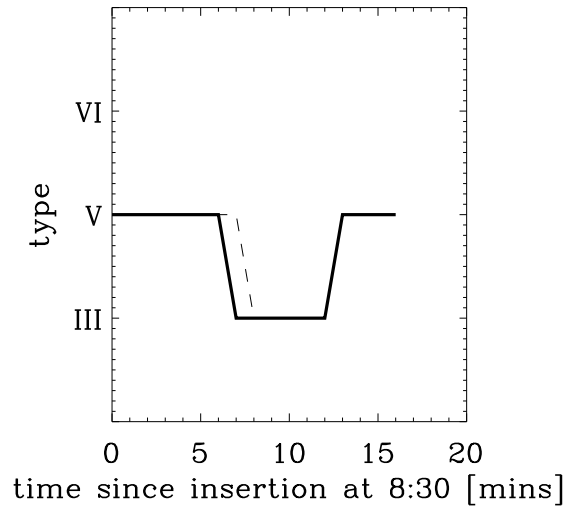


Figure 3.11: Boundary layer type (as diagnosed from the boundary layer scheme) variation with time at a location where large boundary layer fluxes at 8:40 were found to be causing $\delta\theta$ perturbation growth but with the boundary layer type *at that time* being the same in both the positively perturbed run, x^+ (solid line), and the negatively perturbed run, x^- (dashed line), for perturbations of initial amplitude 0.002K in ensemble member A.

3.3.3 Investigation of the second perturbation growth mechanism

After the initial modification of the perturbations by the boundary layer scheme a second mechanism of perturbation growth occurs which coincides with the time that the convective cloud tops rise above the boundary layer (i.e. the initiation of deep moist convection). It is hypothesised that this perturbation growth results from convective instability. To test this hypothesis the structure of the perturbations during the time of this growth is compared with that which would be expected from convective instability, i.e. a change in the intensity of the convective circulations.

The perturbations of amplitude 0.002K inserted here are (initially) too small to change the basic state of the system i.e. the locations of convective storms should not be different between the forecasts, only the strength or timing of the initiation of the cells should change. The diagram in Figure 3.12 illustrates the perturbation field expected from a difference in height of a convective plume between the positively (x^+) and negatively (x^-) perturbed runs. The conceptual model is based on the plume structure described in Chapter 2. θ_e in the saturated air within the plume is higher than θ_e^* in the environmental air, causing a positive potential temperature anomaly inside the storm relative to its environment. Moisture is advected upwards increasing the specific humidity within the plume. The plume is surrounded by slow subsidence. Areas of convergence are found beneath

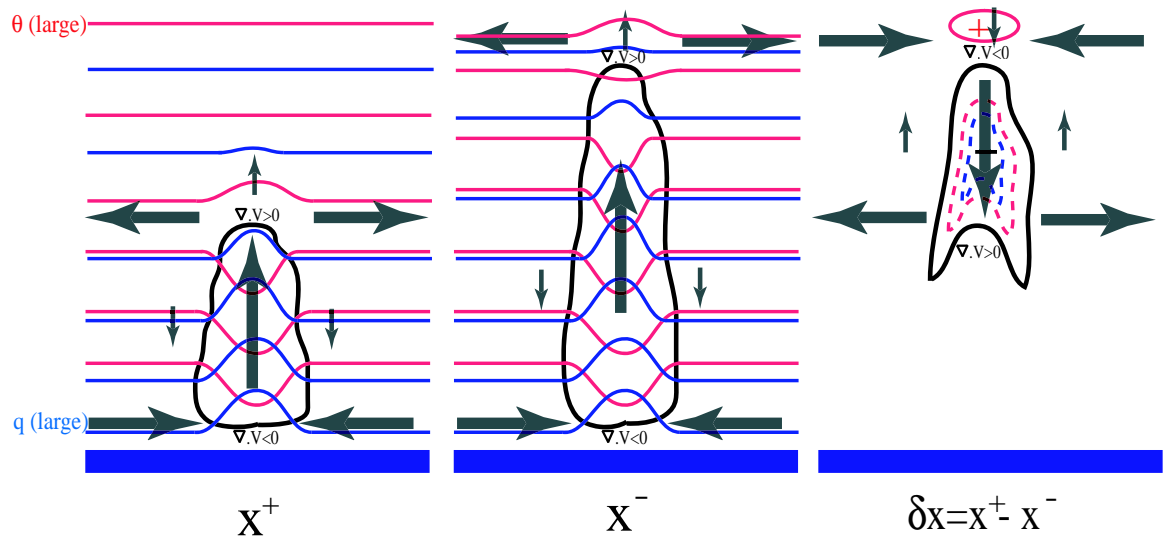


Figure 3.12: A conceptual model of the expected perturbations (right) arising from a height difference in convective plumes between two runs (left and centre). Contours of potential temperature, θ (red) and specific humidity, q (blue dashed) are shown. Dashed contours indicate a negative perturbation. The outline of the cloud, or 100% relative humidity, is marked (thick black). Wind vectors are shown by the arrows along with areas of convergence and divergence.

the cloud base and divergence above the cloud top. Some forced dry ascent of the statically stable air immediately above the rising plume head (as observed in the control run) causes a negative potential temperature anomaly relative to the environment above the cloud. The expected perturbation field (shown in the right hand panel of Figure 3.12) consists of negative $\delta\theta$, δq and δw at the top of the rising plume with divergence at the base of the perturbation and convergence at the top. A positive $\delta\theta$ associated with the dry ascent above the plume is also expected.

It is worth noting that for clarity this diagram has exaggerated the height difference between the positively and negatively perturbed model runs. Figure 3.13 shows cross-sections of vertical velocity at different times (left) along with the vertical velocity perturbation fields, δw , in ensemble member A. The mismatch in amplitudes between δw and w^+ in Figure 3.13 (described later) suggests that the heights of the storms are very similar in both \mathbf{x}^+ and \mathbf{x}^- but different enough for the change in plume strength with height to cause noticeable perturbations. Two storms are labelled (*storm A* and *storm B*) in the full field plots on the left hand side. Storm B has a clear signature in δw associated with it, but storm A has only a very weak signature. The reasons for this will be explored in Chapter 4. It can be seen that at 09:30, 10:00 and 10:10 the perturbation signatures are strongest near the top of the rising convective plumes as expected from the conceptual model.

Figure 3.14 shows the perturbation structure for a selection of variables expected to be affected

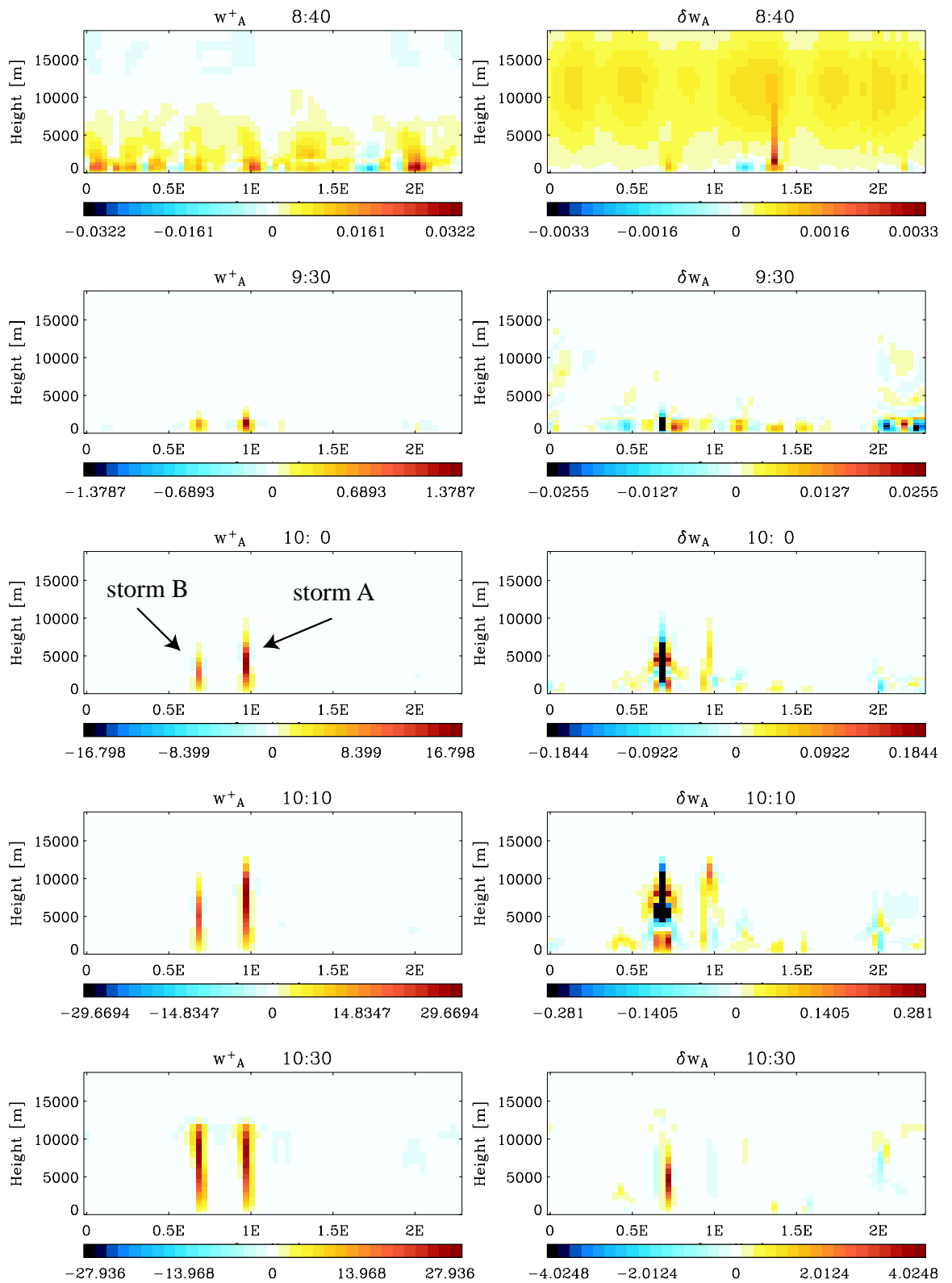


Figure 3.13: Vertical cross-section through 1.16N showing vertical velocity in positively perturbed ensemble member A, w_A^+ [m s^{-1}], evolution with time (left hand panels). Vertical velocity perturbation, δw_A [m s^{-1}], evolution with time (right hand panels). Note that the colour scales change in each plot. Storms A and B are labelled.

by moist convection at a time when the convective plume associated with storm B is growing rapidly. These structures correspond well with those expected from the conceptual model. There is a positive correlation between δw , $\delta\theta$ and δq within the head of the plume. The vertical velocity perturbations in the head are surrounded by perturbations of opposite sign associated with the subsidence around the cell. δp and $\delta(\nabla \cdot \mathbf{V})$ have a positive correlation, i.e. a positive pressure difference corresponds with a relative divergence of the horizontal wind between the forecasts. The u-component (west-east) of the wind perturbation δu also displays the dipole signatures of convergence and divergence associated with the perturbations. The specific humidity perturbations, δq become smaller as the plume rises since the absolute humidity decreases with height resulting in the differences also decreasing with height, whereas the relative humidity perturbations $\delta(RH)$ do not show this height dependence. The plume also has a potential vorticity perturbation, $\delta(PV)$, associated with the diabatic heating caused by condensation within the plume.

Other areas of perturbation growth are also evident in areas away from the two storms in this cross-section, particularly at lower levels. The δp plots show that the atmospheric pressure in the large scale environment is sensitive to perturbation growth within the storms with a negative perturbation field influencing an area significantly larger than the storm itself.

In summary, the conceptual model presented provides a good description of the perturbation fields observed in these simulations. The second period of perturbation growth is associated with differences in the heights of the convective plumes between the perturbed forecasts. Consequently, it can be concluded that convective instability is the mechanism responsible for the perturbation growth between 09:20 and 11:00. The forecast differences resulting from convective instability are two orders of magnitude larger (in a mean square sense) than those resulting from the boundary layer regime changes.

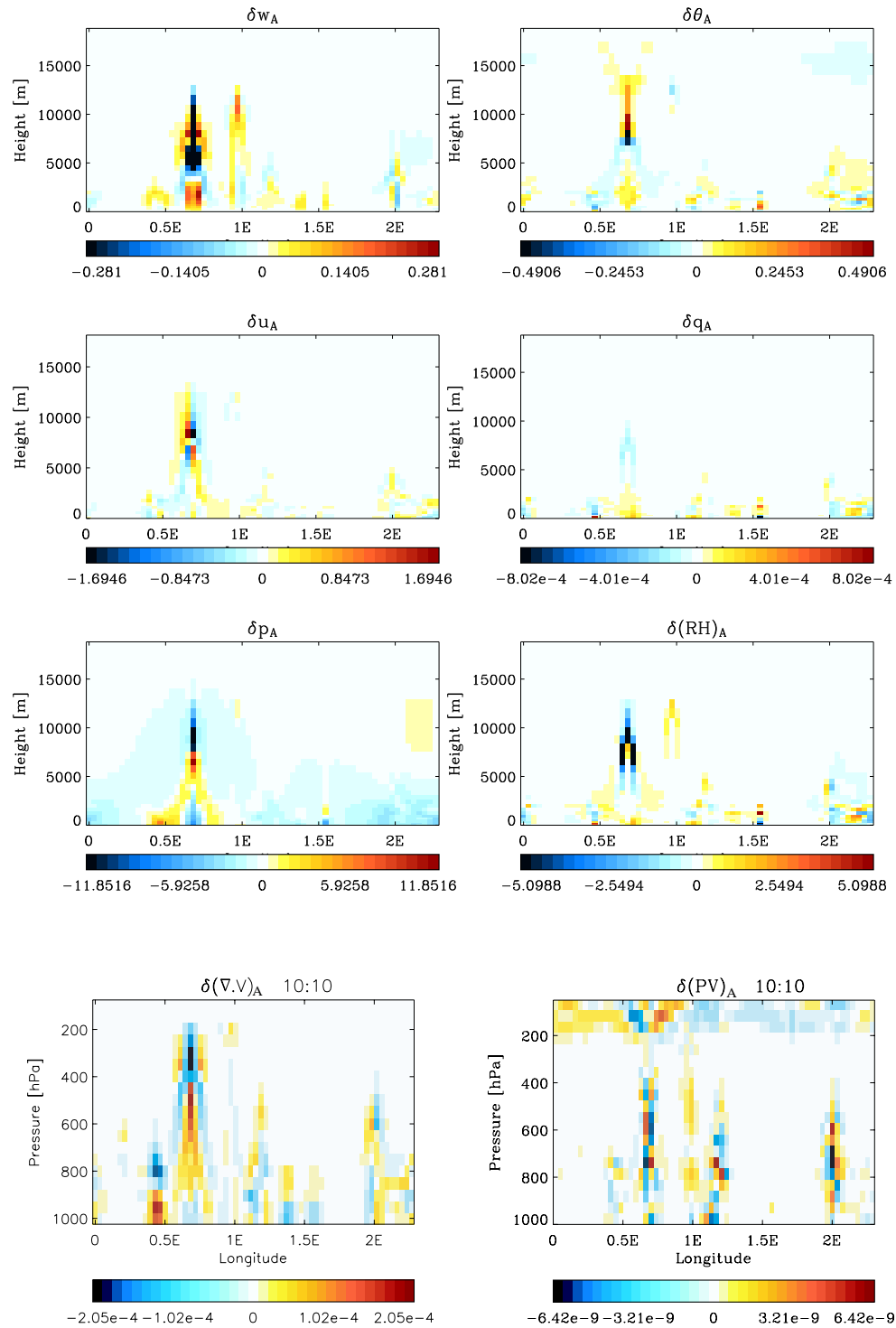


Figure 3.14: Vertical cross-sections along 1.16N latitude at 10:10. Perturbation fields of vertical velocity (δw_A) [ms^{-1}], potential temperature ($\delta \theta_A$) [K], u-component of wind (δu_A) [ms^{-1}], specific humidity (δq_A) [$kgkg^{-1}$], pressure (δp_A) [Pa] and relative humidity ($\delta(RH)_A$) [%], divergence of horizontal wind ($\delta \nabla \cdot V$) [s^{-1}] and potential vorticity (δPV) [$Kkg^{-1}ms^{-2}$]. For θ perturbations of initial amplitude 0.002K inserted at 500m height. Results are shown for ensemble member A in experiment MAIN.

3.4 Chapter Summary

- An experiment (MAIN) was designed to address the first thesis aim of identifying the error growth mechanisms dominating in the first three hours of the forecast. Random perturbations with some spatial coherency were added to and subtracted from the potential temperature field in the control run at 500m height at 08:30 (one hour before the initiation of deep moist convection). The differences between the two forecasts initially had an amplitude of 0.002K and their subsequent evolution was studied. An ensemble of three pairs of positively and negatively perturbed forecasts was considered to improve the significance of the results.
- A separate experiment (LEV) was conducted to determine the relative sensitivity of forecasts of convective storms to uncertainty in θ in the boundary layer compared with that in the mid-troposphere. The results indicated that perturbations initiated in the boundary layer had a more rapid initial growth rate in the boundary layer and mid-troposphere than those initiated in the mid-troposphere during the first hour of the forecast.
- Perturbations initially confined to a single height were observed to propagate vertically throughout the troposphere. Since the effects of the perturbations travelled faster than the speed of the air, wave processes were assumed to be responsible.
- An adjustment to hydrostatic balance was observed which acted to project the unbalanced θ perturbations onto other thermodynamic variables during the first few minutes of the forecast. A slight decay of the perturbations was observed in the mean square difference of θ during this time.
- **Two periods of perturbation growth were observed during the first three hours of the forecast** separated by a period of weak decay. The structure of the perturbations during these times was examined in order to understand the mechanism of that growth.
- **The first perturbation growth mechanism was associated with a change in the boundary layer type** (as diagnosed by the boundary layer parameterisation scheme). The vertical profile of θ in the boundary layer is used by the boundary layer scheme to determine the boundary layer type and hence the mixing profiles. Changes in the θ profile caused by the perturbations resulted in different boundary layer types between the positively and negatively perturbed forecasts at certain sensitive locations. This led to rapid perturbation growth at these locations associated with the different boundary layer heat fluxes resulting from these differences. Consequently, the perturbations in each ensemble member became

very similar after this mechanism had acted as perturbation growth occurred at the same locations in each.

- The second perturbation growth mechanism became dominant one hour into the forecast. The perturbation structure was consistent with a height difference in the convective circulations **indicating that convective instability was responsible for the perturbation growth** during this time.

CHAPTER FOUR

Attribution of two perturbation growth mechanisms to total perturbation growth

In Chapter 3 it was shown that, in this case study, two perturbation growth mechanisms are dominant in the first three hours of the forecast in this case study: firstly, boundary layer regime changes by small potential temperature perturbations led to changes in the heat and humidity structure of the boundary layer; secondly, convective instability led to small perturbations affecting the intensity of the convective storms. It was also noted that the perturbation growth within the convective plumes appeared to vary considerably from storm to storm. In this chapter, the interaction and contribution of the two perturbation growth mechanisms to the total perturbation within the storms are investigated.

In the first section of this chapter, the fact that the magnitude of perturbation growth is variable between different storms is established more rigorously than before. Then the relationship of the perturbation amplitude with various factors is investigated. The results lead to the formation of several hypotheses to explain the mechanism leading to this perturbation strength variability. Several experiments are then performed to test these hypotheses.

4.1 Perturbation growth variability between different storms

4.1.1 Relationship of perturbation strength to storm intensity and initial perturbation amplitude

In section 3.3.3 it was noted that, in experiment MAIN, the perturbations associated with storm B were significantly stronger than those associated with storm A by the time the plumes rose into the mid-troposphere. In this section, the variability of the perturbation strength within storms is further investigated through analysis of many other storms across the domain.

For the purposes of this analysis, a storm is defined as any grid cell where the vertical velocity at 8000m (the approximate height of updraught maxima in this case study) exceeded 15ms^{-1} between 08:30 and 10:30. A time range is used to account for the fact that the storms initiated at slightly different times. Then the absolute magnitude of the maximum vertical velocity occurring at 8000m during this time range, w_{max} , (in the \mathbf{x}^+ run) is used as a measure of the ‘intensity’ of the storm. Similarly, the maximum vertical velocity perturbation at 8000m between 08:30 and 10:30, $|\delta w|_{max}$, is used as a measure of the perturbation ‘strength’. The modulus is taken since the sign of the perturbations is arbitrary. This chapter is concerned with separating the effects of the perturbation growth at sensitive boundary layer locations (SBLs) and perturbation growth due to storm intensity differences. However, some storms formed in different locations for \mathbf{x}^+ and \mathbf{x}^- which resulted in perturbation growth due to a location mismatch; these storms were discounted from the calculations. 18 storms met the criteria both for the vertical velocity maxima (defined earlier) and storm co-location, and were selected for study.

Figure 4.1 shows $|\delta w|_{max}$ plotted against w_{max} for each of the 18 storms. The first point to note is that there is a large range of $|\delta w|_{max}$ (vertical axis) indicating that the enhanced perturbation growth in storm B (marked in blue) was not unique to that storm, but a common characteristic of many storms in this case study. Secondly, there does not appear to be any clear correlation between a storm’s intensity and its perturbation strength. The correlation coefficient (a measure of the *linear* relationship between the two variables) is -0.317. These results indicate that in this case study more intense storms did not necessarily produce larger perturbations.

It might be expected that the maximum strength of the perturbation, $|\delta w|_{max}$, within a given storm

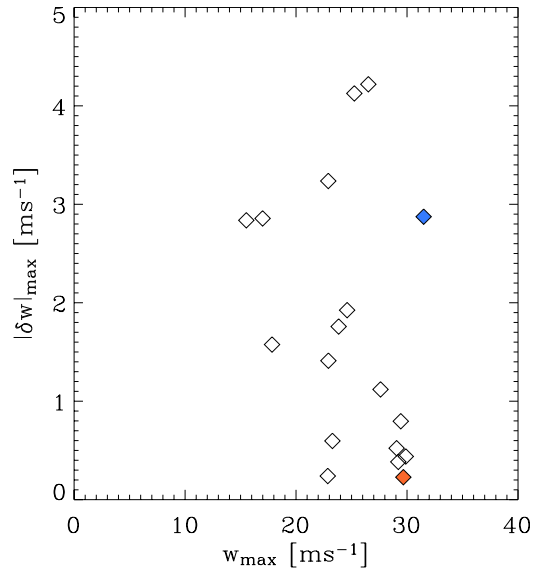


Figure 4.1: Maximum vertical velocity (between 08:30 and 10:30) at 8000m, w_{max}^+ [ms^{-1}], plotted against maximum vertical velocity perturbation (between 08:30 and 10:30) at 8000m, $|\delta w|_{max}$ [ms^{-1}]. Each point represents an individual convective storm. Storms are defined as grid cells where $w_{8000m}^+ > 15ms^{-1}$. Storms that have formed in different locations between x^+ and x^- are not included here. Storm A is marked in red and storm B in blue.

will be related to the initial value of the random potential temperature perturbation, $|\delta\theta|$, inserted at that location. For a convective plume growing in the linear regime, the perturbation strength at a given time will be related linearly to the initial value of that perturbation. It was shown in section 3.3.1 that the perturbations are readily projected from θ onto w through the governing dynamical equations, so it would be expected that an increase in $\delta\theta$ would lead to a similar increase in δw . Figure 4.2 shows $|\delta w|_{max}$ plotted against $|\delta\theta|$ at 08:30 at the location of each storm. Again there does not appear to be a clear relationship between the two variables. The correlation coefficient in this case is 0.308. This suggests that some other factor is responsible for creating the storm-to-storm perturbation strength variability.

Figure 4.3 shows $|\delta w|_{max}$ plotted against $|\delta\theta|$ at 09:50 (the approximate time of initiation for many storms) for each storm. The apparent linear relationship between the two is supported by a correlation coefficient of 0.78. This is consistent with the initial growth of the storms being in the linear regime. This implies that some process occurring between the insertion of perturbations at 08:30 and deep convective initiation at around 09:50 was responsible for the variability of the storms' perturbation strengths. Perturbation growth due to boundary layer regime differences between the different model runs at SBLs was observed to occur during this time (see previous chapter).

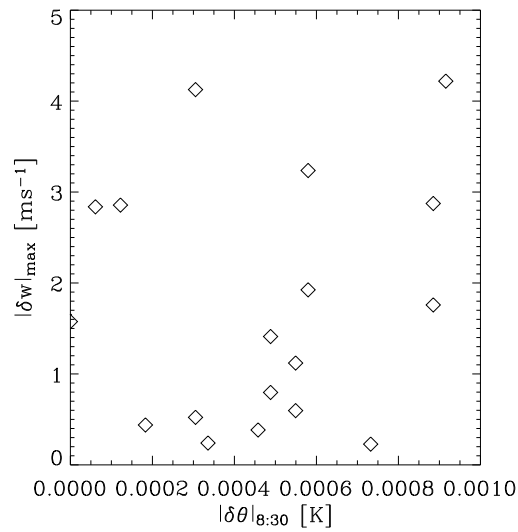


Figure 4.2: Initial potential temperature perturbation at 500m, $|\delta\theta|_{8:30}$ [K], plotted against maximum vertical velocity perturbation (between 08:30 and 10:30) at 8000m, $|\delta w_{max}|$ [$m s^{-1}$]. Each point represents an individual convective storm. NB. Storms defined by grid cells where $u_{8000m}^+ \geq 15 m s^{-1}$. Storms that have formed in different locations between x^+ and x^- are not included here.

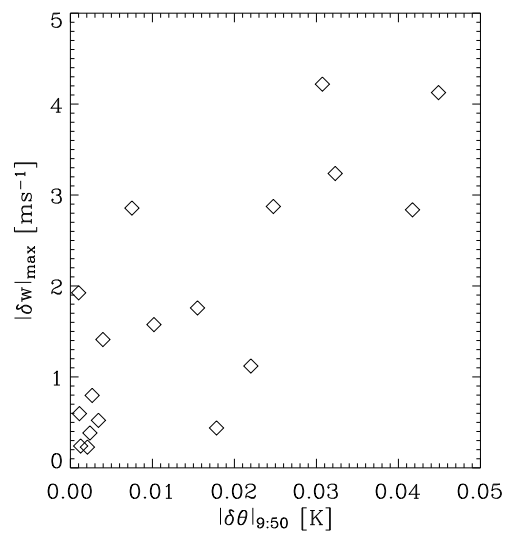


Figure 4.3: Potential temperature perturbation at 500m at 09:50, $|\delta\theta|_{09:50}$ [K], plotted against maximum vertical velocity perturbation (between 08:30 and 10:30) at 8000m, δw_{max} [$m s^{-1}$]. Each point represents an individual convective storm. NB. Storms defined by grid cells where $u_{8000m}^+ \geq 15 m s^{-1}$. Storms that have formed in different locations between x^+ and x^- are not included here.

4.2 Formation of hypotheses to explain the storm-to-storm perturbation variability

The results in the previous section have established that:

1. storm-to-storm perturbation strength variability exists,
2. the perturbation strength within a storm is not related to the storm intensity or the initial value of the random perturbation added at 08:30,
3. some process acting between 08:30 and convective initiation at 09:50 modifies $\delta\theta$ which then grows quasi-linearly within the storms.

It is noted that storm B is located adjacent to an SBL (see Figure 3.10) and that its perturbation growth is larger than that of storm A.

Several hypotheses regarding the factors effecting the perturbation growth variability between the storms are formed:

- **Hypothesis 1:** Perturbation growth associated with boundary layer regime differences at SBLs (i.e. mechanism 1) occurring between perturbation insertion and deep convective initiation increases $|\delta\theta|$ at the locations of some convective storms prior to initiation which results in larger perturbation growth within those storms.
- **Hypothesis 2:** Perturbation growth within a storm is inversely related to its distance from an SBL.

In addition, there is no reason to assume that the two mechanisms are interdependent, which leads to the final hypothesis:

- **Hypothesis 3:** The two perturbation growth mechanisms act independently; any co-location of SBLs and convective storms is purely by chance.

4.3 Testing the hypotheses

4.3.1 Experiment TARGET: Testing Hypothesis 1 by targeting perturbations directly into a rising plume

In experiment MAIN, the boundary layer type changed between the time of perturbation insertion and deep convective initiation. This delay can be reduced by targeting perturbations directly into a plume after its initiation. In addition, insertion of the perturbations above the boundary layer means that it takes time for them to propagate vertically before any boundary layer type differences can occur. These two measures should ensure that perturbation growth by storm intensity differences occurs prior to perturbation growth due to boundary layer type differences. If hypothesis 1 is correct then avoiding perturbation growth by boundary layer regime change will result in the amplitude of the perturbation within a plume being proportional to the initial value of the perturbation inserted at that location.

The experiment designed to test this hypothesis (experiment TARGET) consists of perturbations inserted at 4500m height (i.e. above the boundary layer) at 09:50 such that the rising plume passed through them within 5 minutes of insertion. The same perturbations were used as in ensemble member B in experiment MAIN since these showed a local maxima at the longitude of storm A (see Figure 3.2). In experiment MAIN, the perturbation growth in this ensemble member was much larger within storm B than storm A despite the initial perturbation being smaller at storm B than storm A.

The process by which modifications to the boundary layer θ led to changes in the intensity of the convective plumes was discussed in section 3.2.3. In this experiment, the process is slightly different since the perturbations are inserted above the boundary layer in the mid-troposphere. Previously, the perturbations were made to the potential temperature of the rising surface air parcel, whereas now the perturbations are to the environment within which that parcel rises. However, both of these perturbation methods result in a change in the buoyancy of the air parcel which influences the intensity of the convective plume. A positive perturbation here will result in decreased buoyancy (as the difference in temperature between the parcel and its environment is reduced) whereas a negative perturbation will result in increased buoyancy and therefore increased plume intensity.

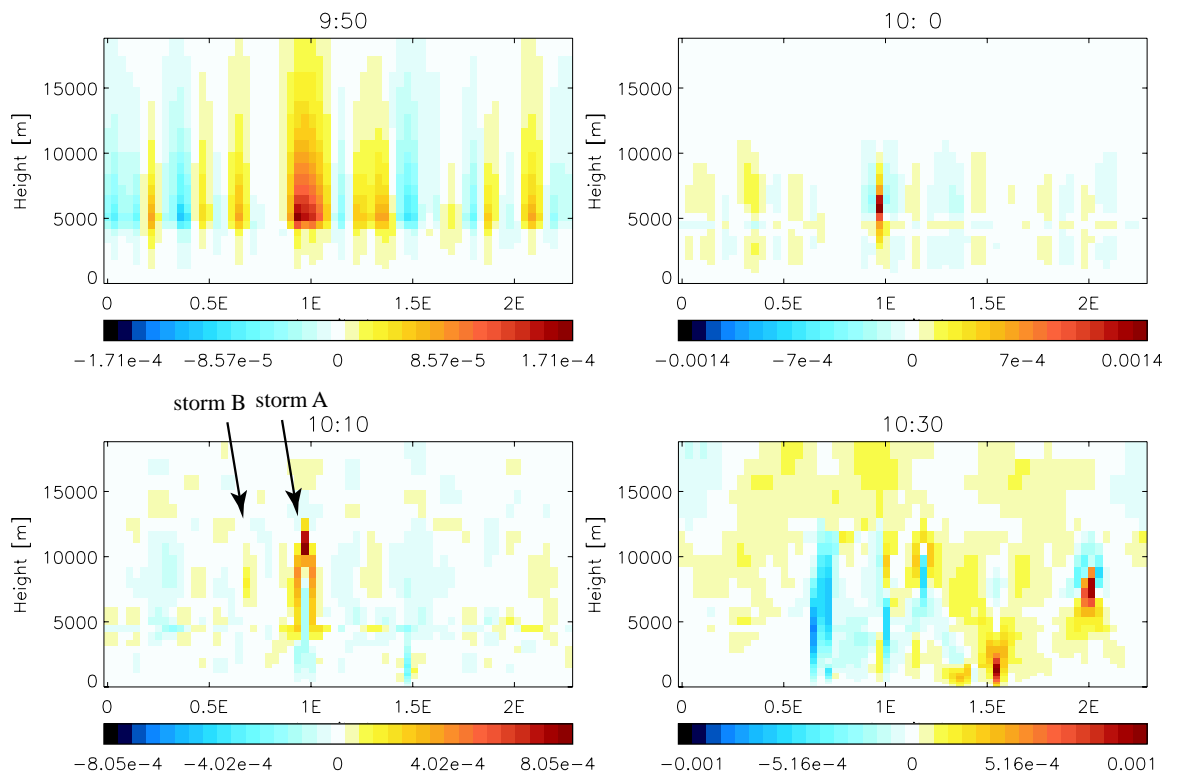


Figure 4.4: Vertical cross-sections of vertical velocity perturbation, δw_B [$m s^{-1}$], at 1.16N latitude at various times. Results are from the experiment where perturbations were targeted directly into the rising plume of storm A (perturbations inserted at 4500m height at 09:50) so that perturbation growth from storm intensity differences could occur before perturbation growth by boundary layer regime differences. The locations of storms A and B are marked with arrows.

Cross-sections showing the time evolution of the vertical velocity perturbations are presented in Figure 4.4. It can be seen that from 10:00 to 10:10 the perturbation signature associated with storm A is stronger than that of storm B (in contrast to the previous experiment where the opposite was true). The perturbation amplitude in both storms is less than that associated with storm B in experiment MAIN (see Figure 3.7) since this time the boundary layer has not had time to grow the perturbations prior to convective initiation. The first boundary layer type differences did not occur until 10:10. The amplitude of the initial random perturbations, $|\delta\theta|$, at the location of storm B was 0.00037K compared with 0.00201K in storm A. These results appear to support hypothesis 1.

4.3.2 Testing Hypothesis 2 using a comparison of perturbation growth between storms

In section 3.3.3 it was noted that the perturbation growth in storm B was larger than that in storm A and also that a SBL was found in the vicinity of storm B. This led to Hypothesis 2 which asserted

that the nearer a storm was to a SBL, the larger the perturbation associated with that storm. This can be tested through analysis of the distribution of SBLs relative to the convective storms in experiment MAIN.

Again, a storm is defined as any grid cell where the vertical velocity at 8000m exceeded 15ms^{-1} between 08:30 and 10:30. Figure 4.5 shows the locations of the convective storms at 10:30 overlaid on a mask of the locations where boundary layer type differences occurred between \mathbf{x}^+ and \mathbf{x}^- from 08:30 to 08:40 (during the time when perturbation growth is dominated by differences in boundary layer type). Storms which have $|\delta w|_{max} > 1\text{ms}^{-1}$ are marked by a '+' indicating 'large' perturbation growth, while those with $|\delta w|_{max} \leq 1\text{ms}^{-1}$ are marked by a '-' indicating 'small' perturbation growth. Storms which were not common in both \mathbf{x}^+ and \mathbf{x}^- are not included in this analysis.

It can be seen that several storms with large perturbation growth are located near SBLs, for example storm B. However, there are also several storms with large perturbation growth which lie

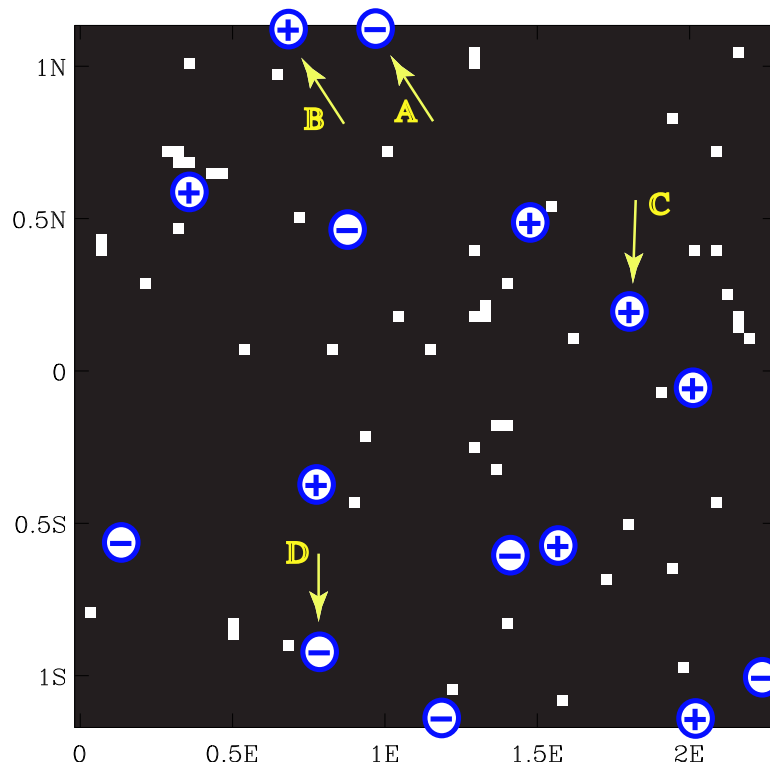


Figure 4.5: Plan view of locations where the boundary layer type is diagnosed differently between \mathbf{x}^+ and \mathbf{x}^- in the time range 08:30 to 08:40 (squares), with the locations of convective storms with vertical velocity (w^+) at 10:30 greater than 15ms^{-1} at 8000m superimposed (circles). A '+' indicates $|\delta w|_{max} > 1\text{ms}^{-1}$ within that storm and a '-' indicates $|\delta w|_{max} \leq 1.0\text{ms}^{-1}$. The locations of storms A,B,C and D are indicated with arrows.

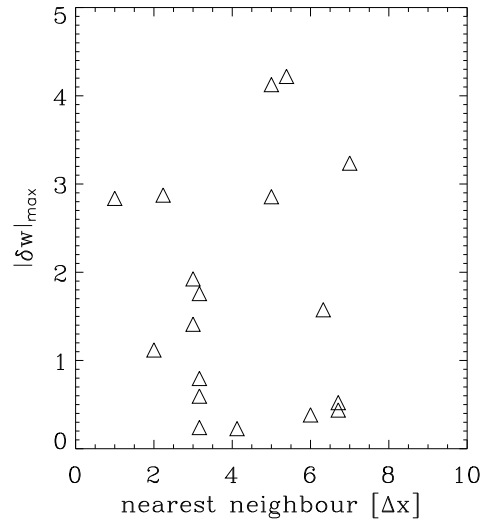


Figure 4.6: $|\delta w|_{max}$ [ms^{-1}] at 8000m plotted against the distance to the nearest sensitive boundary layer location [Δx] within each storm with updraughts exceeding $15ms^{-1}$.

further away from sensitive boundary layer locations (e.g. storm C in Figure 4.5). Similarly, there are some storms with small perturbation growth which lie close to SBLs (e.g. storm D).

This apparent contradiction of Hypothesis 2 is backed up further in Figure 4.6 which shows $|\delta w|_{max}$ plotted against the distance (in grid cells) to the nearest SBL for each storm with updraughts exceeding $15ms^{-1}$. If the hypothesis were correct then the perturbation strength would be inversely related to the distance from a sensitive boundary layer area. This does not appear to be the case. Furthermore, the correlation coefficient between the two of 0.0107 confirms that there is no linear relationship. These results strongly suggest that Hypothesis 2 is incorrect. A second test of the hypothesis is presented in the next section.

4.3.3 Experiment SWAP: Testing Hypothesis 2 by attempting to move storm B away from an SBL

Hypothesis 2 was based on the fact that storm B (which was located adjacent to an SBL) had larger perturbation growth associated with it than storm A (which was not adjacent to an SBL). If the hypothesis is correct then moving storm B away from the SBL should reduce the perturbation growth within it. Similarly, moving storm A nearer to an SBL should increase its perturbation growth. However, if the larger perturbation growth in storm B were not related to the nearby SBL

but an internal property of the storm then the perturbation growth should remain large wherever the SBL is moved to.

When the model was initialised at 00:00 white noise was added to θ at the lowest model level to provide lateral density contrasts and allow convective circulations to develop. In Chapter 2 it was found that the location of the convective plumes was determined by this white noise since these were the only inhomogeneities present in this case study. Since the horizontal winds prior to convective initiation were negligible, it can be expected that storms form in locations where the local environmental conditions are particularly conducive to convective initiation. In this experiment (experiment SWAP) an attempt is made to swap the locations of storm A and storm B by swapping the initial θ white noise in the local environments of each storm at 00:00. If the increased perturbation growth in storm B was due to the nearby SBL then the effect of moving the storm away from that location to a new location further from any SBLs would be to reduce the perturbation growth within that storm.

Two boxes (A and B) are defined centered around storms A and B respectively. Since these storms occurred near the periodic boundary of the domain the boxes also cross the boundary. The boxes do not overlap, but are adjacent to each other. The θ white noise added at 00:00 in \mathbf{x}_A is then swapped between boxes A and B in a new run, \mathbf{x}_S . Figure 4.7 shows θ_S and θ_A at 00:00 with the outlines of the boxes superimposed. The bottom panel shows the difference between the two and illustrates the fact that the white noise is unaltered everywhere except within the defined boxes.

The vertical velocity in both runs, w_A and w_S , are compared in Figure 4.8. The individual convective storms are visible as areas of strong upward motion surrounded by weaker subsidence. It can be seen that there are a number of differences between \mathbf{x}_A and \mathbf{x}_S . Some storms formed in the same locations (e.g. storm X), however a number of storms cannot be matched between the two runs. No storms formed at the locations of storms A and B in \mathbf{x}_S (centre panels). The changes made to the potential temperature within the two boxes influenced the locations of convective storms right across the domain. This is an unexpected result since it had been expected that the only differences would occur within the two boxes. At 08:40, the differences in w between the two runs (top right) are concentrated within the areas of the two boxes (for box outlines see Figure 4.7) but they are not restricted to that region. These differences increase with time such that by 09:50 (lower right) the differences are spread evenly across the domain.

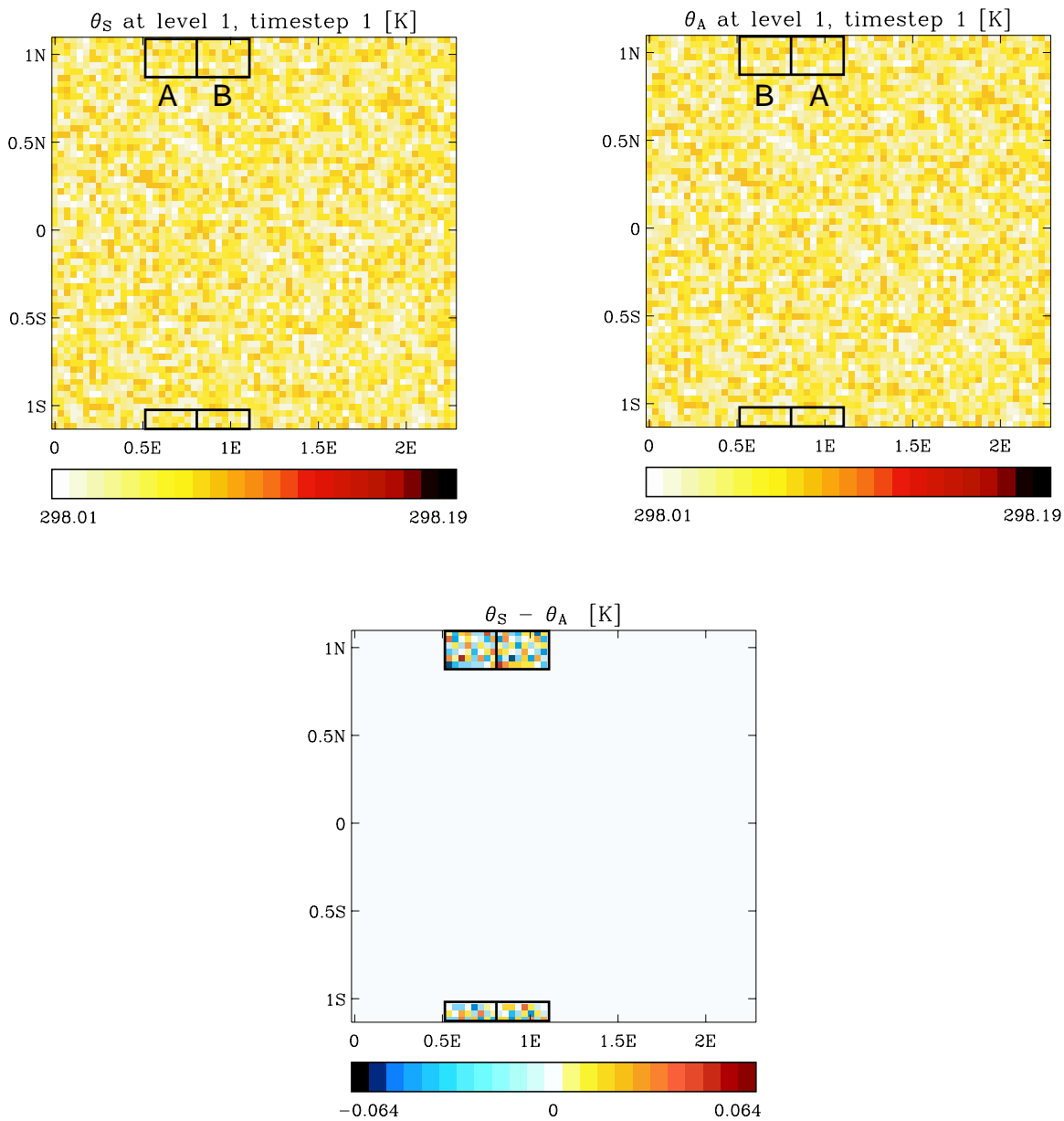


Figure 4.7: Plan views of potential temperature, θ [K], at lowest model level at 00:00 for x_S (top left) and x_A (top right). The lower panel shows the difference between the two. The boxes defined around storms A and B are marked for clarity.

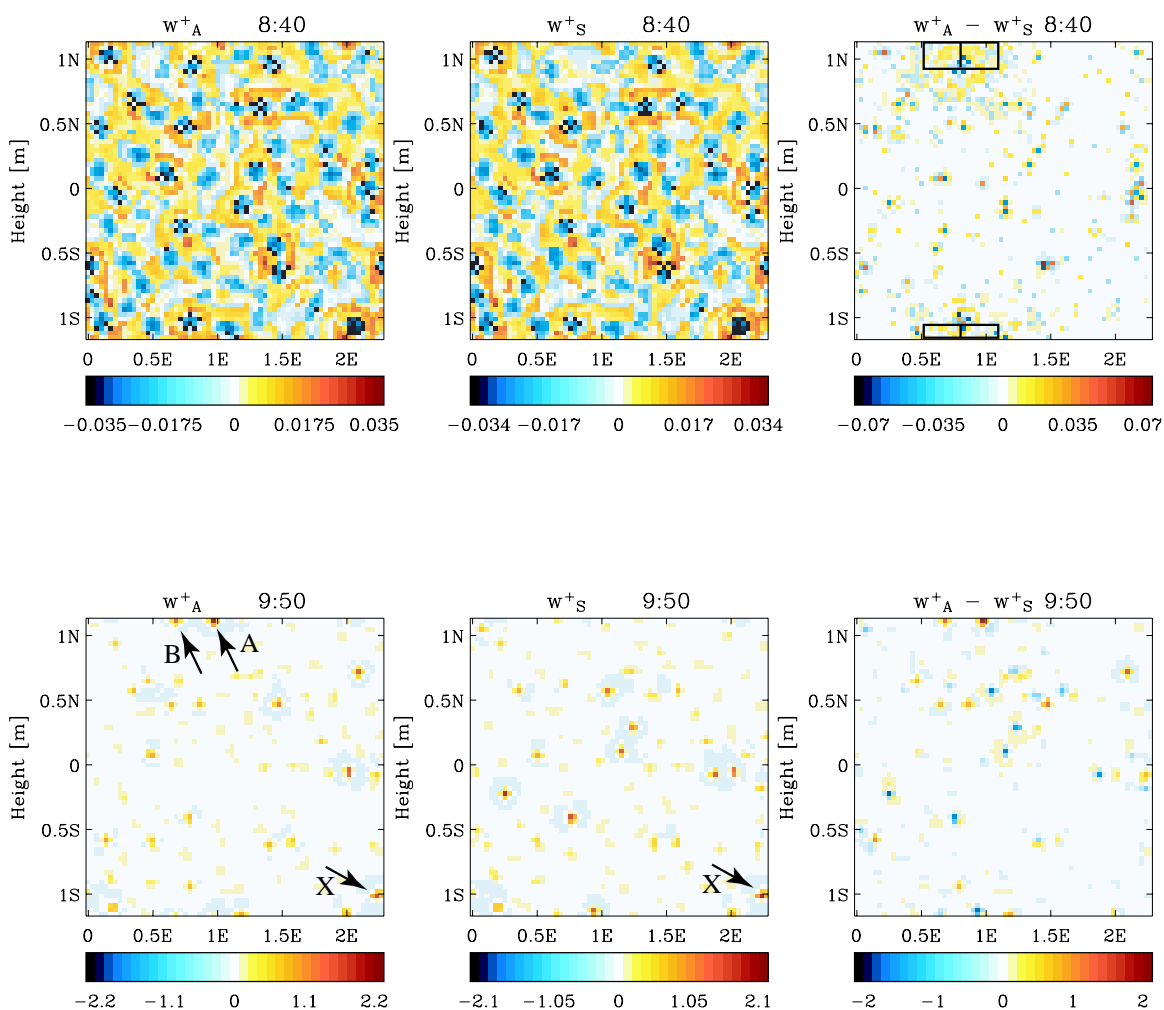


Figure 4.8: Plan views of vertical velocity, w [ms^{-1}], at 500m x_A (left panels) and x_S (centre panels) and the difference between the two (right panels), at two different times. The locations of storms A, B and X (see text) are marked.

It had been assumed that since the advection was negligible prior to convective initiation, the local environment was the only factor responsible for determining if a storm triggered there. However, these results indicate that wave interactions occur which propagate information and influence convective initiation at a distance far greater than that possible by advection alone.

A previous study by Cohen (2001) investigated the timescale of convective adjustment towards an equilibrium state after an increase in the destabilisation rate. It was noted that the timescale of adjustment was linearly related to the mean cloud spacing and that this timescale was similar to the time taken for gravity waves to propagate between the individual clouds. Here it appears that some wave interactions are also occurring during the destabilisation process which influence the locations of the convective storms. Other studies (e.g. Marsham and Parker (2006)) have also shown evidence of gravity waves influencing the secondary initiation of convective storms in large eddy models and in observational data.

These results suggest that the factors governing the locations of convective initiation are more complicated than expected when designing the experiment. Unfortunately this also means that the method used here cannot allow storms to be “cut and pasted” from one location to another and prevents understanding about the contribution of the two perturbation growth mechanisms to the total perturbation growth.

4.3.4 Testing Hypothesis 3: determining if the two mechanisms act independently

Hypothesis 3 suggests that the location of the convective storms is not determined by the location of the SBLs, i.e. the two perturbation growth mechanisms found in this thesis act independently and that any co-location of the two happen only by chance. This can be tested by comparing the distribution of the locations where each mechanism occurs, i.e. comparing the locations where the boundary layer type is different between perturbed runs leading to perturbation growth, and the locations of the convective storms with their associated perturbation growth. Two masks are defined. Mask S marks the locations of the convective storms with maximum vertical velocity at 8000m exceeding 15ms^{-1} , at any time up to 10:30. Mask B indicates the locations where the boundary layer type (as defined by the boundary layer parameterisation scheme) becomes different in the positively and negatively perturbed runs within 10 minutes of perturbation insertion i.e. Mask B marks the SBLs.

Figure 4.9 shows Mask B (left) and Mask S (right). There appears to be little spatial relationship between the two. To quantify the degree of spatial correlation between the two masks, the distribution of distances of the nearest SBL to each storm was calculated. This can then be compared with the distribution between two random masks, Masks R1 and R2. To construct the random masks, two random number fields were generated with a uniform distribution between 0 and 1. Then a threshold value was defined below which the mask was set to 0 and above which the mask set to 1. The number of points in the two location masks, Mask S and Mask B, are different (24 convective storms compared with 55 SBLs). For a fair comparison, the number of points in Masks R1 and R2 were set to match those in Masks B and S respectively by adjusting the threshold value until the correct number of points was achieved in each mask. Masks R1 and R2 are shown in Figure 4.10.

To reduce the sampling error in the comparison a further 999 pairs of random masks were constructed in the manner previously described. The distribution of the distance to the nearest point in Mask B from each point in Mask S is shown by the solid line in Figure 4.11; correspondingly, the mean distribution of the distances between points in each pair of random masks is shown by the dashed line in Figure 4.11 along with standard error bars. A bin size of $3\Delta x$ was chosen to reduce noise in the distribution resulting from the small sample size. The similarity of the histograms from the data and the randomly generated masks suggests that the spatial distribution of Masks S and B are indeed unrelated to each other. This result supports hypothesis 3.

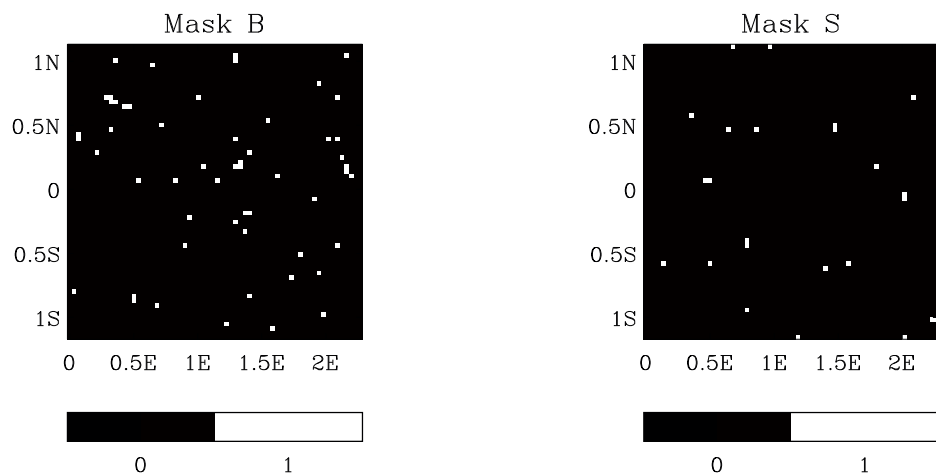


Figure 4.9: Mask B (left) indicating the locations where the boundary type is different between \mathbf{x}^+ and \mathbf{x}^- between 08:30 and 08:40. Mask S (right) indicating where the vertical velocity at 8000m exceeds $15ms^{-1}$ at any time up to 10:30. [*1* -condition met, *0*-condition not met]. There are 55 points in Mask B and 24 in Mask S.

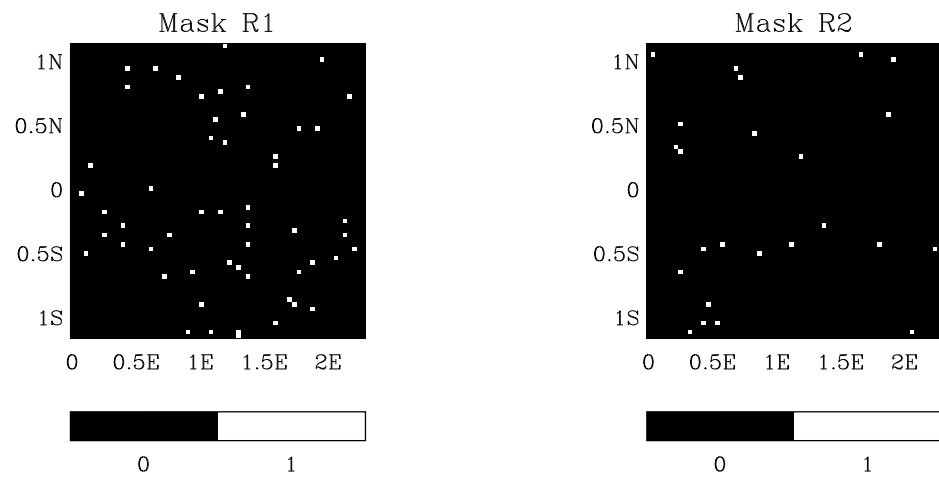


Figure 4.10: Mask R1 (left) and Mask R2 (right). There are 54 points in Mask R1 and 24 in Mask R2.

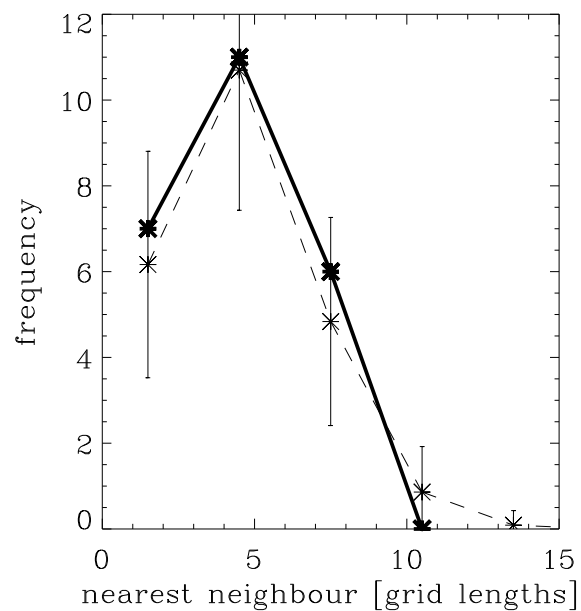


Figure 4.11: Histogram showing the distribution of nearest location '1' in Mask B to each '1' in Mask S (thick solid line) and the mean of the same between 1000 pairs of random masks (dashed line). Standard error bars are shown. The bin size in all histograms is $3\Delta x$.

4.4 Chapter summary

- The fact that the strength of the perturbations within the convective plumes was variable between different storms was demonstrated through an analysis of 18 storms in the original experiment. It was found that there was no direct relationship between the maximum vertical velocity, w_{max} , at 8000m in the plumes (the ‘intensity’ of the storms) and the maximum vertical velocity perturbation, $|\delta w|_{max}$, at the same location. Similarly, the initial potential temperature perturbations, $|\delta\theta|_{08:30}$, did not seem to govern $|\delta w|_{max}$. However, it was found that δw_{max} was linearly related to $|\delta\theta|_{09:50}$ (where 09:50 is the time of convective initiation). Therefore, some process occurring between the insertion of perturbations and convective initiation was responsible for determining the perturbation strength within the storms.
- This led to **Hypothesis 1** which stated that perturbation growth due to boundary layer type differences between runs at sensitive boundary layer locations (SBLs) was the process responsible for the variability of perturbation strength between different storms. The hypothesis was tested in an experiment (TARGET) where perturbations were inserted above the boundary layer timed such that the rising convective plumes passed through them before any perturbation growth at SBLs could occur. It was found that in this experiment the perturbation growth in storm A was larger than in storm B and that the initial value of $|\delta\theta|$ at the location of storm A was also larger than that at storm B. **These results supported Hypothesis 1.**
- In experiment MAIN, it was noted that storm B triggered adjacent to an SBL and that the perturbation growth in this storm was larger than that in storm A (which was not next to an SBL). This led to **Hypothesis 2** which stated that the perturbation strength within a storm was inversely related to the distance from the nearest SBL. This was tested by examining perturbation growth in the 18 largest storms and comparing it with distance to the nearest SBL. **The results showed no clear relationship between the two, in apparent contradiction of Hypothesis 2.** A second method of testing the hypothesis (experiment SWAP) involving an attempt to “cut and paste” a storm from a location near an SBL to a new location away from any SBL by moving the white noise in θ added at 00:00 in the storms environment to a new location. Unfortunately it was found that the method was flawed since modification of θ in the vicinity of a storm led to changes in the locations of convective storms across the domain. Since horizontal advection was negligible prior to convective initiation it was thought that some propagation of differences by waves must have been tak-

ing place. The results provided interesting information on the factors governing the location of convective initiation. However they did not allow any conclusions to be made about the validity of the second hypothesis.

- Finally, **Hypothesis 3** stated that the two perturbation growth mechanisms (perturbation growth due to boundary layer regime differences and perturbation growth within convective plumes) acted independently i.e. a sensitivity of the boundary layer type to small θ perturbations did not necessarily lead to the initiation of a storm with its associated perturbation growth within it; any co-location of the two was purely coincidental. This was tested by looking at the spatial relationship between two masks which identified locations where each mechanism took place. The distribution of distance to the nearest SBL for each storm was calculated and compared with the mean distribution from 1000 pairs of randomly generated masks involving the same number of points as the data. **The results indicated that the storms were randomly distributed with respect to the SBLs, supporting Hypothesis 3.**

CHAPTER FIVE

Quantification of the perturbation growth as a function of spatial scale

In Chapter 3 the first thesis aim was fulfilled by establishing that two error growth mechanisms dominate during the first three hours of a forecast of convective initiation; the first associated with boundary layer regime changes, and the second associated with convective instability. In Chapter 4 these two mechanisms were shown to act independently, i.e. a location at which the boundary layer regime is sensitive to small potential temperature perturbations does not necessarily coincide with the location of convective initiation. While the perturbation growth was quantified in a mean square sense in Chapter 3, this chapter addresses the **second thesis aim** (see section 1.3) of quantifying the growth rate of initial condition errors in the forecast *as a function of spatial scale*.

Fourier analysis is used to quantify the growth of potential temperature perturbations as a function of horizontal spatial scale during the first 100 minutes of the forecast. Information of this kind is useful as it allows an understanding of the likely skill of forecasts of features at different scales. Furthermore, the design of a convective scale data assimilation system (necessary for accurate convective scale weather forecasts) requires information on the initial growth rate of errors and the degree to which a linear approximation of the subsequent growth is valid.

The first section of this chapter describes the Fourier techniques used to quantify the perturbation growth as a function of spatial scale. The *initial perturbation growth rate* is then calculated and its scale dependence compared with that expected from the linear theory of convection. Finally, the transition from the linear regime into non-linear growth is quantified using the *relative non-linearity* as defined by Gilmour *et al.* (2001).

5.1 Fourier analysis of the perturbations

Just as any point in state space can be described by the weighted sum of orthogonal basis vectors, any point in function space (where each point describes a unique function) can be described by the weighted sum of orthogonal basis functions.

A *Fourier series* uses sine and cosine functions as the orthogonal basis functions from which any periodic function can be described (e.g. Stein and Shakarchi (2003)). Hence any periodic function, $f(x)$, can be described by,

$$f(x) = \frac{1}{2}a_0 + \sum_{n=1}^{\infty} a_n \cos(nx) + \sum_{n=1}^{\infty} b_n \sin(nx)$$

where a_n and b_n describe the weightings of each cosine and sine function respectively.

Euler's formula describes sine and cosine functions in terms of complex exponentials. This can be used to define the Fourier series in terms of complex exponentials where the coefficients, A_n , have both real and imaginary parts ($A_n = \Re(A) + \Im(A)$), i.e.

$$f(x) = \sum_{n=0}^{\infty} A_n e^{inx}.$$

Applying this representation to the two dimensional *discrete* function representing the potential temperature perturbation, $\delta\theta$, at a height z , gives,

$$\delta\theta_z(x, y) = \sum_{k=0}^{N-1} \sum_{l=0}^{M-1} A_{k,l} e^{2\pi i(\frac{kx}{N} + \frac{ly}{M})}.$$

where k represents the wavenumber in the east-west (x) direction, l the wavenumber in the north-south (y) direction, N is the number of columns and M is the number of rows in the model domain. The complex coefficients, $A_{k,l}$, can be calculated using a *Fourier Transform*. The *Fast Fourier Transform* (FFT) is a computationally efficient discrete Fourier transform algorithm which calculates the coefficients as follows,

$$A_{k,l} = \frac{1}{MN} \sum_{x=0}^{N-1} \sum_{y=0}^{M-1} \delta\theta_z(x, y) e^{-2\pi i(\frac{kx}{N} + \frac{ly}{M})}.$$

The *spectral energy densities*, $a_{k,l}$, can then be calculated using the square of the norm of the complex coefficients,

$$a_{k,l} = 2 \left(\Re(A_{k,l})^2 + \Im(A_{k,l})^2 \right)$$

where the multiplication by two is applied to all wavenumbers below the Nyquist wavenumber ($k_{nyquist} = l_{nyquist} = 32$) to account for folding above the Nyquist wavenumber.

These *spectral densities* describe the relative contribution of different wavenumbers in the north-south and east-west directions to the total θ perturbation field, i.e. they describe the *power spectrum* of the perturbation. However, all results so far indicate that this case study is horizontally isotropic, therefore the directional information provided by the two dimensional FFT can be converted into a scalar power spectrum. A scalar (non-directional) wavenumber, r , can be defined as follows,

$$r^2 = k^2 + l^2.$$

By binning together spectral densities with equal values of r , the scalar spectral densities, a_r , can be calculated. This provides a non-directional (scalar) power spectrum of the potential temperature perturbation field.

The periodic assumption implicit in Fourier analysis often requires data to be detrended to remove any large scale gradients which cause strong discontinuities near the boundaries. For similar reasons data are often artificially tapered towards zero at the edges. However, the bi-periodic boundary conditions imposed on this model do not require such techniques to be employed and so the data are analysed in their ‘raw’ form here.

In order to quantify the perturbation *growth* at a certain spatial scale (or wavenumber, r) it is necessary to look at the evolution with time of the spectral density at that scale, $a_r(t)$. While the Fourier techniques used here show the spectral content down to the Nyquist wavelength (here 8km), it is important to note that information regarding scales approaching the grid scale should not necessarily be believed (Lander and Hoskins, 1997). For a model grid length of 4km, information on the spectral densities at scales between 8km and 20km should be viewed with an appreciation of the limitations of the techniques used to produce them.

The data examined here are from experiment MAIN (described in Chapter 3). In that experiment the ensemble mean evolutions of three perturbations ($\delta\theta_A$, $\delta\theta_B$ and $\delta\theta_C$) were considered. Therefore, when examining the growth of these perturbations as a function of spatial scale it is necessary to calculate the ensemble mean spectral densities, $\overline{a_r}$, as defined by,

$$\overline{a_r} = \frac{1}{3} (a_r^A + a_r^B + a_r^C).$$

where the superscripts denote the ensemble member from which the spectral densities were derived.

While other methods of spectral analysis such as wavelet analysis (e.g. Kaiser (1999)) can be used in place of Fourier techniques, the bi-periodic boundary conditions placed on the model in this thesis and the domain mean properties sought (as opposed to localised properties) make these results ideal for Fourier analysis.

5.2 Overview of the perturbation growth curves

Figure 5.1 shows the ensemble mean spectra of the potential temperature perturbation fields at 500m in experiment MAIN at 08:30 (solid) and 09:30 (dashed). It should be noted that in this thesis, spatial scales are referred to in terms of wavelength, λ , rather than wavenumbers, r , since wavelengths are not a function of the domain size and can therefore be interpreted more readily. It can be seen that the spectral densities have increased significantly at all spatial scales in the first hour of the forecast. This corresponds to the increased variance of the perturbation fields noted in section 3.3. The method of quantifying the perturbation growth at individual spatial scales (as

described in the previous section) finds the evolution of spectral density at a specific wavelength with time. The evolution of one such spectral density is highlighted in blue.

Figure 5.2 shows the evolution with time of the ensemble mean scalar spectral densities, $\overline{a_\lambda}(t)$, for six different wavelengths, λ . There are several points to note. Firstly, the perturbations grow at all spatial scales several minutes after the perturbations are inserted, associated with the boundary layer regime changes at the sensitive boundary layer locations. The grid point nature of the sensitive boundary layer locations causes an increase in spectral densities at all spatial scales since the power spectrum of a delta function (a spike) consists of equal spectral densities at all wavelengths.

The perturbation growth curve for the smallest spatial scale ($8\text{km}=2\Delta x$) exhibits evidence of diffusion in the model between 08:30 and 08:36 and between 08:40 and 09:20. This diffusion applied in the model is designed to damp variability at scales of $2\Delta x$, so it is not surprising that this dissipation is visible in this curve. Perturbation growth is observed at all scales after around 09:20 (marked by the dashed line in Figure 5.2) associated with convective instability. It can be seen that the growth is approximately linear until around 10:15 at the smallest spatial scales (see 8km and

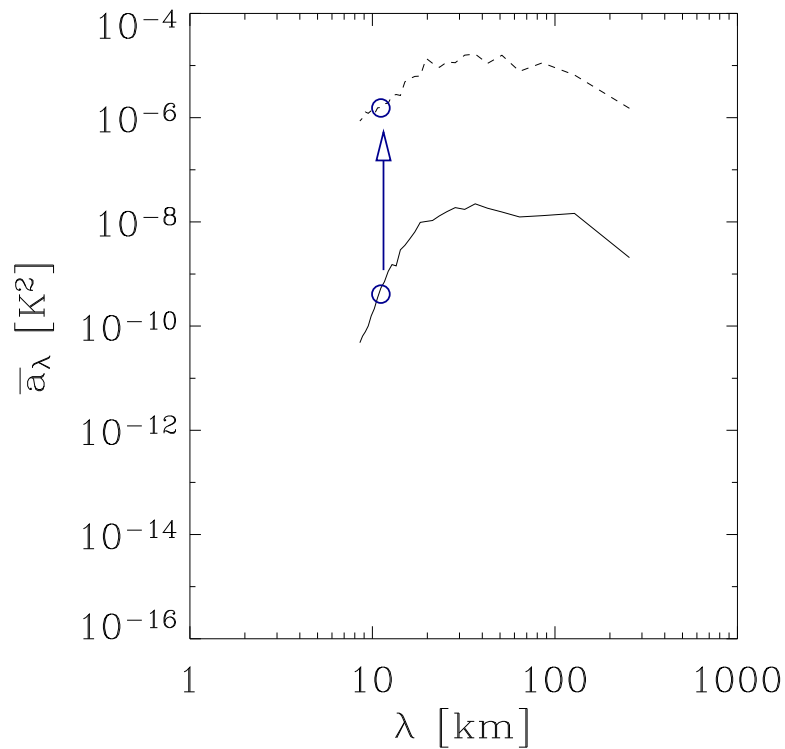


Figure 5.1: The ensemble mean power spectra of $\delta\theta_{500m}$ at 08:30 (solid) and 09:30 (dashed) in experiment MAIN. The evolution of individual spectral densities with time can be used to quantify the perturbation growth at individual spatial scales. An example of the change in spectral densities with time relating to the 10km scale is highlighted in blue.

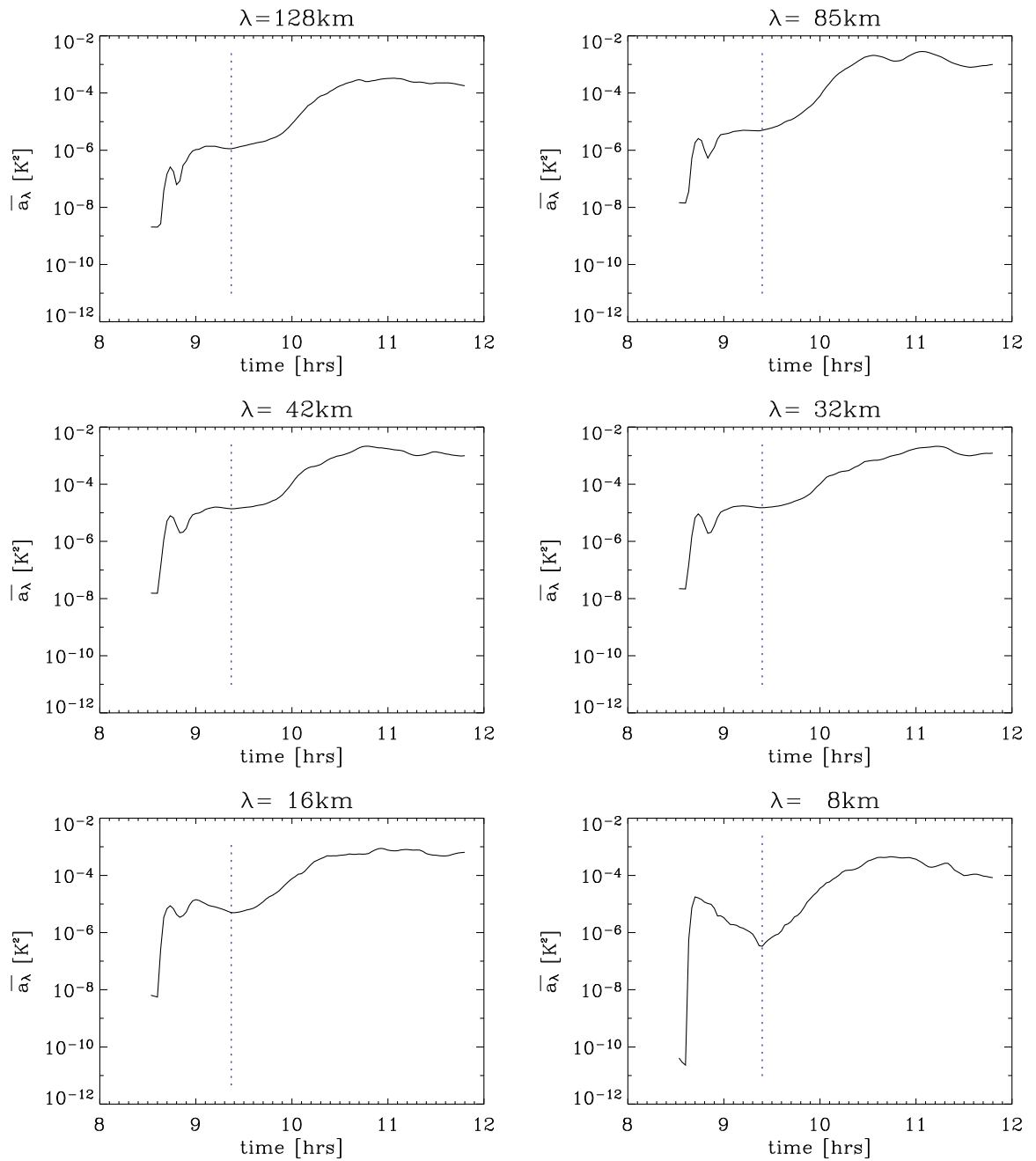


Figure 5.2: The evolution with time of the ensemble mean potential temperature perturbation scalar spectral density, $\overline{a_\lambda}(t)$, for different spatial scales in the boundary layer at 500m. Results shown for experiment MAIN. The time after which perturbation growth associated with convective instability becomes dominant is marked by the dashed line.

16km plots in Figure 5.2). Growth in the linear regime is exponential in nature and appears linear on the logarithmic y-axis in this figure. However, at spatial scales above 32km the perturbation growth at this time is *super-exponential*, i.e. the growth rate increases with time.

The initial growth rate of the perturbations during the second period of growth is measured in section 5.3. The super-exponential growth is investigated further in section 5.4 along with a hypothesis for its possible cause. The degree to which the perturbation growth can be described by linear dynamics is calculated in section 5.5. Finally, the saturation of the perturbations is investigated in detail in Chapter 6.

5.3 Quantification of the initial perturbation growth rate as a function of spatial scale

Information about the growth rate of perturbations during the initiation of deep convection is required for the design of a data assimilation system suitable for use at convective scales. In this section this initial perturbation growth rate is calculated as a function of horizontal spatial scale using the data from experiment MAIN.

The growth of perturbations associated with convective instability is seen to occur shortly after 09:20 in the simulation. Deep convection initiates shortly after this with the cloud tops rising above the boundary layer by 09:40. The initial growth rate is calculated using the difference between the spectral densities at times $t_1=09:38$ and $t_2=09:40$ at each spatial scale provided by the Fourier analysis. i.e.

$$\sigma_\lambda = \frac{a_\lambda(t_2) - a_\lambda(t_1)}{2a_\lambda(t_1)\Delta t} \quad (5.1)$$

where $\Delta t = t_2 - t_1$ and the factor of two on the bottom is inserted to account for the fact that the spectral densities come from the *power* spectrum and not the amplitude spectrum. It was decided to use this method to calculate σ rather than by fitting a curve to the data, since curve fitting makes an a priori assumption about the nature of the evolution of the perturbations. Results presented later in this Chapter (see Section 5.4) show that it is not entirely clear which curve should be used.

However, it must be acknowledged that the use of just two data points to calculate the growth rate of the perturbations will lead to the results being more susceptible to noise.

The results from these calculations are displayed in Figure 5.3a (diamonds). It can be seen that to a first order, the growth rate is faster at smaller spatial scales. The perturbation growth rate at scales of 10km is approximately 10^{-3}s^{-1} , which corresponds to a doubling time of 11.6 minutes. Similarly, at scales of 30km the perturbation growth rate is around 10^{-4}s^{-1} which corresponds to a doubling time of 116 minutes. Interestingly, at scales above 40km (approximately the size of the convective cells in this case study) the perturbation growth rate increases slightly to around $3 \times 10^{-4}\text{s}^{-1}$ at scales of 100km. This is discussed later in this section.

These perturbation growth rates can be compared with those expected from the linear theory of convection. Appendix B derives the growth rate of small perturbations to the basic state assuming that those perturbations are not large enough to significantly alter the basic state itself. The growth rate expected from linear theory, σ_{lin} , is found to be:

$$\sigma_{lin} = \sqrt{-\frac{N_m^2 \beta^2}{1 + \beta^2}}$$

where N_m^2 is the moist static stability parameter and β is the aspect ratio of the convective circulations ($\frac{dz}{dx}$). Therefore, tall, narrow cells grow faster than short, wide cells. This relationship is used to predict the growth rates of the perturbations in this case by making the assumption that the heights of the convective cells are all equal and taking the horizontal scale as the Fourier component being analysed. The heights of the convective cells at 09:40 are approximately 1km. Determining a representative value of N_m^2 is more problematic since there is a large variability with height. Figure 5.3b shows N^2 as calculated from the observed growth rate of the perturbations using the linear theory relationship described above. If linear theory did a good job of describing the observed perturbation growth at all scales then a single value of N^2 would be expected. However, it can be seen that this linear relationship occurs between around 10km and 40km.

Lines of σ_{lin} assuming values of N_m^2 of $-1 \times 10^{-5}\text{s}^{-2}$ and $-1 \times 10^{-4}\text{s}^{-2}$ are shown on Figure 5.3a for guidance. It can be seen that between 8km and 40km, the data follow the same general trend as the curves (i.e. growth rate increasing at smaller scales) albeit with noise present. Considerable

deviation occurs between the growth rates of the data and those expected from linear theory at scales below around 10km. However, at scales above 40km, the growth rate appears to increase as the scale increases.

The reasonable qualitative fit between the change in growth rate with scale between the data and linear theory at scales between 10km and 40km suggest that the *initial growth* of the perturbations can be approximated by making the linear assumption. The poorer fit between the data and linear theory above 40km can be explained by the fact that the convective cells do not grow any larger than 40km in this case study. The linear theory of convection can only be expected to make accurate predictions about the perturbation growth rate at scales over which convection is active.

A surprising result is the fact that the growth rate at the large scales is *greater* than that expected by convection. It seems unlikely that instabilities acting at larger scales such as barotropic or baroclinic instabilities are responsible for the growth at these scales. The growth rates resulting from baroclinic and barotropic instabilities should be *less* than those resulting from convective instability (see Chapter 1). A possible explanation for this unexpected result is that the initiation of regularly spaced convective cells at the time of this calculation is providing a source of energy at the scale of the mean inter-cell separation and is visible in the Fourier analysis (M. Ambaum 2005, personal communication). The peak in the growth rates observed above 40km scales could be indicative of the emergence of this characteristic storm spacing. Figure 2.12 shows that the number of storms (defined by updraughts above 3ms^{-1} at 980m height) in the domain increases rapidly from zero at 09:40 to a peak of over 50 at 10:40. In section 2.3 the mean separation of the storms at 10:40 was calculated to be around 30km. These observed inter-cell separation values seem compatible with the hypothesis above.

5.4 Super-exponential growth at large spatial scales

Figure 5.4 shows the growth rate plotted as a function of time for several spatial scales. For this figure, the growth rates were calculated over ten minutes (i.e. $\Delta t=10$ minutes in equation 5.1) to reduce the noise resulting from short-period variability. It can be seen that at scales where convection is active the growth rate remains relatively constant (e.g. at 8km (solid black line) and 20km (solid grey line)). However, at scales greater than those of the convective storms the growth

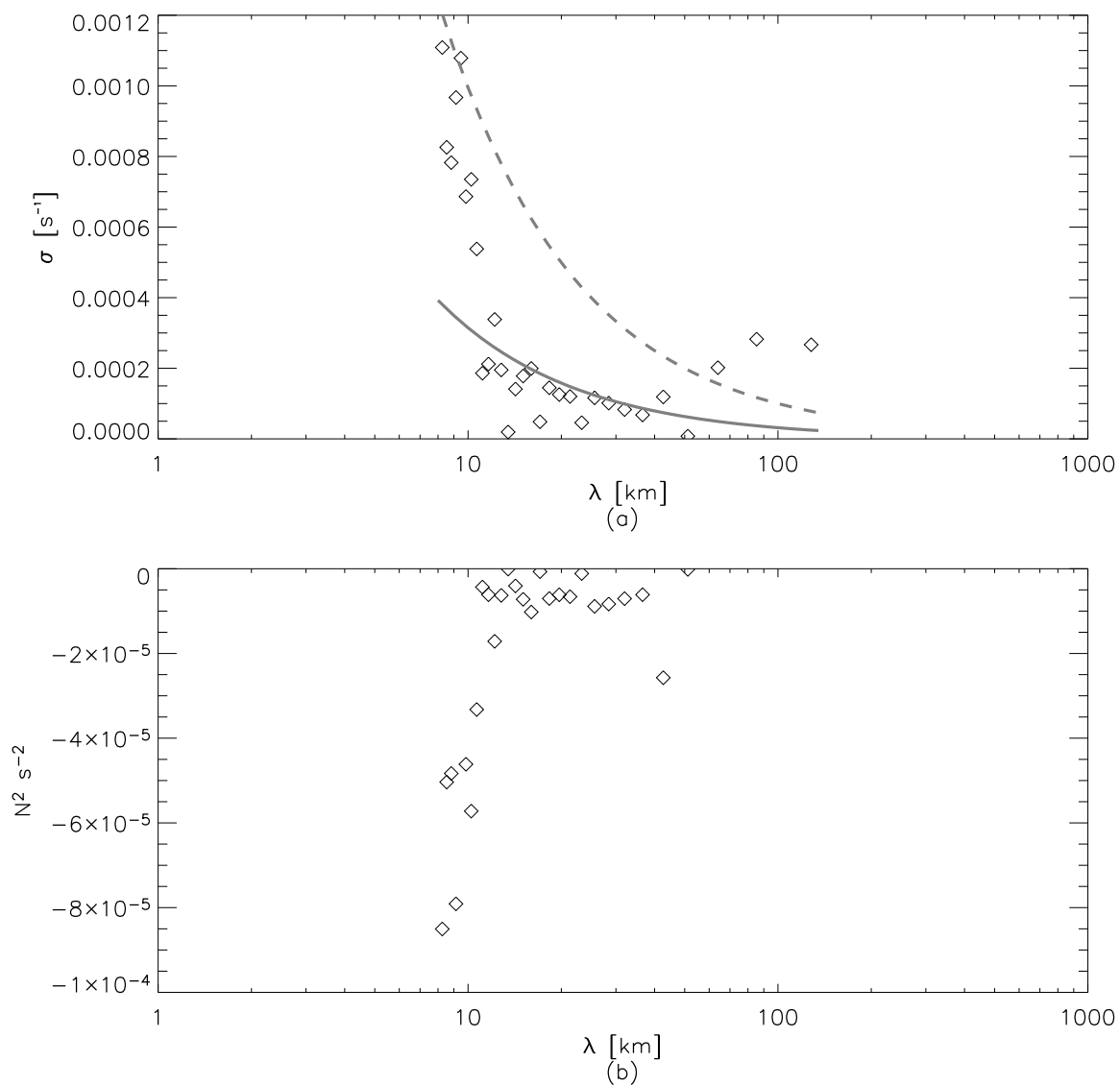


Figure 5.3: (a) The growth rate, σ , of the perturbations as a function of scale, λ , as measured from two data points in the early stages of convective growth. Lines show the growth rates expected from linear theory, σ_{lin} , assuming a constant height, dz , of 1km and $N^2 = -1 \times 10^{-5} \text{ s}^{-2}$ (solid) and $N^2 = -1 \times 10^{-4} \text{ s}^{-2}$ (dashed). (b) N^2 calculated from observed σ values using the linear theory relationship described above.

rate clearly increases with time.

In section 5.3 a hypothesis was presented to explain the relatively large initial growth rates observed at spatial scales above 40km. It was argued that the emergence of a characteristic separation of the convective circulations was manifested in the power spectrum and hence caused faster perturbation growth rates at those scales. Since the scales affected by this faster growth rate are the same scales that exhibit super-exponential growth it seems possible that the two features are related.

The emergence of a characteristic cell separation will result in an increase in the spectral density at the scale of the separation, i.e. perturbation growth at that scale will occur. However, this does not explain the increase in growth rate with time observed at these scales.

Super-exponential perturbation growth occurring at large spatial scales was also observed by Schubert and Suarez (1989) in a study of the domain mean error growth in a General Circulation Model associated with synoptic scale systems. In that paper it was noted that an empirical model of the error growth in which the large scale errors were dependent on the small scale errors, but where the small scale errors had no dependence on the large scale errors, gave an excellent fit to the observed error growth curves. This interaction of the large scales with the small scales was responsible for the super-exponential growth at large scales.

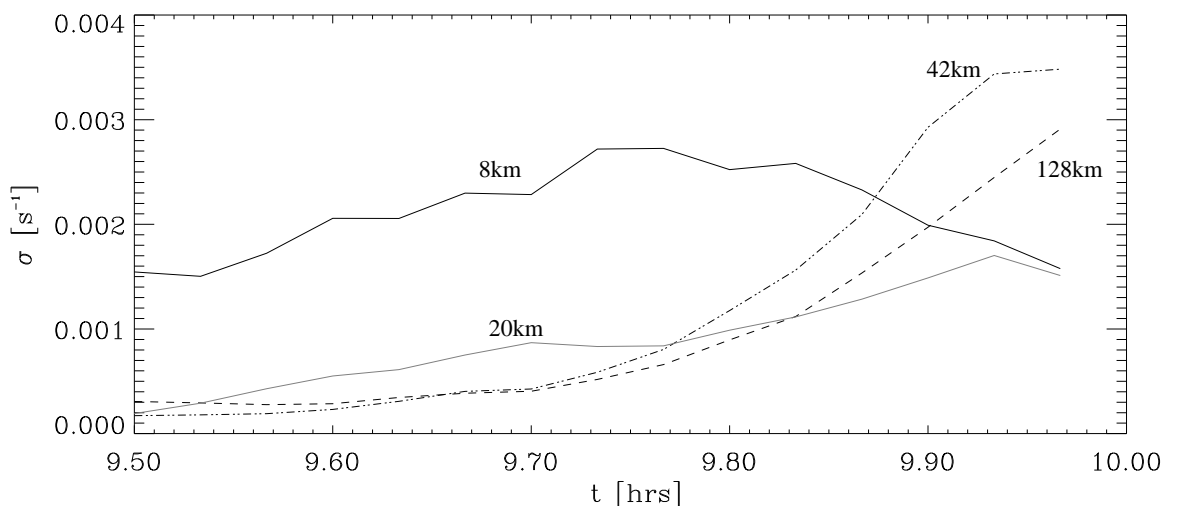


Figure 5.4: The growth rate, σ , of the perturbations as a function of time. Curves are shown for different horizontal spatial scales: 8km (solid black), 20km (solid grey), 42km (dotted), 128km (dashed). Growth rates are calculated over 10 minutes for each point to reduce the noise resulting from timestep to timestep variability. All results measured at 500m height in experiment MAIN.

Previous studies have found evidence of an upscale transfer of energy occurring from convective scales into the mesoscale. Vallis *et al.* (1997), in a large-eddy simulation study of the upscale transfer of energy from convective storms over the ocean, found that an inverse cascade of energy occurred since quasi-two-dimensional flows at scales larger than the convective forcing were induced by the potential vorticity anomalies associated with the storms. This was true both with and without the coriolis force present. However, no such large scale flows are observed in this case study.

In Figure 5.4, it can be seen that at any given time the growth rate at the 128km scale is less than that at 42km. This lag in the growth rates at increasingly large scales could be evidence of a possible upscale transfer of energy as energy takes longer to reach increasingly large spatial scales.

The existence of a possible upscale energy transfer mechanism in this case study needs to be considered further, but is outside the remit of the aims of this thesis. Since the aim of this chapter is to quantify the perturbation growth as a function of spatial scale, it is enough to identify that super-exponential growth at large scales occurs in this case study.

5.5 Quantification of the linearity of the perturbation evolution

It was shown earlier that the perturbation growth during convective initiation (occurring after perturbation growth due to boundary layer transitions) had a scale dependence that was similar to that expected by linear theory. This suggests that the perturbation growth at that time can be explained by linear dynamics. However, the subsequent super-exponential growth is evidently not linear. It is useful to quantify the linearity of the growth with time.

Gilmour *et al.* (2001) defined a measure of how well the evolution of a perturbation can be approximated by linearised dynamics, named the *relative non-linearity*, Θ . This used the fact that in the linear regime, perturbations that are initially equal and opposite will evolve equally and oppositely (see Figure 5.5). Any asymmetry in the evolution of these two perturbations is indicative of non-linear dynamics. The *relative non-linearity* is defined as,

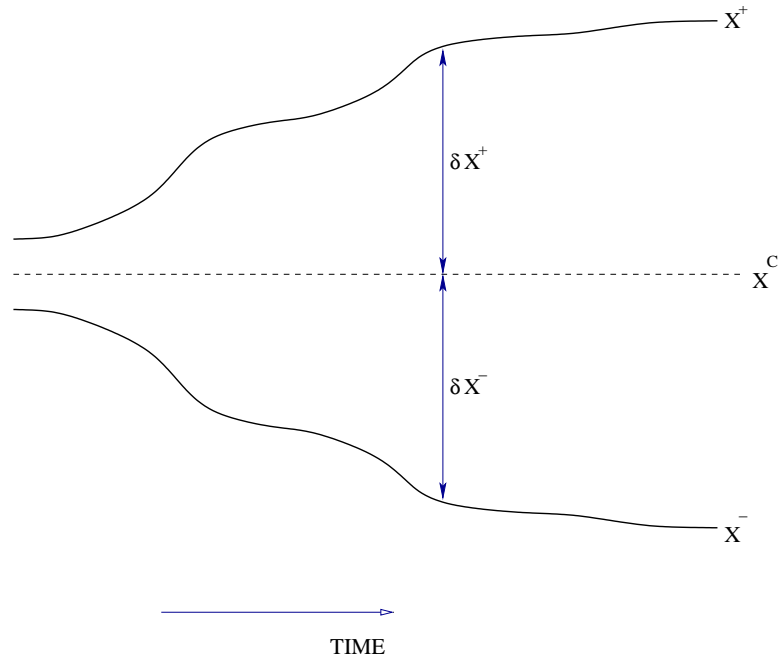


Figure 5.5: Schematic to illustrate the evolution of a positively perturbed forecast, x^+ , and a negatively perturbed forecast, x^- , with respect to an unperturbed control forecast, x^c , in the linear regime. The evolution of the two perturbations, δx^+ and δx^- , is equal and opposite.

$$\Theta(t) = \frac{\|\delta\theta^+(t) + \delta\theta^-(t)\|}{\frac{1}{2}(\|\delta\theta^+(t)\| + \|\delta\theta^-(t)\|)}.$$

where $\delta\theta^+(t) = \theta^+(t) - \theta^c(t)$ and $\delta\theta^-(t) = \theta^-(t) - \theta^c(t)$. θ^+ and θ^- represent the potential temperatures in the forecasts made from the positively perturbed and negatively perturbed initial conditions respectively. θ^c represents the potential temperature in the control (unperturbed) forecast. $\|\cdot\|$ notation represents a norm (in this case the variance of the field). If the perturbations are equal and opposite then the terms in the numerator of the equation cancel, giving a relative non-linearity of zero, i.e. linear growth. The relative non-linearity is necessarily calculated from a single ensemble member (member A) rather than using an ensemble mean.

Figure 5.6 shows $\Theta(t)$ for the perturbations in experiment MAIN as viewed at 500m height. Initially, Θ is close to zero indicating that θ^+ and θ^- are evolving almost equally and oppositely. The fact that $\Theta(08 : 30)$ is not exactly equal to zero results from round-off error in the calculations. However, four minutes after the insertion of the perturbations Θ increases suddenly to two. This shows that the perturbation growth at the sensitive boundary layer locations is highly non-linear. The fact that $\Theta=2$ indicates that only one of the perturbations has grown, i.e. either the positively perturbed run or the negatively perturbed run evolves differently from the control run,

but not both. An examination of the individual perturbation fields confirms this (not shown). This is to be expected since if a boundary layer profile is close to a threshold between ‘types’ in the parameterisation scheme, then only a perturbation that pushes the profile over the threshold will change the type. When considering a positive negative pair, one perturbation will push it closer to (or over) the threshold while the other will take it further away from the threshold. Therefore, the evolutions of the two perturbations will not be symmetric.

It is possible for linear regime growth during convective initiation to take place after non-linear growth during boundary layer regime change. However, this measure of linearity requires that the perturbations are equal and opposite at the time of convective initiation to be able to identify this. Therefore, any subsequent evolution in the linear regime resulting from convective instability cannot be identified in this plot since they take place after the highly non-linear growth at sensitive boundary layer locations.

In an attempt to quantify the linearity of the perturbation growth associated with convective instability, results from experiment TARGET (see Chapter 4) are examined. In this experiment, potential temperature perturbations of 0.002K amplitude were inserted at 4500m height at 09:50. The timing and location of these perturbations were specified such that a growing convective plume

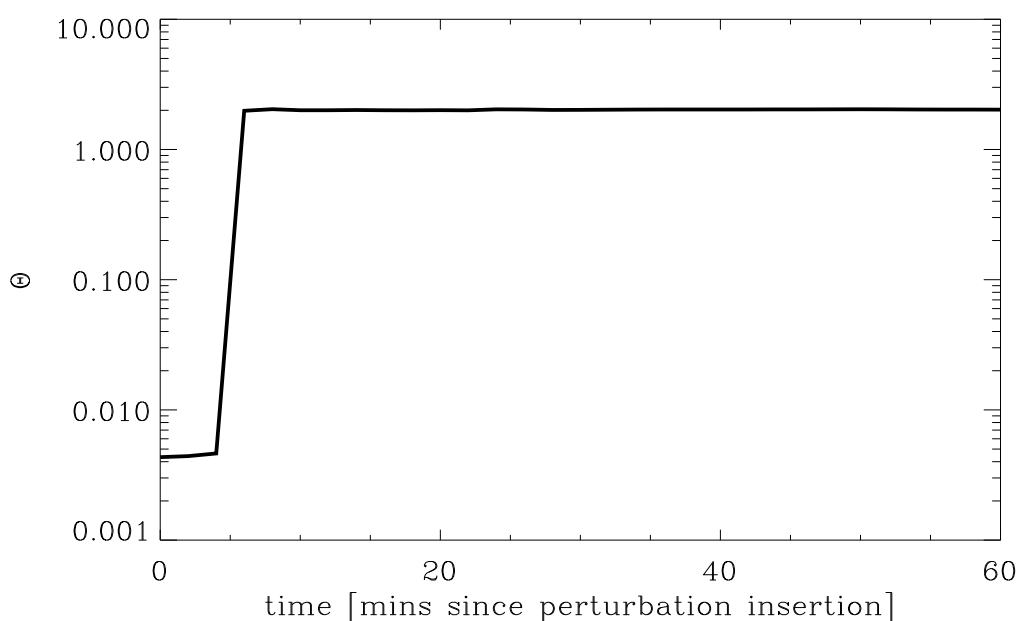


Figure 5.6: The relative non-linearity of the perturbations at 500m height in experiment MAIN. i.e. perturbations inserted at 08:30 at 500m height.

rose through the perturbations within minutes of insertion. In addition, the height of the insertion required more time for vertical propagation of the perturbations before perturbation growth at sensitive boundary layer locations could take place. Therefore, in this experiment perturbation growth associated with convective instability took place before any growth by boundary layer regime changes. The results from this experiment allow the linearity of the perturbation growth associated with convective instability to be quantified.

Figure 5.7 shows the relative non-linearity of the perturbations at 4500m height in experiment TARGET. It can be seen that the initial growth is approximately linear, but that it becomes increasingly non-linear with time. Θ remains below 0.1 for over 15 minutes. However, after 20 minutes Θ has reached a value of around 2. Therefore, these results indicate that the linear regime in this case lasts for only a matter of minutes.

It must be noted that there are several explanations for this rapid transition to non-linearity. Firstly, it is possible that the perturbation growth within these convective storms is inherently non-linear. Secondly, it could be because the convective plume reaches the tropopause around 20 minutes after the perturbations are inserted. Initially linear growth occurring before the storm reaches the tropopause might be expected to become non-linear as the storm ceases to grow vertically.

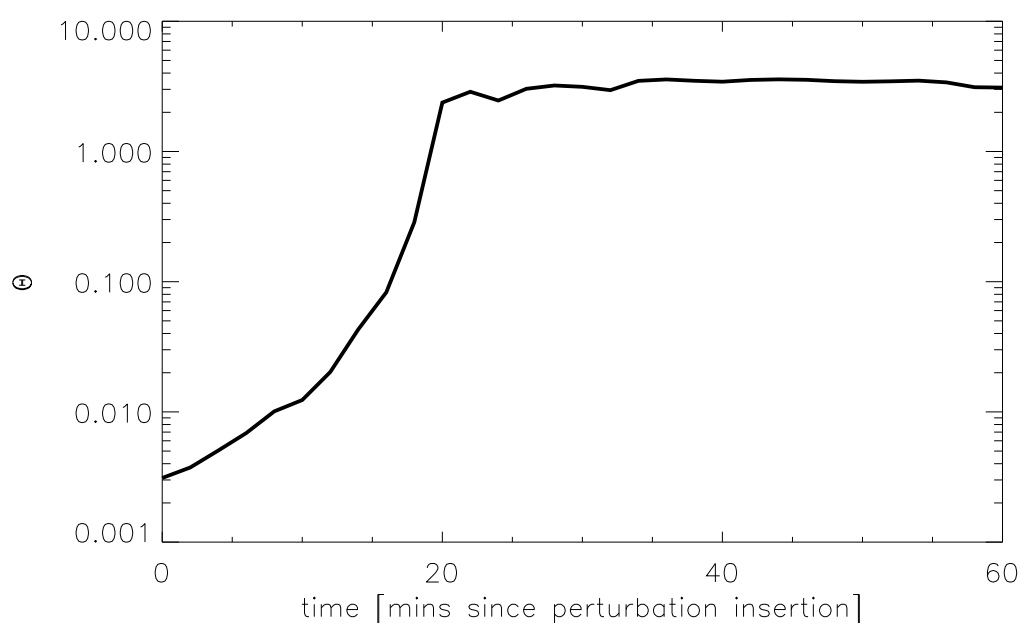


Figure 5.7: The relative non-linearity of the perturbations added at 09:50 in experiment TARGET at 4500m (height of insertion).

Finally, it is possible that the growth within the storm is linear and that vertical propagation of the perturbations into the boundary layer has seeded non-linear perturbation growth at the sensitive boundary layer locations and that these effects have reached the height examined here within 20 minutes. Since the convective storms reach the tropopause at the same time that non-linear growth in the boundary layer occurs it is not possible to identify which if any of these causes is responsible for the non-linear growth observed after 20 minutes.

Using this technique it is difficult to isolate the linearity of each perturbation growth mechanism. However, it can be concluded that in this case study, in this model, the overall perturbation growth is highly non-linear with a linear regime lasting for only a few minutes. The linear regime lasts slightly longer if the perturbations are inserted above the boundary layer.

The rapid transition to the non-linear regime indicated in these results has implications for convective scale data assimilation and the design of optimal perturbations for convective scale ensemble forecasts. These implications will be discussed in Chapter 7.

5.6 Chapter Summary

- The growth of potential temperature perturbations was quantified as a function of horizontal spatial scale and time using Fourier analysis.
- The two periods of perturbation growth identified in Chapter 3 could be identified at all spatial scales.
- **The growth rate of the perturbations during the initiation of deep convection was found to increase as the spatial scale decreased.** Perturbation doubling times ranged from around **12 minutes at 10km scales** to almost **two hours at 30km scales**.
- The linear theory of convection was found to provide a reasonable description of the scale dependence of the perturbation growth rate at scales at which convection was observed to be active (below 40km).
- The emergence of a characteristic storm separation is thought likely to be responsible for perturbation growth rates slightly higher than expected by the linear theory of convection at scales above 40km.

- **Super-exponential growth was observed at scales larger than those of the convective forcing.**
- The linearity of the dynamics was quantified using the relative non-linearity defined by Gilmour *et al.* (2001).
- **Perturbation growth resulting from boundary layer transitions were found to be highly non-linear in nature.** An attempt to isolate the convective growth using results from experiment TARGET revealed a transition from almost linear to non-linear growth within 20 minutes. However, non-linear effects from the boundary layer may still have interfered with these results.

CHAPTER SIX

Quantification of the error saturation timescale

The final thesis aim of quantifying the error saturation timescale (i.e. the timescale over which forecasts lose all skill) at convective scales is addressed in this chapter. Information of this kind is useful for identifying the likely useful range of high resolution numerical weather forecasts of convective features in situations similar to a cold air outbreak.

Lorenz (1982) identified two limits to the range of predictability. The *upper limit* is defined as the time taken for very small amplitude initial errors to saturate, i.e. the maximum lead time over which a forecast can ever be skillful even if the amplitude of the initial errors is reduced to almost zero. The *lower limit* is determined by the amplitude of current errors in the analysis, i.e. the timescale over which forecasts are skillful today. An experiment is described in this chapter which serves to identify both the upper and lower limits of the range of predictability at convective scales. The error saturation timescale is quantified as a function of horizontal spatial scale using the Fourier techniques adopted in the previous chapter.

6.1 Definition of error saturation

In order to quantify an error saturation timescale, it is first necessary to provide a precise definition of *error saturation*. Forecast errors saturate (i.e. their growth rate reduces to zero) when the forecast becomes as different from reality as that of a random ‘guess’ of the atmospheric state based on the climatology of the system. At error saturation, the correlation between the forecast and the true atmospheric state is zero. This is the basis of the definition of error saturation used in this chapter.

Unfortunately, in the absence of adequate convective scale analyses a comparison of a convective scale forecast with reality is not possible. Instead, in this thesis two forecasts started from slightly different initial conditions are compared with each other (i.e. the ‘dynamical’ method described in Chapter 1). Consequently, in this chapter **error saturation is defined as having occurred when the correlation between the two forecasts is zero**. The times taken for the two forecasts to become uncorrelated is likely to be greater than that over which a forecast becomes uncorrelated from the true atmospheric state, since errors associated with scales unresolved by the forecast model quickly spread upscale and increase errors in forecasts of the resolved scales (Lorenz, 1969a). Therefore, it must be recognised from the outset that the definition of error saturation used here may result in an *overestimation* of the timescale over which a forecast actually loses skill.

It can be shown that the variance of the perturbation field (i.e. the difference between two forecasts with states x^+ and x^-) is related to the correlation between the two forecasts using the following identity:

$$\text{var}(x^+ - x^-) = \text{var}(x^+) + \text{var}(x^-) - 2\text{cov}(x^+, x^-)$$

where the covariance (*cov*) is related to the correlation (*cor*) by,

$$\text{cor}(x^+, x^-) = \frac{\text{cov}(x^+, x^-)}{\sqrt{\text{var}(x^+)}\sqrt{\text{var}(x^-)}}.$$

At error saturation the correlation of the two forecasts is zero, i.e. $\text{cov}(x^+, x^-) = 0$. Therefore,

assuming $\text{var}(x^+) \approx \text{var}(x^-)$,

$$\text{var}(\delta x) \approx 2\text{var}(x^+). \quad (6.1)$$

i.e. the variance of the perturbation field becomes equal to twice that in a single forecast when the errors are saturated. This allows error saturation to be diagnosed as a function of spatial scale since the spectral density at a given scale is related to the variance at that scale (see section 6.3.2). The assumption that the variance in each of the two forecasts is the same is valid since both forecasts use the same basic state and differ only by the insertion of equal but opposite perturbations (with a mean of zero). There is no reason to believe that the domain average behaviour of the two forecasts should be significantly different.

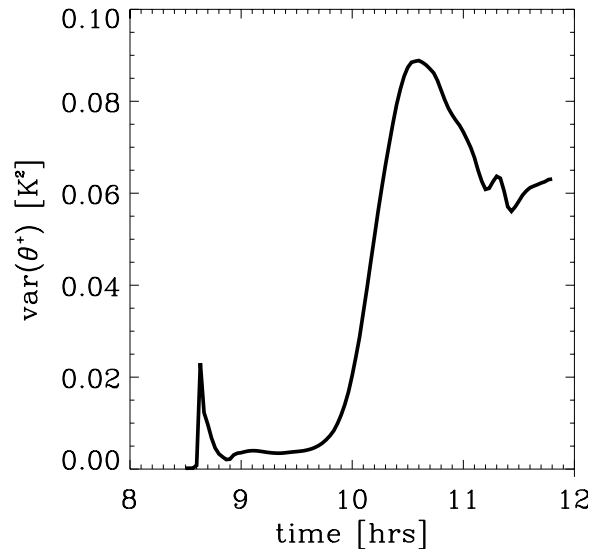


Figure 6.1: The time evolution of the variance of the potential temperature, θ , in a positively perturbed forecast at 500m height. Results are taken from the original experiment (MAIN) where perturbations of initial amplitude 0.002K were inserted at 500m height.

Figure 6.1 shows the variance of the potential temperature in a positively perturbed forecast ($\text{var}(\theta^+)$) in the boundary layer at 500m height. It can be seen that the variance changes significantly during convective initiation (seen here at approximately 09:30). Therefore, the saturation level of the perturbations also changes with time.

6.2 Definition of the initial amplitude of the perturbations

In order to find the upper and lower bounds of the error saturation timescale it is necessary to use perturbations of two amplitudes; the largest should be approximately equal to the current analysis errors in potential temperature, and the smallest should represent the maximum possible accuracy that could ever be achieved in the analysis at convective scales. This section provides estimates of these two amplitudes.

6.2.1 Current analysis errors in potential temperature at convective scales

Meteorological analyses are generated through a data assimilation cycle where observations are combined with a short-range forecast to provide values of each prognostic model variable at every grid point. As always, the estimation of analysis errors is problematic because the analysis is the best available estimate of the state of the atmosphere at a given time, i.e. knowledge of the true state of the atmosphere, with which a comparison is desired, is unavailable. However, the accuracy of an analysis is strongly dependent on the accuracy of the observations used to generate it. This section discusses the accuracy of such observations.

A number of instruments are capable of measuring the temperature of the atmosphere. Screen thermometers measure the temperature just above the surface, LIght Detection and Ranging (LIDAR), SOund Detection And Ranging (SODAR) and microwave and infra-red sounders can also sense the temperature remotely. Table 6.1 displays the accuracy of various instruments at measuring the temperature, as quoted from the given sources. A traditional mercury thermometer has an accuracy of $\pm 0.2\text{K}$. However, the inability of standard specification screens to provide sufficient ventilation and shielding from radiation can result in errors of up to 2.5K (WMO, 1983). Satellite-borne sounders have an accuracy of no better than 1.0K .

In addition, observations of convective boundary layers have shown that the potential temperature can have a high degree of variability from the mesoscale ($\sim 100\text{km}$) down to the scale of viscous dissipation ($\sim 1\text{mm}$) (De Roode and Duynkerke, 2004). Weckworth *et al.* (1999) and Weckworth (2000) demonstrated that boundary layer virtual potential temperature variations of over 0.5K can occur over scales of only 500m associated with convective rolls. This small-scale variability combined with the sparse sampling provided by the current observing network leads to considerable

Instrument	Accuracy [K]	Source
Screen thermometer	0.2 - 2.5	WMO (1983)
Radiosonde	0.2 - 0.5	Luers (1997), Hooper (1986)
ATOVS/HIRS/AMSU (satellite)	1.0 - 3.2	Li <i>et al.</i> (2000), Huang <i>et al.</i> (1992), Shi (2001)
GOES (satellite)	1.0 - 2.0	Menzel <i>et al.</i> (1998)
Lidar	1.0	Korb and Weng (1982)
Microwave radiometer	1.0	Browning (2005)
Sodar	0.3	Bradley and Hipkin (2002)

Table 6.1: Accuracy of various instruments capable of measuring boundary layer temperature.

sampling error in the observations. Surface observations in the United Kingdom are typically separated by tens of kilometres and report, at best, every 30 minutes. Furthermore, the current United Kingdom radiosonde network provides vertical profiles of temperature at only 10 locations every 12 hours. While almost global coverage is provided by satellite-borne sounders (such as ATOVS, HIRS, AMSU and GOES) the vertical and horizontal resolution of these instruments is still inadequate to resolve convective scale features.

Therefore, at convective scales the relatively sparse spatial and temporal resolution of the current observation network mean that even with accurate instrumentation, the observational errors are likely to have a similar amplitude to the variability of the thermodynamic fields. Given these observational errors, it is unlikely that the analyses at convective scales will have a significantly higher accuracy. It seems probable that the analysis errors in potential temperature are on the order of 1K. This is used as the amplitude of the largest perturbations inserted in this experiment, and will be used to provide the lower limit to the error saturation timescale.

6.2.2 Lower limit of analysis errors in θ at convective scales

The perturbations used in the original experiment (MAIN) had an amplitude of only 0.002K in order to extend the linear regime of error growth. It seems highly improbable that analysis errors in potential temperature at convective scales will ever be reduced to 0.002K given that at present, operational observing instruments do not an accuracy within two orders of magnitude of that value and given the spatial and temporal variability of the temperature at convective scales (see previous section). Therefore, this amplitude is chosen to represent the minimum analysis errors that will

ever be achieved; the time taken for these perturbations to saturate will indicate the maximum time over which accurate convective scale forecasts in these situations will ever be possible.

6.3 Methodology of experiment ‘AMP’

The timescale over which perturbations of different initial amplitude reach saturation is measured in this experiment. This experiment will be referred to as experiment ‘AMP’ herein. Perturbations of four different amplitudes are considered. Perturbation fields with the same shape, but different amplitude are constructed by convolving Gaussian kernels of different amplitude with the same random number field. As in the original experiment (MAIN), a ‘Lean’ ensemble of three uncorrelated positive/negative perturbation pairs is used to make the results less prone to sampling error, i.e. a total of 12 positive/negative pairs of perturbations are considered; 4 ensembles (constructed from the same random number fields but using Gaussian kernels of different amplitudes), each consisting of 3 ensemble members (using uncorrelated random perturbation fields of the same amplitude). A schematic is presented in Figure 6.2 to clarify the setup of this experiment.

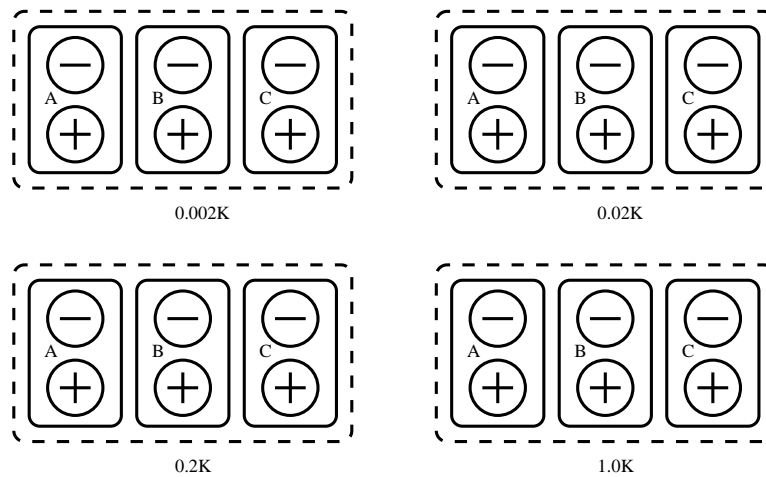


Figure 6.2: A schematic to illustrate the individual forecasts used in experiment AMP. ‘+’ indicate forecasts where the potential temperature perturbation is added, ‘-’ indicates those forecasts where the same perturbations are subtracted. The difference between these two forecasts is then measured. Four ensembles (shown by the dashed lines) consisting of three pairs (A, B and C) of forecasts (solid lines) are used. The perturbations within each ensemble are uncorrelated. The only difference between each ensemble is the initial amplitude of the perturbation (indicated in the figure).

6.3.1 Constructing perturbations of different amplitude

As in experiment MAIN, the perturbations are constructed by convolving a Gaussian kernel with a random number field. Different amplitude perturbation fields are generated by varying the amplitude of the Gaussian kernels. Table 6.2 shows the amplitude of the Gaussian kernels used along with the ensemble mean peak amplitude of the resulting perturbation fields in this experiment. The two intermediate amplitude ensembles of perturbations are set with initial amplitudes of approximately 0.2K and 0.02K in order to provide information on the likely improvement in the timescale of skillful forecasts brought about by a decrease in analysis errors.

The same three random number fields R_A , R_B and R_C are used to generate the perturbations in each ensemble. Therefore, the only difference between each ensemble is the amplitude of the perturbations.

6.3.2 Measuring error saturation as a function of horizontal spatial scale

As in the previous chapter, the spectral content of the perturbations is calculated using Fourier techniques. As mentioned earlier, this allows the error growth and its subsequent saturation to be measured as a function of spatial scale. The definition of error saturation provided by equation 6.1 is in terms of the variance of the perturbation with respect to the variance in an individual forecast. The spectral density at a given scale (found by Fourier analysis) is directly proportional to the variance at that scale. Therefore, this definition can be adapted to allow error saturation to be defined at a given spatial scale in terms of the perturbation spectral density, $a_{\delta\theta}(\lambda)$, with respect to the spectral density in an individual forecast, $a_{\theta}(\lambda)$, as follows:

Kernel amplitude	Mean peak amplitude of $\delta\theta$ [K] (2 sig.fig)
0.001	0.0021
0.01	0.021
0.1	0.21
0.5	1.0

Table 6.2: The ensemble mean peak amplitude of the perturbations, $\delta\theta$, in each ensemble constructed from Gaussian kernels of different amplitude.

$$a_\lambda(\delta\theta) \approx 2a_\lambda(\theta^+),$$

where λ is the wavelength.

Furthermore, the ratio, γ , of the spectral density of the perturbation to the spectral density of the full θ field can be defined as,

$$\gamma(\lambda) = \frac{\bar{a}_\lambda(\delta\theta)}{\bar{a}_\lambda(\theta^+)} \quad (6.2)$$

where overbars represent ensemble means. When $\gamma=2$, at a horizontal scale, λ , errors can be said to have saturated at that scale.

6.4 Results

6.4.1 Spatial and initial perturbation dependence of error saturation

Figure 6.3 shows γ as a function of time for different values of λ . Each plot shows the ensemble mean evolution of the different ensembles (each starting from a different initial amplitude) for a particular spatial scale, λ , (indicated at the top of each plot). The line $\gamma = 2$ is also shown (dashed) in each plot to indicate when the condition of error saturation has been met.

It can be seen that a large discontinuity in the values of γ occurs around 10 minutes after perturbation insertion, associated with the error growth at sensitive boundary later locations which occurred at that time. Interestingly, the ratio, γ , decreases at this time as the perturbation variance becomes smaller relative to the total field variance. After this, all of the curves tend towards saturation (with some noise present).

At scales of 8km (lower-right plot) perturbations with an initial amplitude of 0.002K take longer to reach saturation than those with a larger initial amplitude (e.g. 1.0K). It can be seen that this is also true at other spatial scales. Similarly, comparing the 0.002K perturbations (orange curves) at scales of 128km (upper left) and 8km (lower right) reveals that while after three hours the perturbations are almost saturated ($\gamma \approx 2$) at 8km scales, they are still far from saturated at 128km.

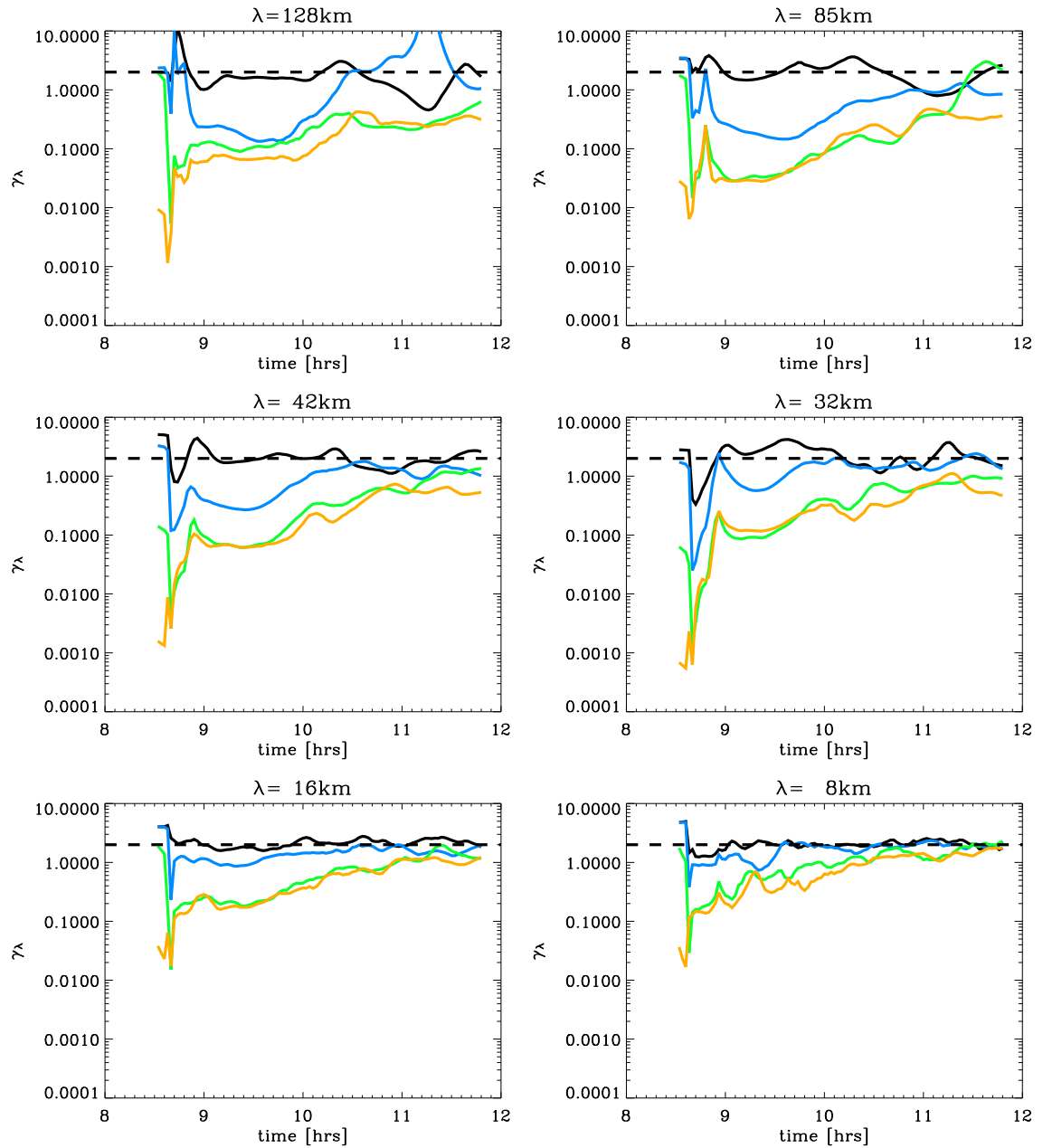


Figure 6.3: The evolution of $\gamma_\lambda = \frac{a_\lambda(\delta\theta)}{a_\lambda(\theta^+)}$ with time for perturbations of different initial amplitude at different spatial scales (indicated at the top of each plot). γ for perturbations of initial amplitude of 1.0K (black), 0.2K (blue), 0.02K (green) and 0.002K (orange) are shown. The line $\gamma = 2$ is also shown (dashed) which represents the level of error saturation.

From this brief examination of the results it is possible to conclude that smaller spatial scales saturate more rapidly than larger scales, and that perturbations with a smaller initial amplitude take longer to reach saturation than those with a large initial amplitude.

Another point of interest is that some of the curves have an initial value of γ greater than two, i.e. the variance of the perturbations added to or subtracted from the basic state is greater than that in the model prior to the insertion of those perturbations. In such cases, the value of γ quickly decreases indicating that that variance in the thermodynamic fields cannot be supported by the model atmosphere at that time.

Noise appears to be present in all of the curves. In particular the curves for larger spatial scales (e.g. 128km plot in upper-left) have larger amplitude fluctuations than those at small spatial scales. This could result from sampling error in the fourier analysis. The domain size of 256km can only support two waves of wavelength 128km, but 32 waves of wavelength 8km. This makes the larger scales more prone to sampling error leading to a variability in the spectral density with time at those scales.

The noise present in the γ curves mean that it is not appropriate to find the error saturation timescale by simply measuring the time taken for γ to reach a value of two. Such a technique would be highly sensitive to any noise present in the results. The use of time integrals which are dependent on the whole curve rather than on just an individual point along it are less sensitive to noise and therefore more suitable for quantifying the error saturation in these results. The following sections describe two new metrics (based on time integrals) that are applied to these results; the first is a measure of the overall skill in the first 200 minutes of the forecast, the second is a measure of the error saturation timescale.

6.4.2 Quantifying the skill of the forecast

Prior to error saturation, a forecast contains some degree of skill. In Figure 6.3, a forecast has skill if an area exists between the error growth curve and the line $\gamma = 2$. Therefore, the area between the perturbation growth curve and the line $\gamma = 2$ over a finite time can be used as a measure of the overall skill of the forecast during that time. This measure can be called the *characteristic skill*, S , of the forecast,

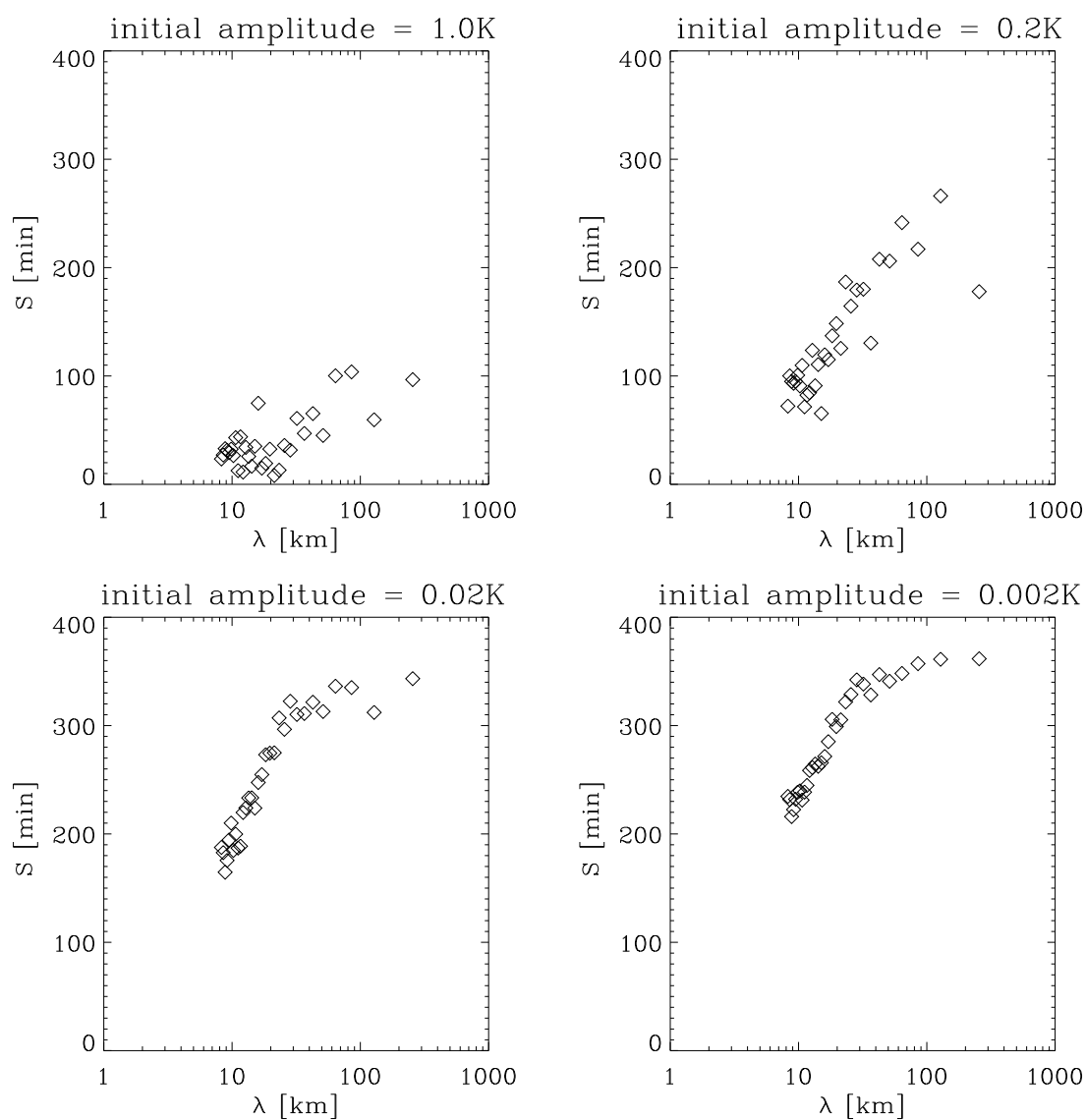


Figure 6.4: The characteristic skill, S , of the first 200 minutes of the forecast as a function of spatial scale. Plots show ensemble mean S for ensembles of perturbations of different initial amplitude. The initial amplitude of the perturbations is indicated at the top of each plot.

$$S = \int_{t_1}^{t_2} (2 - \gamma) dt \quad (6.3)$$

where t_1 is taken to be 08:30 and t_2 taken as 200 minutes later in the following calculations. It must be remembered that the use of the word ‘skill’ in this case is only appropriate within a perfect model framework, since these forecasts are only compared with each other and never with reality.

Figure 6.4 shows S as a function of spatial scale for perturbations of different initial amplitude. In each plot, forecasts of features with smaller spatial scales have less skill than those at larger spatial scales (indicated by lower values of S with decreasing λ). Also, it can be seen that the values of S are smaller when the initial perturbation amplitude is larger. For example, the largest perturbations inserted (with an amplitude of 1.0K; approximately equal to the current analysis errors) result in forecasts with little or no skill at all spatial scales.

6.4.3 Quantifying the error saturation timescale

A measure of the timescale over which errors approach saturation can be calculated with the use of a new metric τ . This is defined as the characteristic skill, S , weighted by time, and normalised by S , i.e.

$$\tau = \frac{\int_{t_1}^{t_2} t (2 - \gamma) dt}{\int_{t_1}^{t_2} (2 - \gamma) dt}. \quad (6.4)$$

It can be seen that τ has units of time, and more weight is given to skill at long lead times. Appendix D provides further guidance on the interpretation of τ using some simple test curves for γ . Values of τ less than $\frac{t_2 - t_1}{2}$ (in this case 100 minutes) mean that γ is tending towards saturation. In this range τ is related to the time taken for γ to reach saturation, i.e. the range of predictability (described in Chapter 1). If τ equals $\frac{t_2 - t_1}{2}$ then γ is not tending towards saturation. γ is tending away from saturation if τ has a value greater than $\frac{t_2 - t_1}{2}$.

Figure 6.5 shows τ as a function of horizontal spatial scale for perturbations of different initial amplitude. The values of τ in all cases are less than 100 minutes confirming that all perturbations are indeed tending towards saturation. It is also clear that the error saturation timescale is longer

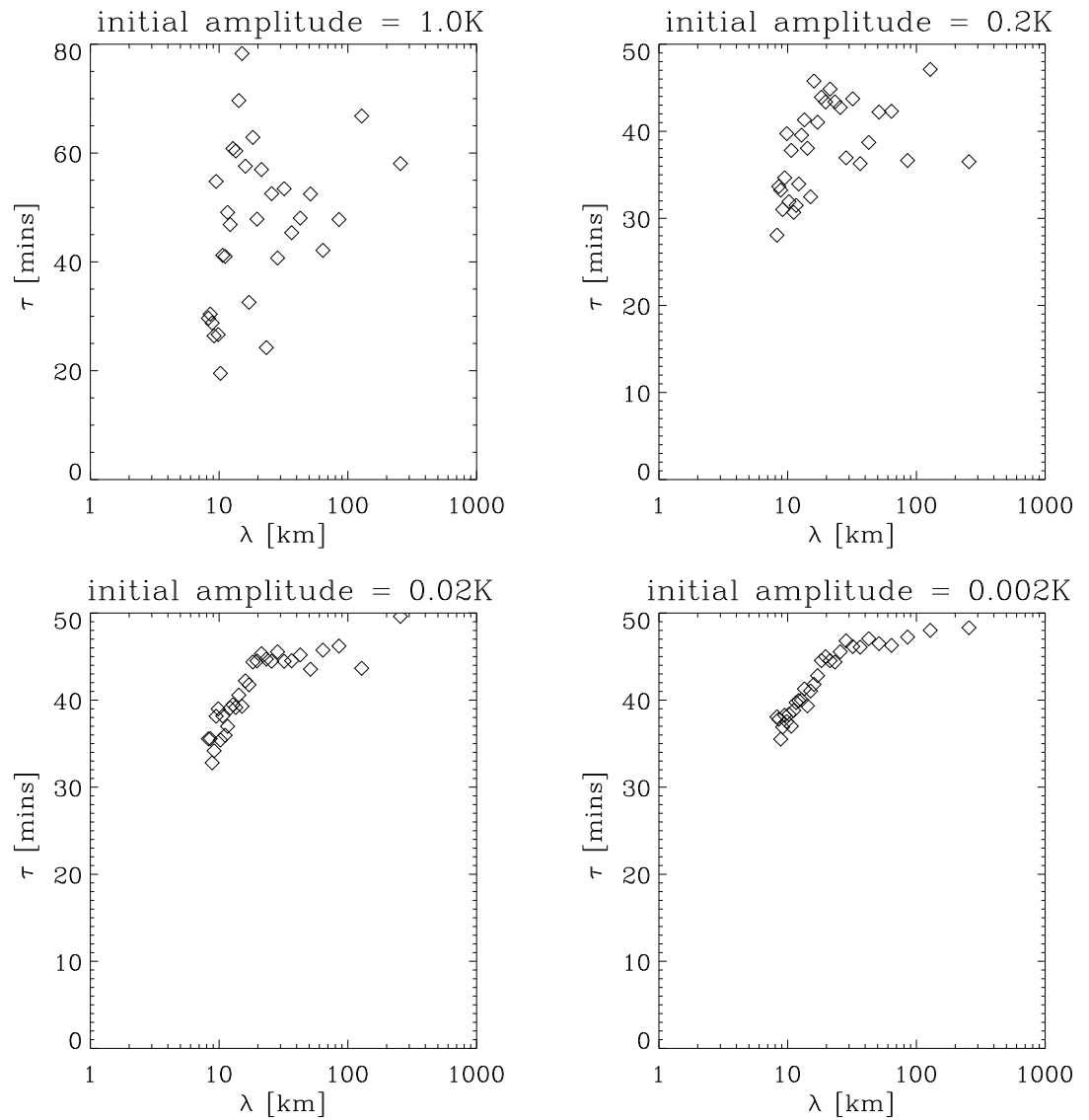


Figure 6.5: τ calculated over the first 200 minutes of the forecast as a function of spatial scale. Plots show ensemble mean τ for ensembles of perturbations of different initial amplitude. The initial amplitude of the perturbations is indicated at the top of each plot.

for forecasts of features at larger spatial scales (indicated by the increase in τ with λ in all of the plots).

The values of τ should not be interpreted as the time taken for the errors to reach saturation (i.e. the range of predictability), but simply as being proportional to it. However, the range of predictability can be estimated using these results. A curve tending towards a saturated value will never reach that value. The range of predictability can be defined as the time taken for the correlation between the forecasts to drop below some arbitrary level. In this case, if the errors with an initial amplitude of 0.002K are assumed to reach this arbitrary value after 200 minutes at scales of 8km (taken from Figure 6.3) then a simple scaling of the error saturation timescales can be used to calculate the range of predictability for those errors at larger spatial scales. This technique leads to a range of predictability of around 260 minutes for spatial scales of 20km, and 275 minutes for scales of 100km, for errors with an initial amplitude of 0.002K. These are the upper limits of the range of predictability.

The change in the slope of τ with λ at about 20km coincides with the approximate spatial scale of the convective cells. This could indicate that the predictability timescale of spatial scales larger than the convective scales are determined by the maximum size of the convective storms, i.e. the convective storms provide a mechanism to transfer error energy from the small scales to large scales and influence the predictability of those scales. However, further work would be required to confirm this.

It would be expected that the error saturation timescale would be shorter for errors with a larger initial amplitude as they set off closer to saturation, i.e. forecasts initiated from analyses with larger errors will be skillful for less time. However, the increased spread of the values of τ with increasing initial perturbation amplitude (e.g. see the large variability in the 1.0K results compared with the 0.002K results in Figure 6.5) make any such relationships hard to attain from the data. This noise is thought to result from the fact that the characteristic skill, S , for the forecasts made from larger initial perturbations is lower resulting in a greater sensitivity of the results to the variability seen in all curves in Figure 6.3. Examination of τ for spatial scales of 10km between the different plots in Figure 6.5 do suggest that this hypothesis may be verified. For example, with initial errors of 0.002K, τ is around 35 minutes. With initial errors of 0.2K, τ is only 30 minutes. However, it is hard to draw any firm conclusions on this given the noise present in the data. Further experiments using a larger ensemble of simulations would probably help to reduce this noise.

6.5 Examination of saturated perturbation structure

The largest perturbations inserted in the model had an initial value of γ greater than two (see Figure 6.3). An examination of the vertical velocity in the positively and negatively perturbed runs (from each ensemble member) in the ensemble made from perturbations with a 1.0K initial amplitude reveals that the perturbations are so large that they change the locations of convection (see Figure 6.6), i.e. individual convective plumes (indicated by their updraughts) are located in different places in each of the perturbed runs. This indicates that the errors can become no larger since they are already as different from each other as they can ever be in the absence of any larger scale instability. This examination of the perturbation structure confirms that perturbations inserted with an initial amplitude of 1.0K have no skill in forecasting the locations of individual convective storms in this case study.

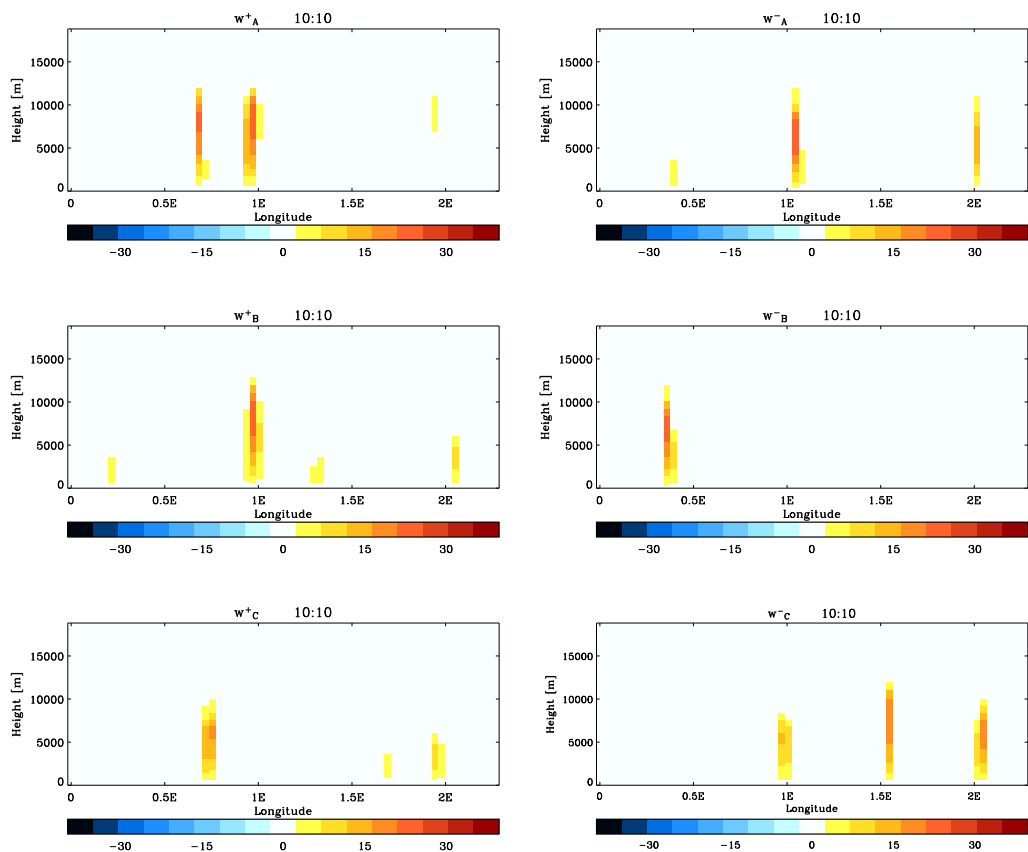


Figure 6.6: Cross-sections of vertical velocity at 1.16N for the positively and negatively perturbed runs in each ensemble member. The perturbations were inserted at 500m height with amplitude 1.0K.

6.6 Chapter summary

- A definition of error saturation involving the ratio of the spectral density (related to the variance) of a perturbation field to the spectral density in a single forecast was presented.
- An experiment was conducted in which potential temperature perturbations of different amplitude were inserted and allowed to grow and saturate. The timescale over which these perturbations saturated was investigated as a function of horizontal spatial scale.
- The resulting error growth curves revealed that **perturbations saturate more rapidly at small spatial scales and when their initial amplitude is larger.**
- A new metric, S , related to the overall skill of a forecast over a finite time was suggested. The results showed that forecasts starting from initial conditions with smaller errors contain more skill overall than those starting from data with larger errors. **Forecasts starting with errors of 1.0K (estimated to be approximately equal to current analysis errors) have little or no skill at forecasting features at scales below 128km.**
- A second metric, τ , designed to be representative of the error saturation timescale was also suggested. These quantitative results confirmed the findings of the qualitative analysis of the error growth curves. i.e. errors in forecasts of features at larger spatial scales saturate over a longer timescale than those at smaller scales. However, the results were less clear regarding the dependence of error saturation timescale with the initial amplitude of the perturbations. This was thought to be due to the greater sensitivity of τ to noise in the error growth curves as the overall skill decreases.
- The results indicate that the **lower limit** to the range of predictability (representing the accuracy of current forecasts) is **almost zero at convective scales**, i.e. current analysis errors are so large that forecasts of features at convective scales have no skill in situations similar to a cold air outbreak.
- The results suggest that the **upper limit** to the range of predictability (representing the maximum lead time over which forecasts will *ever* be skillful) lies at around **200 minutes for features at 10km horizontal scales, 260 minutes at 20km scales, and 275 minutes for features at 100km scales** in situations similar to a cold air outbreak. However, the method adopted in this experiment means that these results ignore errors associated with the unresolved scales. This could mean that these results are an *overestimation* of the actual error saturation timescales in these situations.

CHAPTER SEVEN

Conclusions and discussion of the implications

The predictability of the first kind of the initiation of convective showers over the ocean during homogeneous destabilisation has been investigated in a mesoscale model in this thesis. The non-hydrostatic Met Office Unified Model was run with a horizontal resolution of 4km without the use of a convective parameterisation scheme. An idealised simulation of convective initiation during a cold air outbreak was setup. The growth of initial condition uncertainty into errors in short-range weather forecasts of convective initiation was then examined using the dynamical method (Lorenz, 1969b), i.e. the divergence of the states of forecasts initiated from initial conditions differing only by a small perturbation was examined. Moist static stability perturbations were made by adding random fields to and subtracting random fields from the potential temperature, θ , at a single height. The evolution of these perturbations was then examined to understand the nature of error growth in the first three hours of the forecast.

Several experiments were conducted, each designed to address an individual thesis aim. The conclusions from these experiments are presented below in the context of the original thesis aims.

7.1 Conclusions

Aim 1: Understand the dominant mechanisms acting to grow initial condition errors in the first 3 hours of the forecast

- Two perturbation growth mechanisms were found to dominate during the first three hours of the forecast. These mechanisms were identified through an analysis of the structure of the perturbation fields.
 1. Boundary layer regime changes caused by the perturbations occurred and resulted in different profiles of heat and moisture within the boundary layer between the perturbed forecasts at certain locations highly sensitive to small potential temperature perturbations. The potential temperature profiles at these sensitive boundary layer locations were close to a threshold in the boundary layer parameterisation scheme which defined different boundary layer types. The differences in the forecasts caused by this mechanism were dominant over other mechanisms during the first 60 minutes of the forecast. To the author's knowledge, this specific mechanism in which small uncertainty in the initial conditions of the boundary layer can result in relatively large forecast differences over such short timescales, has not been described before.
 2. Convective instability became the dominant perturbation growth mechanism following the initiation of deep convection in this case study, approximately 60 minutes into the forecast.
- Perturbation growth by the first mechanism early in the forecast was shown to contribute to the overall perturbation growth later in the forecast after convective instability had acted. Consequently, some storms had larger perturbation structures associated with them than others. Therefore, the perturbation growth due to boundary layer regime changes did not become irrelevant after the action of convective instability.
- The random distribution of the locations at which each mechanism occurred suggested that the two mechanisms acted independently of each other.
- Perturbations were found to spread vertically via wave processes. Consequently, perturbations initially confined to the mid-troposphere rapidly propagated down into the boundary layer and seeded rapid perturbation growth there.

Aim 2: Quantify the growth rate of initial condition errors in the forecast as a function of spatial scale

- A Fourier analysis of the evolution of the perturbation fields with time revealed that perturbation growth was more rapid at smaller horizontal spatial scales. Perturbation doubling times of 12 minutes were observed at the 10km horizontal scale, compared with almost 2 hours at 30km.
- At scales between 10km and 40km, the linear theory of convection provided a reasonable description of the relationship between perturbation growth rate and spatial scale during the initiation of deep convection in this simulation.
- The linearity of the perturbation growth was quantified using a metric based on the symmetry of initially equal and opposite perturbations. Perturbation growth due to boundary layer regime changes was found to be highly non-linear in nature. The linearity of the perturbation growth associated with convective instability could not be determined as it occurred after the non-linear growth in the boundary layer.
- Super-exponential perturbation growth was observed at scales larger than those of the convective forcing, i.e. above around 40km.

Aim 3: Quantify the timescale over which initial condition errors lead to forecasts with no skill (error saturation timescale) as a function of spatial scale and initial error amplitude

- A definition of error saturation was made involving the correlation of two forecasts initiated from slightly different initial conditions. Secondly, a new metric, τ , was defined which was related to the timescale over which the perturbations tended towards saturation. τ was then calculated as a function of the initial perturbation amplitude and horizontal spatial scale.
- Perturbations with a mean initial amplitude of only 0.002K were found to saturate after approximately 200 minutes at the 10km scale compared with approximately 275 minutes at the 100km scale. i.e. **Forecasts of individual convective showers over the ocean under homogeneous forcing are unlikely to ever be accurate beyond approximately 4 hours.**
- Perturbations with a mean initial amplitude of 1.0K (approximately equal to the current

analysis errors in potential temperature at convective scales) were found to saturate almost immediately. i.e. shallow convective features are not adequately resolved by current analyses.

- It seems likely that these values are *overestimates* of the actual timescale over which forecasts lose skill since the method employed here implicitly assumed that the sub-grid scales were error-free (see section 7.3.2).

7.2 Discussion of the implications of the results

These results have revealed (or perhaps confirmed) that individual oceanic convective showers are essentially unpredictable. The results suggest that forecasts made from analyses with current errors cannot predict the timing and location of individual showers. The reduction in analysis errors required for a skillful forecast of these features out to 4 hours (from $\sim 1\text{K}$ to $\sim 0.002\text{K}$) seems unachievable in the near future.

Another important outcome of this thesis was the appreciation of the importance of gravity waves in the propagation of initial condition errors into previously error-free areas. This result implies that although forecasts of convective storms are more sensitive to initial condition uncertainty within the boundary layer, any uncertainty initially confined to the mid-troposphere will soon be propagated to the boundary layer and seed forecast errors from there.

7.2.1 Implications for convective scale data assimilation

The results found here have significant implications for convective scale data assimilation. The methodology of data assimilation assumes that useful information exists in the short-term forecast (background state) which can then be combined with new observations to produce an analysis which is more accurate than either of the two individually. However, these results show that forecasts of small scale features can lose all skill within a few tens of minutes. Therefore, for the background state to contain any useful information the data assimilation cycle would have to be very short.

In addition, the non-linearity of the error growth observed in section 5.5 is likely to be problematic in data assimilation where a linear assumption is usually made.

The current temperature observational error is similar to the variability of the temperature within convective storms and the observational spatial sampling is on the same order as the spatial variability of these fields. However, it is important to note that assimilation of other variables which resolve convective features better (such as radar reflectivity) may allow the associated temperature field to be inferred. Therefore, the possibility remains that significant improvements can be made to analyses of potential temperature at the convective scale.

7.2.2 Implications for convective scale ensemble forecasting

Over the past 40 years, computing power has approximately doubled every two years, as predicted by Moore's Law (Moore, 1965). If this continues, then within a decade it will be possible to run an ensemble of 50 forecasts operationally with a horizontal resolution of 4km on a domain covering the United Kingdom. In the following 10 years it would be possible to run the same system at 1km resolution. Considering the success of ensemble forecasting at synoptic scales, it may seem obvious that ensemble forecasting at convective scales will bring similar benefits. However, the results in this thesis have highlighted a major difference between error growth at synoptic scales and those at convective scales; errors at the scale of convective showers saturate far more rapidly than those at synoptic scales.

Ensemble forecasts can provide no benefit over a forecast of the climatology of the situation once the errors have saturated. For example in the case study examined in this thesis, the climatology of the situation describes a field of scattered showers with an equal probability of convective initiation at any point across the domain. Before the errors have saturated, an ensemble forecast may yield some information about the locations where convective initiation is more probable. However, once the errors have saturated, the ensemble mean (given a suitably large sample) would indicate no preferred location for convective initiation.

In the case of explicit forecasts of oceanic convective showers where the errors are shown to saturate very rapidly, the additional benefits of using a high resolution ensemble forecasting system over the use of a single low resolution deterministic forecast using convective parameterisation

seem slight. However, not all convective showers are formed under conditions of homogeneous destabilisation over a homogeneous surface (see section 7.4.2).

If ensemble forecasts were attempted at convective scales then the construction of optimal perturbations (see section 1.7.5) may prove problematic due to the highly non-linear nature of the perturbation development. Singular vectors which make the linear assumption may not be suitable for the construction of optimal perturbations in this case.

7.3 Discussion of the limitations of this work

This thesis has provided some new information about the predictability of convective showers. However, it is important that the results are not taken out of context and that the limitations of the method used are recognised.

The experiments in this thesis have used a numerical model to make inferences about the predictability of convective showers in the atmosphere. However, no numerical model can ever be a perfect representation of the real atmosphere. This fact results in limitations of this method's ability to achieve the thesis aims. These are discussed in the following sections.

7.3.1 Boundary layer regime changes in the real atmosphere

The growth of perturbations by differences in the evolutions of the boundary layer regimes between two perturbed forecasts was observed in the Unified Model. This is possible because of the way in which the boundary layer is modelled by the non-local boundary layer parameterisation scheme (Lock *et al.*, 2000). This scheme determines the mixing profiles of heat, moisture and momentum based on predefined reference profiles for different boundary layer types e.g. stable, well-mixed or cumulus capped. The boundary layer type is diagnosed using the existing profiles of potential temperature and specific humidity in the boundary layer. At some locations, small perturbations to the potential temperature can change the diagnosed boundary layer type resulting in a new mixing profile and significant modification to the boundary layer structure.

However, different numerical models use other parameterisation schemes, many of which do not

involve the diagnosis of a boundary layer ‘type’. This raises the issue of whether or not this error growth mechanism is merely an artifact of this particular numerical model.

Observations have shown that the atmospheric boundary layer does exhibit qualitatively distinct regimes of behaviour within which thermodynamic structures are maintained in quasi-equilibrium (Betts, 1986). Furthermore, the transition between the regimes can occur rapidly e.g. the sudden formation of a field of cumulus clouds from a clear sky. Figure 7.1 shows an infra-red satellite image over the Atlantic Ocean. Several different boundary layer types can be seen. An area of stratocumulus (labelled ‘i’) borders an area of open-cell shallow cumulus (‘ii’) indicated by the relatively warm (grey) cloud tops which lie adjacent to cumulonimbus showers (‘iii’) indicated by the relatively cold (white) cloud tops. It can be seen that the length scale of the regime transition is small compared with the length scale over which the different regimes exist. This is further evidence of distinct boundary layer regimes in the atmosphere with rapid inter-regime transitions. However, although the transitions between the regimes in the atmosphere can be rapid, they are not instantaneous as is the case in the parameterisation scheme used here.

The existence of locations where the subsequent boundary layer regime is highly sensitive to the

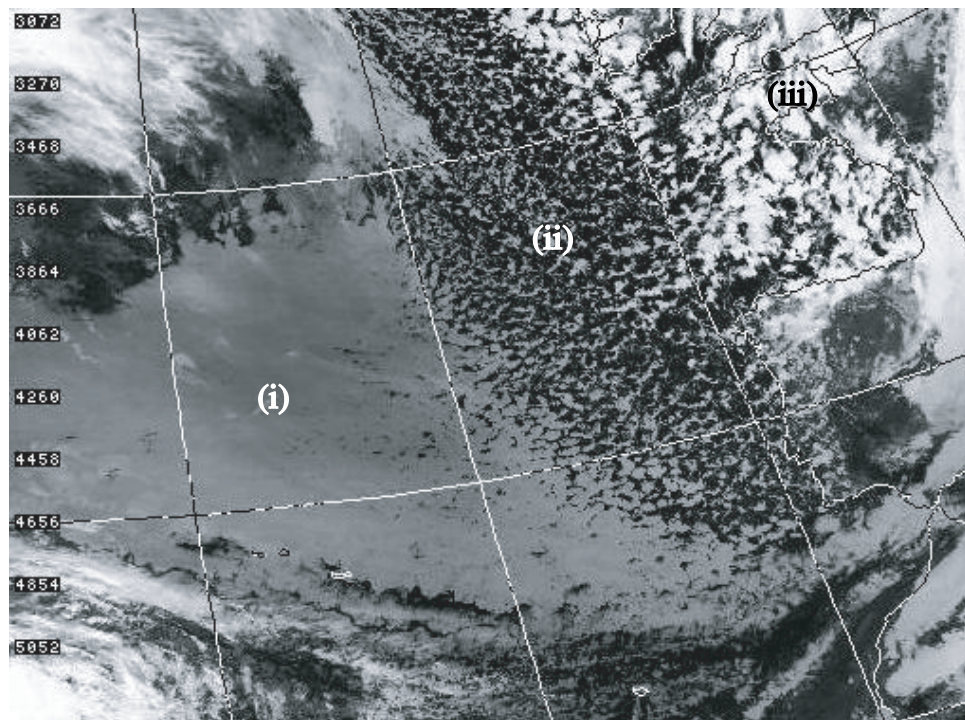


Figure 7.1: NOAA HRPT channel 5 (thermal infra-red) image from 25/12/04 over the Atlantic Ocean with Europe appearing on the right hand side. Different boundary layer regimes are marked (i), (ii) and (iii).

initial conditions seems probable. These locations can be thought of as analogous to locations on the Lorenz attractor situated between the two lobes, where small differences in the state can lead to dramatically different behaviour (Lorenz, 1993, p.14).

However, it seems likely that the magnitude of the perturbation growth by this mechanism, found in this study, was artificially high due to the model setup used. The boundary layer parameterisation scheme was designed for use at lower resolutions along with a convection scheme. The boundary layer scheme simulates the effects of all unresolved turbulent mixing within the boundary layer except for those within any diagnosed cumulus layers. If present, the convective parameterisation scheme simulates mixing in those cumulus layers. However, when running at higher resolution it is inappropriate to use this convective parameterisation scheme, therefore mixing within the cumulus clouds must be represented explicitly by the model dynamics. While the convective parameterisation scheme mixes instantaneously, the explicit convection cells in the model used here take time to ‘spin-up’ due to the high effective viscosity of the fluid in the model. The slow response of the convection to instability allows a localised build up of Convective Available Potential Energy (CAPE) within the cumulus layer which can be released instantaneously upon a change to a non-cumulus boundary layer type where mixing is dealt with directly by the parameterisation scheme.

It is recognised that this effect is an undesirable characteristic of this model setup. The importance of this effect on the results had not been anticipated at the time that the model was setup. Also, an alternative boundary layer scheme was not readily available. As stated in Chapter 1 the results should be interpreted in the context of this model setup and the likely differences between this and reality noted. However, even if the *magnitude* of error growth by this mechanism in these results may be too high, the *mechanism* itself may still exist in the atmosphere.

In summary, it seems likely that this mechanism of error growth is not merely an artefact of the model setup. However, the rate and magnitude of the error growth are likely to be different in more sophisticated representations of the boundary layer turbulent mixing. Further understanding of boundary layer regime transitions in the atmosphere through new observations and modelling would be highly beneficial to understanding the extent to which the results regarding this mechanism are applicable to the predictability of convective showers.

7.3.2 The implicit assumption of error-free sub-grid scales

When studying the divergence of two forecasts initiated from slightly different initial conditions, an implicit assumption is made that the sub-grid scales are error free. However, when comparing a forecast with reality, differences existing in the sub-grid scales are transferred upscale and lead to errors in the forecast at resolved scales (Lorenz, 1969a). This fact was recognised from the outset in this thesis, but its implications must be noted.

The error saturation timescales determined in Chapter 6 (through an examination of the time taken for two forecasts to become decorrelated) are likely to be *overestimates* of the time taken for a forecast to become decorrelated with reality due to the effect of the unresolved scales. Errors in the resolved scales arriving from the sub-grid scales will result in a more rapid decorrelation of the forecast with reality. Any such contamination of the forecast from the unresolved scales requires an upscale transfer of energy to exist at the grid scale. Understanding of upscale transfer mechanisms at convective scales is currently low (Tribbia and Baumhefner, 2004), therefore the extent of the overestimation of the error saturation timescale in this thesis is not easily determined.

Previous studies have used observations to estimate the error saturation timescale in the atmosphere. Germann and Zawadzki (2002) used Lagrangian persistence to forecast precipitation patterns based on radar observations, i.e. the radar echoes were advected to produce a short-range forecast. The increase in forecast skill achievable by filtering out the smallest (unpredictable) scales was then investigated by a low-pass filtering of both the forecasts and the radar observations. A forecast ‘lifetime’ was then defined by measuring the timescale over which the forecasts and observations became decorrelated. The results for several different case studies are shown in Figure 7.2. In each case, the inclusion of small spatial scales results in a reduction of the forecast lifetime. This implies that features at small spatial scales have a shorter predictability timescale than those at larger scales, in agreement with the results from this thesis.

The timescales of predictability for a particular scale found in that study cannot be compared directly with those in this thesis since different measures of predictability were used. The *low-pass* filtering method used in Germann and Zawadzki (2002) mean that the results at the smallest scales (e.g. 10km) also include larger (more predictable) scales which explains why the predictability timescales are longer than those seen in Chapter 6. It is interesting to note that the forecast lifetimes differ by up to a factor of two between the different case studies.

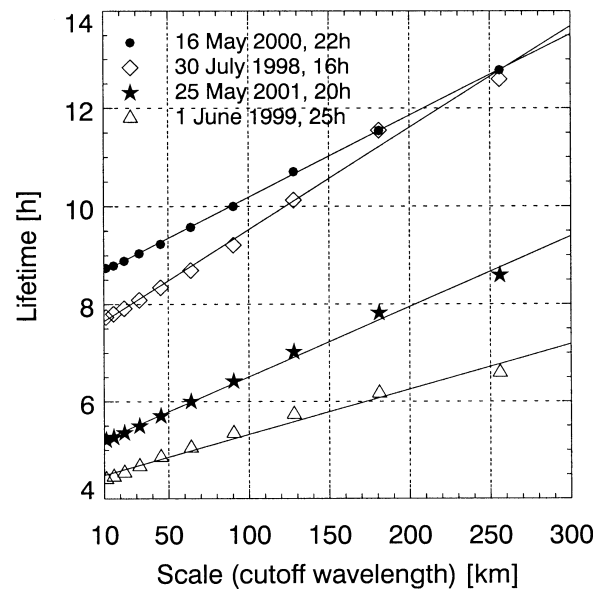


Figure 7.2: Decorrelation time (lifetime) between Lagrangian persistence based nowcasts of precipitation and radar observations as a function of the smallest spatial scale allowed. The results from several case studies are presented. [Figure taken from Germann and Zawadzki (2002)].

7.3.3 Limitations of the model setup

Computational restraints prevented horizontal grid lengths of $\sim 100\text{m}$, desirable for entirely explicit representation of energy containing convective eddies, from being used in the model. The 4km horizontal grid lengths used here tend to produce convective storms which are slower to initiate, but eventually more vigorous than those in reality. The use of a model with a shorter grid length would be more likely to provide results more representative of the real atmosphere.

Finally, it must be remembered that this thesis addressed only one specific problem, i.e. that of the predictability of the first kind for the initiation of convective showers over the ocean forced by homogeneous destabilisation. The results produced, and conclusions made, are only applicable to that precise situation. Any inferences made about the predictability of convective showers over land where the forcing tends to be more localised, or the predictability *after* convective initiation, are invalid. Further work is required to understand the predictability of deep convection in all of the situations in which it can occur.

7.4 Directions for future work

7.4.1 Further work on this case study

In order to address the issue of the unresolved scales, further work on identifying possible upscale energy transfer mechanisms at the convective scales would be very useful. A comparison of simulations run at different resolutions can allow the influence of the small scales on the larger scales to be assessed. Furthermore, repeating the experiments of this thesis using a shorter grid-length may provide a better representation of the convective storms themselves and produce results more applicable to the atmosphere. In addition, sensitivity studies could be conducted to assess the impact of parameters such as destabilisation rate and coriolis force on the perturbation growth.

The idealised framework used in this thesis has allowed perturbation growth associated with convective instability to be isolated from baroclinic and barotropic instability acting at large scales. However, in real case studies, these instabilities are unlikely to be so well separated. Cold air outbreaks usually occur after the passage of a cold front associated with a baroclinic extra-tropical cyclone. Therefore, the growth of forecast errors in these conditions may be significantly different from those calculated in this thesis. Further work studying the problem of the predictability of the first kind for convective initiation over the ocean could use real case studies of cold air outbreaks to assess the differences from the idealised case studied here.

7.4.2 Convective initiation under inhomogeneous forcing

This thesis has studied the predictability of the first kind of convective initiation under conditions of homogeneous forcing. However, convection over the land (where it affects far more people) is often triggered as the result of inhomogeneous forcing. Examples include convergence lines where moisture convergence can lead to a localised increase in buoyancy and convective initiation (Weckworth, 2000) and upper level potential vorticity anomalies which can lead to localised areas of enhanced convective destabilisation (Roberts, 2000a). A study by Jorgensen and Weckworth (2003) demonstrated that the locations where convective rolls and sea breeze fronts intersect provide conditions preferable for convective initiation. Similarly, orography can act to enhance destabilisation locally through a number of mechanisms (Houze, 1993, p.534). It may be that the

predictability (of the first kind) under such forcing may be very different from the case of homogeneous destabilisation studied in this thesis. Research in this area could prove very interesting.

Furthermore, even if the first kind of predictability of storms initiating in areas of localised forcing turns out to be equally low, then it does not mean that useful forecasts of these features are not possible. If the storms have a high predictability of the second kind (see section 1.2.1), then useful forecasts can be made. Figure 7.3 is reproduced from a forecasters handbook (Met.Office, 1997) and illustrates areas more likely to be affected by convective showers over the British Isles during the winter under different wind directions. Lines of showers are commonly observed similar to those shown in this figure associated with localised areas of enhanced forcing. Although forecasts of individual showers may not be possible with any skill, the (often small) regions affected by the showers can be well forecast and provide useful information.

Mesoscale Convective Systems are clusters of convective storms which have a lifetime greater than any individual convective cell component Houze (1993). These can be viewed as localised regions of forcing. To make useful forecasts of a mesoscale convective system, the forecasts of the individual convective cells need not be accurate provided that the forecasts of the region of forcing have reasonable skill. The predictability of these areas of forcing may be substantially greater than that of the individual convective storms. For example, Figure 7.4 shows the locations of lightning strikes associated with a mesoscale convective system (marked by an arrow). It can be seen that the path of the system seems relatively predictable since the direction of motion changed little over the 20 hour lifetime of the system.

In August 2004, a series of convective storms were triggered along a stationary convergence line near Boscastle in southwest England. Since all the storms triggered over the same location, the accumulated precipitation totals were very high and resulted in flash floods and considerable damage to property and local infrastructure. Despite the fact that the individual storms were only a few kilometers across, a 4km resolution NWP model had great success in forecasting the accumulated totals 12 hours prior to initiation (May *et al.*, 2004). This example illustrates that even though the forecasts of the individual storms within the area of forcing may have been inaccurate (i.e. the errors were saturated), detailed and accurate forecasts of the small region affected by the storms could be made providing that the features forcing the convection were forecast accurately. Studies on the predictability of these mechanisms (as opposed to the convection that they generate) may be of great benefit to the design of a convective scale ensemble forecasting system.

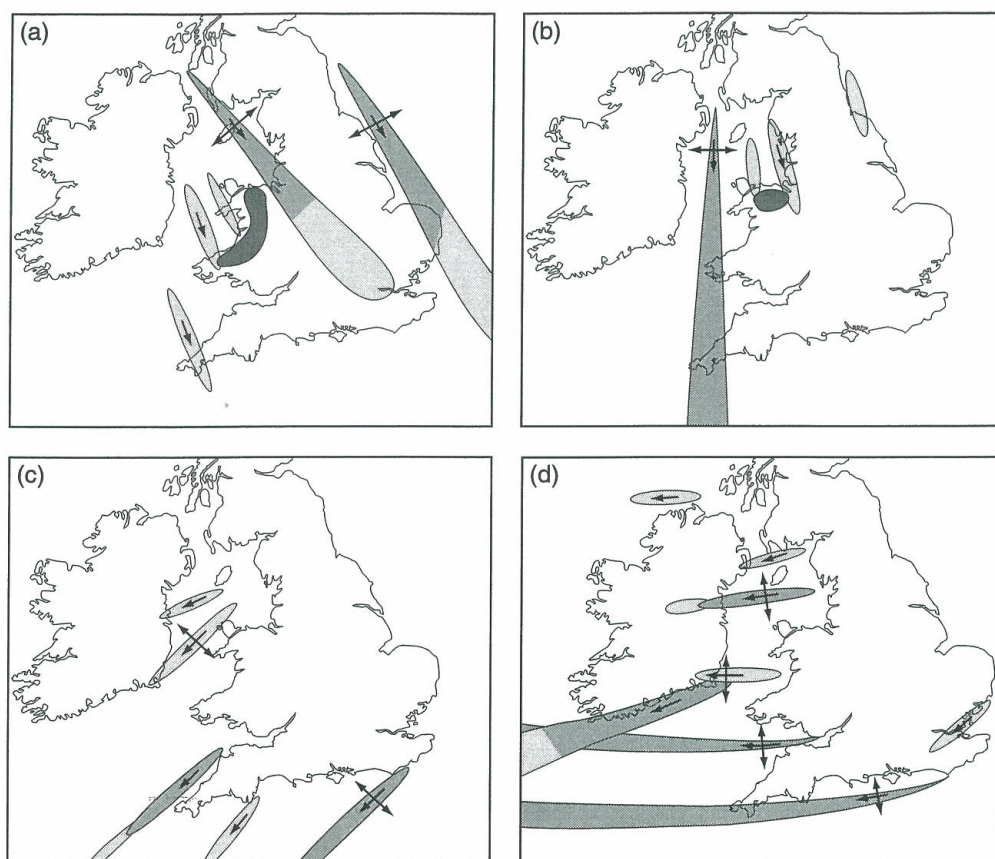


Figure 7.3: Areas expected to be affected by convective showers (shaded regions) in winter in (a) North-westerly air flow, (b) northerly air flow, (c) north-easterly air flow, and (d) easterly air flow. Shading shows the frequency of occurrence and arrows are indicative of the uncertainty in the alignment of the shower bands. [Reproduced from Met. Office (1997)].

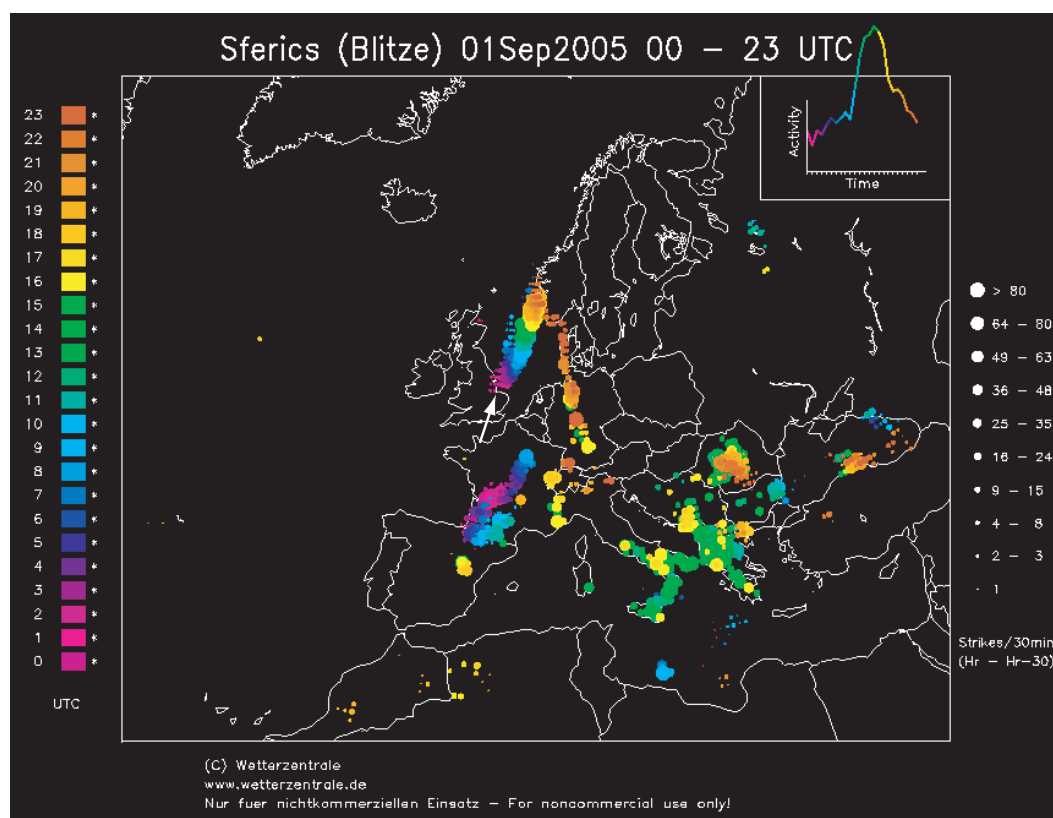


Figure 7.4: Map of locations of lightning strikes (circles) observed using sferics. Strike rate indicated by size of circle. Time of strikes indicated by colour of the circles. The arrow marks the storm mentioned in the text. [Image courtesy of www.wetterzentrale.de].

In such situations it is possible that a high resolution convective scale ensemble forecasting system may provide additional information about the areas affected by convective storms over a low resolution model where convection is parameterised, since the small scale processes leading to convective initiation can be represented more accurately. Further work into the predictability of the second kind of convective showers initiated under inhomogeneous forcing would be very useful.

The results from this thesis have shown the inherent unpredictability of individual small oceanic convective showers. However, these are likely to represent a ‘worst case scenario’ in terms of the potential for accurate forecasting of convective storms. Unlike the homogeneous forcing of the idealised case study used here, most precipitating convection over land can be tied to distinct localised forcing features (such as convergence lines and orography). Further research is required to understand error growth in these conditions of inhomogeneous destabilisation. However, the potential remains for improved forecasts of convective storms through better forecasts of the features that trigger them.

APPENDIX A

Linearisation of the logistic map

A linearisation of the non-linear map can be used to estimate the growth of perturbations that can be considered small. This is achieved by defining a background state, X^b , about which a small perturbation, δX , grows. Hence,

$$X_{n+1} = \alpha X_n (1 - X_n)$$

$$X = X^b + \delta X$$

$$X_{n+1}^b + \delta X_{n+1} = \alpha \left(X_n^b + \delta X_n \right) \left(1 - \left(X_n^b + \delta X_n \right) \right)$$

$$X_{n+1}^b + \delta X_{n+1} = \alpha \left(X_n^b - \left(X_n^b \right)^2 - X_n^b \delta X_n + \delta X_n - \delta X_n X_n^b - \left(\delta X_n \right)^2 \right).$$

Terms of order $(\delta X_n)^2$ can be considered small here and so are removed,

$$X_{n+1}^b + \delta X_{n+1} = \alpha \left(X_n^b \left(1 - X_n^b \right) - \delta X_n \left(2X_n^b - 1 \right) \right)$$

and using the fact that $X_{n+1}^b = \alpha X_n^b (1 - X_n^b)$ we can find an expression in terms of δX ,

$$\delta X_{n+1} = -\alpha \delta X_n (2X_n^b - 1).$$

APPENDIX B

The linear theory of moist convection

Linear theory can be used to predict the expected growth rate of small perturbations to a basic state. Here, the full momentum equations are first presented, followed by scale analysis for a convective system to remove insignificant terms. Then these, along with the thermodynamic and continuity equations are linearised for small perturbations to a basic state. Finally, the evolution of the vorticity in the x-z plane is described and solved to find the expected growth rate.

B.1 Momentum equations

Navier Stokes equations are written as:

$$\frac{D\mathbf{V}}{Dt} + f\mathbf{k} \times \mathbf{V} = -\frac{1}{\rho}\nabla p + \mathbf{g} + \mathbf{F}$$

where $\mathbf{V} = (u, v, w)$	- velocity vector
$\mathbf{g} = (0, 0, -g)$	- gravitational acceleration
$f \equiv 2\Omega \sin\phi$	- coriolis parameter
p	- pressure
ρ	- density

$$\mathbf{F} = \nu \nabla^2 \mathbf{V} \quad \text{- frictional acceleration}$$

$$\nu \quad \text{- kinematic viscosity coefficient}$$

which expanded out in cartesian co-ordinates and using a shallow atmosphere approximation ($r=a$) gives each component,

x component:

$$\frac{Du}{Dt} - \frac{w \tan \phi}{a} + \frac{uw}{a} = -\frac{1}{\rho} \frac{\partial p}{\partial x} + 2\Omega v \sin \phi - 2\Omega w \cos \phi + F_{rx}$$

y component:

$$\frac{Dv}{Dt} - \frac{u^2 \tan \phi}{a} + \frac{vw}{a} = -\frac{1}{\rho} \frac{\partial p}{\partial y} + 2\Omega u \sin \phi + F_{ry}$$

z component:

$$\frac{Dw}{Dt} - \frac{u^2 + v^2}{a} = -\frac{1}{\rho} \frac{\partial p}{\partial z} - g + 2\Omega u \cos \phi + F_{rz}$$

Here only the acceleration, pressure gradient and gravity terms are considered giving the following simplified momentum equations:

$$\frac{Du}{Dt} = -\frac{1}{\rho} \frac{\partial p}{\partial x}$$

$$\frac{Dv}{Dt} = -\frac{1}{\rho} \frac{\partial p}{\partial y}$$

$$\frac{Dw}{Dt} = -\frac{1}{\rho} \frac{\partial p}{\partial z} - g.$$

B.2 Linearising the momentum equations

These equations can be linearised if the variables are thought of as consisting of a basic state and a small perturbation from that state: $u = \bar{u} + u'$

$$v = \bar{v} + v'$$

$$w = \bar{w} + w'$$

$$p = \bar{p} + p'$$

$$\rho = \bar{\rho} + \rho'$$

where an overbar represents the basic state, and a ‘ $'$ ’ indicates a perturbation. Linear theory assumes that the perturbations are so small that they do not significantly change the flow and that the product of perturbations are negligible. In this way the full non-linear equations become linear.

Here, the basic state is assumed to be at rest, with no variations in the horizontal, but some variations in the vertical can be defined i.e. $p = \bar{p}(z) + p'(x, y, z, t)$, $\rho = \bar{\rho}(z) + \rho'(x, y, z, t)$, $\bar{u} = \bar{v} = \bar{w} = 0$, $u = u'(x, y, z, t)$, $v = v'(x, y, z, t)$, $w = w'(x, y, z, t)$, and the basic state is assumed to be in hydrostatic balance:

i.e.

$$\frac{1}{\bar{\rho}} \frac{\partial \bar{p}}{\partial z} = -g. \quad (\text{B.1})$$

This leads to the following linearisation of the x component of the momentum equation:

$$\frac{\partial u'}{\partial t} + u' \frac{\partial u'}{\partial x} + v' \frac{\partial u'}{\partial y} + w' \frac{\partial u'}{\partial z} = -\frac{1}{(\bar{\rho} + \rho')} \frac{\partial (\bar{p} + p')}{\partial x}$$

where terms containing the products of perturbations can be assumed to be negligible,

$$\frac{\partial u'}{\partial t} = -\frac{1}{(\bar{\rho} + \rho')} \frac{\partial (\bar{p} + p')}{\partial x}$$

$$= -\frac{1}{(\bar{\rho} + \rho')} \left(\frac{\partial p'}{\partial x} + \frac{\partial \bar{p}}{\partial x} \right)$$

and the since variation of pressure in the horizontal was previously defined to be zero,

$$= -\frac{1}{(\bar{\rho} + \rho')} \frac{\partial p'}{\partial x}.$$

Expanding the first term on the right hand side using a Taylor series,

i.e.

$$\frac{1}{(\bar{\rho} + \rho')} = \frac{1}{\bar{\rho}} \left(\frac{1}{1 + \frac{\rho'}{\bar{\rho}}} \right) = \frac{1}{\bar{\rho}} \left[1 - \frac{\rho'}{\bar{\rho}} + \left(\frac{\rho'}{\bar{\rho}} \right)^2 + \dots \right]$$

gives

$$\frac{\partial u'}{\partial t} = -\frac{1}{\bar{\rho}} \left(1 - \frac{\rho'}{\bar{\rho}} \right) \frac{\partial p'}{\partial x}$$

$$= -\frac{1}{\bar{\rho}} \left(\frac{\partial p'}{\partial x} - \frac{\rho'}{\bar{\rho}} \frac{\partial p'}{\partial x} \right)$$

where once again, products of perturbations are assumed to be zero, finally giving the linearised x -component of the momentum equation:

$$\frac{\partial u'}{\partial t} = -\frac{1}{\bar{\rho}} \frac{\partial p'}{\partial x} \tag{B.2}$$

similarly, for the y -component:

$$\frac{\partial v'}{\partial t} + u' \frac{\partial v'}{\partial x} + v' \frac{\partial v'}{\partial y} + w' \frac{\partial v'}{\partial z} = -\frac{1}{(\bar{\rho} + \rho')} \frac{\partial (\bar{p} + p')}{\partial y}$$

$$\frac{\partial v'}{\partial t} = 0. \tag{B.3}$$

The linearisation of the z -component differs from above due to the fact that the pressure field basic state does vary in the vertical,

$$\frac{\partial w'}{\partial t} + u' \frac{\partial w'}{\partial x} + v' \frac{\partial w'}{\partial y} + w' \frac{\partial w'}{\partial z} = -\frac{1}{(\bar{\rho} + \rho')} \frac{\partial(\bar{p} + p')}{\partial z} - g$$

removing terms containing the product of perturbations leads to,

$$\frac{\partial w'}{\partial t} = -\frac{1}{\bar{\rho}} \left(1 - \frac{\rho'}{\bar{\rho}} \frac{\partial(\bar{p} + p')}{\partial z} \right) - g$$

which can be expanded as follows,

$$\frac{\partial w'}{\partial t} = -\frac{1}{\bar{\rho}} \left(1 - \frac{\rho'}{\bar{\rho}} \frac{\partial \bar{p}}{\partial z} + \frac{\partial p'}{\partial z} \right) - g$$

$$\frac{\partial w'}{\partial t} = -\frac{1}{\bar{\rho}} \frac{\partial \bar{p}}{\partial z} - \frac{1}{\bar{\rho}} \frac{\partial p'}{\partial z} + \frac{\rho'}{\bar{\rho}} \frac{\partial \bar{p}}{\partial z} - g \quad (\text{B.4})$$

recalling the fact that the basic state is in hydrostatic balance (eqn. B.1), two terms can be removed, and the remaining $\frac{1}{\bar{\rho}} \frac{\partial \bar{p}}{\partial z}$ term can be set equal to -g. This yields the linearised vertical momentum equation,

$$\frac{\partial w'}{\partial t} = -\frac{1}{\bar{\rho}} \frac{\partial p'}{\partial z} - g \left(\frac{\rho'}{\bar{\rho}} \right). \quad (\text{B.5})$$

B.3 Thermodynamic equation

For a pseudo-adiabatic process, the equivalent potential temperature, θ_e , is conserved. Therefore the thermodynamic equation is simply,

$$\frac{D\theta_e}{Dt} = 0 \quad (\text{B.6})$$

Again, this can be linearised by assuming that the full field consists of a basic state, and a perturbation away from that.

$\theta_e = \bar{\theta}_e + \theta'_e$ where $\bar{\theta}_e = \bar{\theta}_e(z)$

$$\frac{D(\bar{\theta}_e + \theta'_e)}{Dt} = 0$$

$$\frac{D\bar{\theta}_e}{Dt} + \frac{D\theta'_e}{Dt} = 0. \quad (\text{B.7})$$

Neglecting the density differences caused by the presence of water vapour, the buoyancy of the perturbation with respect to the basic state can be described by,

$$b' = g \frac{\theta'_e}{\bar{\theta}_e}$$

we can write equation B.7 in terms of buoyancy by multiplying it by $\frac{g}{\bar{\theta}_e}$,

$$\frac{g}{\bar{\theta}_e} \frac{D\bar{\theta}_e}{Dt} + \frac{g}{\bar{\theta}_e} \frac{D\theta'_e}{Dt}$$

$$\frac{g}{\bar{\theta}_e} \frac{D\bar{\theta}_e}{Dt} + \frac{Db'}{Dt} = 0$$

$$\frac{g}{\bar{\theta}_e} \left(\frac{\partial \bar{\theta}_e}{\partial t} + u' \frac{\partial \bar{\theta}_e}{\partial x} + v' \frac{\partial \bar{\theta}_e}{\partial y} + w' \frac{\partial \bar{\theta}_e}{\partial z} \right) + \frac{Db'}{Dt} = 0$$

$$\frac{Db'}{Dt} + \frac{g}{\bar{\theta}_e} \frac{\partial \bar{\theta}_e}{\partial z} w' = 0.$$

Assuming a saturated environment, the moist static stability parameter can be defined as,

$$N_m^2 = \frac{g}{\bar{\theta}_e} \frac{\partial \bar{\theta}_e}{\partial z} \quad (\text{B.8})$$

which gives,

$$\frac{Db'}{Dt} + N_m^2 w' = 0$$

which can be expanded to,

$$\frac{\partial b'}{\partial t} + u' \frac{\partial b'}{\partial x} + v' \frac{\partial b'}{\partial y} + w' \frac{\partial b'}{\partial z} + N_m^2 w' = 0$$

removing terms containing the product of perturbations gives the linearised thermodynamic equation:

$$\frac{\partial b'}{\partial t} + N_m^2 w' = 0. \quad (\text{B.9})$$

B.4 Continuity equation

The continuity equation can be written as:

$$\frac{1}{\rho} \frac{D\rho}{Dt} + \nabla \cdot \mathbf{U} = 0$$

making Boussinesq approximation (i.e. assuming that the density is constant everywhere except in the buoyancy term) gives the continuity equation for an incompressible flow:

$$\nabla \cdot \mathbf{U} = 0$$

which expands to,

$$\frac{\partial u}{\partial x} + \frac{\partial v}{\partial y} + \frac{\partial w}{\partial z} = 0.$$

As before, this can be linearised:

$$\frac{\partial u'}{\partial x} + \frac{\partial v'}{\partial y} + \frac{\partial w'}{\partial z} = 0 \quad (\text{B.10})$$

giving the linearised continuity equation for an incompressible flow.

$$\frac{\partial u'}{\partial x} + \frac{\partial w'}{\partial z} = 0.$$

B.5 Describing the circulation

Now, the y-component of the vorticity equation describes the circulation in the x-z plane,

$$\xi_y = \frac{\partial u'}{\partial z} - \frac{\partial w'}{\partial x}. \quad (\text{B.11})$$

To describe how this circulation evolves with time, we can take $\frac{\partial}{\partial z}$ (B.2)

$$\frac{\partial}{\partial z} \left(\frac{\partial u'}{\partial t} + \frac{1}{\bar{\rho}} \frac{\partial p'}{\partial x} \right) = 0$$

and $\frac{\partial}{\partial x}$ (B.3),

$$\frac{\partial}{\partial x} \left(\frac{\partial w'}{\partial t} + \frac{1}{\bar{\rho}} \frac{\partial p'}{\partial z} \right) = -\frac{\partial b'}{\partial x}$$

and subtract the two (as in eqn. B.11), leaving a $\frac{\partial}{\partial t}$ term from the momentum equations.

$$\frac{\partial}{\partial t} \left(\frac{\partial u'}{\partial z} + \frac{\partial w'}{\partial x} \right) = -\frac{\partial b'}{\partial x}$$

we now have an equation which describes the evolution of the circulation in the x-z plane in terms of buoyancy:

$$\frac{\partial \xi_y}{\partial t} = -\frac{\partial b'}{\partial x}. \quad (\text{B.12})$$

Now we can also find another expression for $\frac{\partial b'}{\partial x}$ using,

$$-\frac{\partial}{\partial x} \left(\frac{\partial b'}{\partial t} + w' N_m^2 \right) = 0$$

$$-\frac{\partial}{\partial x} \left(\frac{\partial b'}{\partial t} \right) - \frac{\partial w'}{\partial x} N_m^2 = 0$$

$$-\frac{\partial}{\partial x} \left(\frac{\partial b'}{\partial t} \right) = \frac{\partial w'}{\partial x} N_m^2$$

and using equation B.12,

$$-\frac{\partial}{\partial x} \left(\frac{\partial \xi_y}{\partial t} \right) = \frac{\partial w'}{\partial x} N_m^2$$

$$-\frac{\partial^2 \xi_y}{\partial x^2} = \frac{\partial w'}{\partial x} N_m^2. \quad (\text{B.13})$$

Now, using the continuity equation (eqn. B.10) for an incompressible fluid we can define a stream function in terms of perturbations away from the background state,

$$u' = \frac{\partial \psi}{\partial z}$$

$$w' = -\frac{\partial \psi}{\partial x}$$

and writing the y-component of the vorticity equation in terms of this streamfunction,

$$\xi_y = \frac{\partial^2 \psi}{\partial z^2} + \frac{\partial^2 \psi}{\partial x^2}$$

then substituting this into equation B.13 gives,

$$\frac{\partial^2}{\partial t^2} \left(\frac{\partial^2 \psi}{\partial z^2} + \frac{\partial^2 \psi}{\partial x^2} \right) = -N_m^2 \frac{\partial^2 \psi}{\partial x^2}. \quad (\text{B.14})$$

This equation has solutions of the form, $\psi = \psi_0 e^{i(kx+mz)+\sigma t}$, where k is the horizontal wavenumber, m is the vertical wavenumber and σ is the growth rate.

Substituting this solution into equation B.14 yields the growth rate, σ

$$\frac{\partial^2}{\partial t^2} \left(\frac{\partial^2}{\partial z^2} \psi_0 e^{i(kx+mz)+\sigma t} + \frac{\partial^2}{\partial x^2} \psi_0 e^{i(kx+mz)+\sigma t} \right) = -N_m^2 \frac{\partial^2}{\partial x^2} \psi_0 e^{i(kx+mz)+\sigma t}$$

$$\sigma^2 m^2 \psi_0 e^{i(kx+mz)+\sigma t} + \sigma^2 k^2 \psi_0 e^{i(kx+mz)+\sigma t} = -N_m^2 k^2 \psi_0 e^{i(kx+mz)+\sigma t}$$

$$\sigma^2 m^2 + \sigma^2 k^2 = -N_m^2 k^2$$

$$\sigma = \sqrt{-\frac{N_m^2 k^2}{m^2 + k^2}}.$$

Then defining an aspect ratio for the convection cell, $\beta = \frac{k}{m}$,

$$\sigma = \sqrt{-\frac{N_m^2 \frac{k^2}{m^2}}{1 + \frac{k^2}{m^2}}}$$

we find the growth rate of the circulation,

$$\sigma = \sqrt{-\frac{N_m^2 \beta^2}{1 + \beta^2}}$$

with the limits that $\sigma \rightarrow \Re(N_m)$ as $\beta \rightarrow \infty$ and that $\sigma \rightarrow 0$ as $\beta \rightarrow 0$. i.e. tall, narrow cells grow faster than short, wide ones.

APPENDIX C

Summary of experiments

A number of experiments were conducted in this thesis. Each experiment used a unique perturbation strategy. The strategies employed are summarised in table C.1 below.

	Time of insertion	Initial amplitude [K]	Height of insertion [m]
MAIN	08:30	0.002K	500m
LEV	08:30	0.002K	4500m
TARGET	09:50	0.002K	4500m
AMPa	08:30	0.02K	500m
AMPb	08:30	0.2K	500m
AMPc	08:30	1.0K	500m

Table C.1: The amplitude and height of insertion for the perturbations used in the experiments in this thesis.

APPENDIX D

Understanding the meaning of τ

A new metric, τ , was defined in Section 6.4.3 as follows,

$$\tau = \frac{\int_0^T t(2 - \gamma) dt}{\int_0^T (2 - \gamma) dt}.$$

This was designed to give a measure of the timescale over which the perturbations tend towards saturation (as measured by the ratio of the perturbation spectral density to the full field spectral density, γ). However, the values of τ should not be directly interpreted as a timescale. The properties of this metric are investigated here with the use of several simple curves to represent γ . The values of τ that would result from these curves are calculated in order to gain a better understanding of the meaning of the results in section 6.4.3.

Curves of the form,

$$\gamma = 2 - Ae^{-\frac{t}{T}} \tag{D.1}$$

are considered. These tend towards a saturation value (i.e. $\lim_{t \rightarrow \infty} \gamma = 2$) with time, t . A is a coefficient and T is the timescale governing how rapidly γ reaches saturation. The metric τ is designed to be proportional to T .

Four curves of this form are considered. The values of A and T used in each curve are presented in table D.1 and the curves are shown in Figure D.1. Curve 2 tends towards saturation over the same timescale as Curve 1 but starting from a value of γ closer to saturation. Curve 3 takes twice as

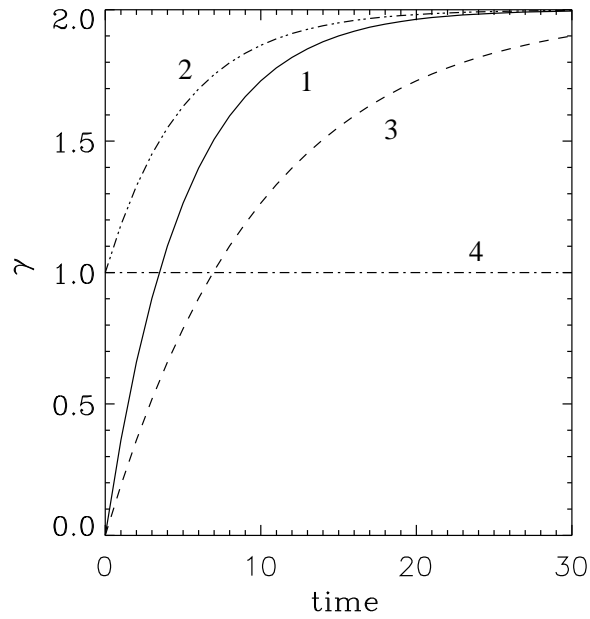


Figure D.1: γ curves used to understand τ . γ_1 (solid), γ_2 (dotted), γ_3 (dashed) and γ_4 (dot-dash).

long to saturate as Curves 1 and 2. Finally, Curve 4 describes a constant value, i.e. γ not tending towards saturation.

The first metric, S , (defined in Section 6.4.2) thus becomes,

$$\begin{aligned} S &= \int_{t_1}^{t_2} \left(2 - 2 + Ae^{-\frac{t}{T}} \right) dt \\ &= \left[A(-T) e^{-\frac{t}{T}} \right]_{t_1}^{t_2} \end{aligned}$$

When integrated over an infinite time range (i.e. $t_1 = 0$ and $t_2 = \infty$) this becomes:

$$\begin{aligned} S &= A[0 + T] \\ &= AT. \end{aligned}$$

Curve number, n	A_n	T_n
1	2.0	5.0
2	1.0	5.0
3	2.0	10.0
4	1.0	∞

Table D.1: Parameters used in test curves 1 to 4.

This is proportional to the difference between the forecasts over the time range t_1 to t_2 (or forecast skill if one of the forecasts is assumed to be the truth). Similarly, the metric τ becomes,

$$\begin{aligned}
 \tau &= \int_0^{\infty} \frac{t \left(2 - 2 + Ae^{-\frac{t}{T}} \right)}{S} dt \\
 &= \int_0^{\infty} tAe^{-\frac{t}{T}} dt / S \\
 &= A \left[-tTe^{-\frac{t}{T}} \right]_0^{\infty} + \frac{A}{S} \left[-T^2 e^{-\frac{t}{T}} \right]_0^{\infty} \\
 &= \frac{0 + AT^2}{S} \\
 &= \frac{AT^2}{AT} \\
 &= T.
 \end{aligned}$$

Therefore it can be seen that S is proportional to the initial value of γ , while τ is not. Furthermore, when integrated over an infinite time range, τ is directly proportional to the saturation timescale, T .

When integrating over a finite time (i.e. $t_2 \neq \infty$), the value of τ can become truncated and infinite values of τ are not possible. The values of τ calculated the test curves illustrate this clearly (see table D.2). The values of τ are *related* to the timescale, T , but not directly proportional to them. It can be seen that the values of τ calculated provide a good indication of the saturation timescale, with almost equal values calculated for curves 1 and 2. Curve 3 has a value of τ almost twice that of curves 1 and 2. The limiting case described by curve 4 shows that when integrating over a finite time, if γ does not tend towards saturation then $\tau = \frac{t_2 - t_1}{2}$. This must be remembered when interpreting the values of τ for the error growth curves in this thesis as it may have been assumed that a curve not tending toward saturation would have a value of τ equal to infinity. Finally, if γ tends *away* from saturation (not shown here), then τ will have a value greater than $\frac{T}{2}$.

Curve number, n	S	τ_n
1	9.98	4.96
2	4.99	4.92
3	19.00	9.22
4	30.00	15.00

Table D.2: Values of metrics, S and τ , for test curves 1 to 4.

References

- Anthes, R., Kuo, Y., Baumhefner, D., Errico, R., and Bettge, T. (1985). *Predictability of mesoscale motions*, volume 28. Academic Press.
- Betts, A. (1986). A new convective adjustment scheme. Part I: Observational and theoretical basis. *Quart. J. Roy. Meteor. Soc.*, **112**, 677–691.
- Bradley, S. and Hipkin, V. (2002). DIAS: Differential absorption of sound to obtain temperature profiles from multifrequency Sodar. *J. Atmos. Ocean. Tech.*, **19**, 1199–1202.
- Browning, K. (2005). Convective Storms Initiation Project Operations Plan. Retrieved April 2006 from: <http://www.env.leeds.ac.uk/csip/>.
- Changnon, J. and Bannon, P. (2005). Wave response during hydrostatic and geostrophic adjustment. Part I: Transient dynamics. *J. Atmos. Sci.*, **62**, 1311–1329.
- Charney, J., Fjortoft, R., and von Neumann, J. (1950). Numerical integration of the barotropic vorticity equation. *Tellus*, **2**, 237–254.
- Charney, J., Fleagle, T., Lally, V., Riehl, H., and Wark, D. (1966). The feasibility of a global observation and analysis experiment. *Bull. Amer. Meteor. Soc.*, **47**, 200–220.
- Cohen, B. (2001). *Fluctuations in an ensemble of cumulus clouds*. Ph.D. thesis, University of Reading.
- Crook, N. (1996). Sensitivity of moist convection forced by boundary layer processes to low-level thermodynamic fields. *Mon. Wea. Rev.*, **124**, 1767–1785.
- Cunning, J., Poor, H., and DeMaria, M. (1986). An investigation of the development of cumulonimbus systems over south Florida. Part II: In-cloud structure. *Mon. Wea. Rev.*, **114**, 25–39.
- Dalcher, A. and Kalnay, E. (1987). Error growth and predictability in operational ECMWF analyses. *Tellus*, **39A**, 474–491.

- Davies, T., Cullen, M., Malcolm, A., Mawson, M., Staniforth, A., White, A., and Wood, N. (2005). A new dynamical core for the Met Office's global and regional modelling of the atmosphere. *Quart. J. Roy. Meteor. Soc.*, **131**, 1759–1782.
- De Roode, S. and Duynkerke, P. (2004). Large-eddy simulation: how large is large enough? *J. Atmos. Sci.*, **61**, 403–421.
- Done, J. (2003). *Predictability and representation of convection in a mesoscale model*. Ph.D. thesis, University of Reading.
- Eady, E. (1951). *Compendium of Meteorology*, chapter The quantitative theory of cyclone development., pages 464–469. Am. Meteorol. Soc., Boston.
- Ehrendorfer, M. and Errico, R. (1995). Mesoscale predictability and the spectrum of optimal perturbations. *J. Atmos. Sci.*, **52**, 3475–3500.
- Ehrendorfer, M. and Raeder, K. (1999). Singular vector perturbation growth in a primitive equation model with moist physics. *J. Atmos. Sci.*, **56**, 1627–1648.
- Emanuel, K. (1994). *Atmospheric Convection*. Oxford University Press.
- Errico, R. and Baumhefner, D. (1987). Predictability experiments using a high resolution limited area model. *Mon. Wea. Rev.*, **115**, 488–504.
- Errico, R. and Langland, R. (1999a). Notes on the appropriateness of "bred modes" for generating initial perturbations used in ensemble prediction. *Tellus*, **51**(3), 431–441.
- Errico, R. and Langland, R. (1999b). Reply to: Comments on: "Notes on the appropriateness of "bred modes" for generating initial perturbations used in ensemble prediction". *Tellus*, **51**(3), 450–451.
- Farrell, B. (1989). Optimal excitation of baroclinic waves. *J. Atmos. Sci.*, **46**, 1193–1206.
- Gage, K. (1979). Evidence for a $k^{-5/3}$ Law Inertial Range in Mesoscale Two-Dimensional Turbulence. *J. Atmos. Sci.*, **36**, 1950–1954.
- Garratt, J. (1992). *The atmospheric boundary layer*. Cambridge University Press.
- Gerard, L. and Geleyn, J. (2005). Evolution of a subgrid deep convection parameterization in a limited-area model with increasing resolution. *Quart. J. Roy. Meteor. Soc.*, **131**, 2293–2312.

- Germann, U. and Zawadzki, I. (2002). Scale-dependence of the predictability of precipitation from continental radar images. Part I: Description of the methodology. *Mon. Wea. Rev.*, **130**, 2859–2873.
- Gilmour, I., Smith, L., and Buizza, R. (2001). Linear regime duration: is 24 hours a long time in synoptic weather forecasting? *J. Atmos. Sci.*, **58**, 3525–3539.
- Guillemin, V. (2003). *The story of quantum mechanics*, chapter Determinism, free will and the new physics. Courier Dover Publications.
- Holton, J. (2004). *An introduction to dynamic meteorology*. International Geophysical Series. Elsevier Academic Press.
- Hooper, A. (1986). WMO international radiosonde comparison Phase I, Beaufort Park, UK. In *WMO instruments and observing methods report No.28*, page 118. World Meteorol. Organiz., Geneva.
- Houze, R. (1993). *Cloud Dynamics*, volume 53 of *International Geophysical Series*. Academic Press.
- Huang, H., Smith, W., and Woolf, H. (1992). Vertical Resolution and Accuracy of Atmospheric Infrared Sounding Spectrometers. *J. App. Meteor.*, **31**, 265–274.
- Jorgensen, D. and Weckworth, T. (2003). Forcing and organization of convective systems. *Meteorological Monographs*, **30**, 75–75.
- Kaiser, G. (1999). *A friendly guide to wavelets*. Birkhauser Verlag.
- Kalnay, E., Corazza, M., and Cai, M. (2002). Are Bred vectors the same as Lyapunov vectors? AMS Symposium on Observation, Data Assimilation and Probabilistic Prediction. 13-17 January 2002, Orlando, FL. Retrieved April 2006 from: <http://www.atmos.umd.edu/~ekalnay>.
- Korb, C. and Weng, C. (1982). A theoretical study of a two-wavelength Lidar technique for the measurement of atmospheric temperature profiles. *J. App. Meteor.*, **21**, 1346–1355.
- Lacarra, J. and Talagrand, O. (1988). Short-range evolution of small perturbations in a barotropic model. *Tellus*, **40**, 81–95.
- Lander, J. and Hoskins, B. (1997). Believable Scales and Parameterizations in a Spectral Transform Model. *Mon. Wea. Rev.*, **125**, 292–303.

- Leith, C. (1965). Numerical simulation of Earth's atmosphere. In *Methods in Computational Physics*, volume 4, pages 1–28. New York, Academic Press.
- Leith, C. and Kraichnan, R. (1972). Predictability of turbulent flows. *J. Atmos. Sci.*, **29**, 1041–1058.
- Li, J., Wol, W., Menzel, W., Zhang, W., Huang, H., and Achtor, T. (2000). Global soundings of the atmosphere from ATOVS measurements: the algorithm and validation. *J. App. Meteor.*, **39**, 1248–1268.
- Lilly, D. (1983). Stratified turbulence and the mesoscale variability of the atmosphere. *J. Atmos. Sci.*, **40**, 749–761.
- Lock, A., Brown, A., Bush, M., Martin, G., and Smith, R. (2000). A new boundary layer mixing scheme. Part I: Scheme description and single-column model tests. *Mon. Wea. Rev.*, **128**, 3187–3199.
- Lorenz, E. (1963). Deterministic nonperiodic flow. *J. Atmos. Sci.*, **20**, 130–141.
- Lorenz, E. (1965). A study of the predictability of a 28-variable atmospheric model. *Tellus*, **17**, 321–333.
- Lorenz, E. (1969a). The predictability of a flow which possesses many scales of motion. *Tellus*, **21**, 130–141.
- Lorenz, E. (1969b). Three approaches to atmospheric predictability. *Bull. Amer. Meteor. Soc.*, **50**, 345–349.
- Lorenz, E. (1975). Climate predictability: the physical basis of climate modelling. *GARP Publication Series*, **16**, 132–136.
- Lorenz, E. (1982). Atmospheric predictability experiments with a large numerical model. *Tellus*, **34**, 505–513.
- Lorenz, E. (1993). *The Essence of Chaos*. University College London Press.
- Luers, J. (1997). Temperature error of the Vaisala RS90 radiosonde. *J. Atmos. Ocean. Tech.*, **14**, 1520–1532.
- Marsham, J. and Parker, D. (2006). Secondary initiation of multiple bands of cumulonimbus over southern Britain. Part II: Dynamics of secondary initiation. *Quart. J. Roy. Meteor. Soc.*, **132**, 1053–1072.

- May, B., Clark, P., Cooper, A., Forbes, R., Golding, B., Hand, W., Lean, H., Pierce, C., Roberts, N., and Smith, R. (2004). Flooding at Boscastle, Cornwall on 16 August 2004 - A study of Met Office Forecasting Systems. Forecasting Research Technical Report 429, Met Office Forecasting Research.
- Menzel, W., Holt, F., Schmit, T., Aune, R., Schreiner, A., Wade, G., and Gray, D. (1998). Application of GOES-8/0 soundings to weather forecasting and nowcasting. *Bull. Amer. Meteor. Soc.*, **79**(10), 2059–2077.
- Met.Office (1997). *Source book to the forecaster's reference book*, chapter 5. HMGSO.
- Mintz, Y. (1964). Very long-term global integration of the primitive equations of atmospheric motion. Technical Report 66, WMO.
- Molteni, F., Buizza, R., Palmer, T., and T., P. (1996). The ECMWF ensemble prediction system : Methodology and validation. *Quart. J. Roy. Meteor. Soc.*, **122**(529), 73–119.
- Moore, G. (1965). Cramming more components onto integrated circuits. *Electronics Magazine*.
- Newton, I. (1687). *Philosophiae Naturalis Principia Mathematica*. London.
- Petch, J. (2004). The predictability of deep convection in cloud-resolving simulations over land. *Quart. J. Roy. Meteor. Soc.*, **130**, 3179–3187.
- Petch, J., Brown, A., and Gray, M. (2002). The impact of horizontal resolution on the simulations of convective development over land. *Quart. J. Roy. Meteor. Soc.*, **128**, 2031–2044.
- Poincaré, H. (1914). *Science and Method*, chapter Chance. Nelson.
- Roberts, N. (2000a). A guide to aspects of water vapour imagery interpretation: the significance of dry regions. NWP Technical Report 294, Met Office Forecasting Research.
- Roberts, N. (2000b). The relationship between water vapour imagery and thunderstorms. NWP Technical Report 300, Met Office Forecasting Research.
- Roberts, N. (2003). Stage 1 report from the Storm-Scale numerical modelling project. Technical Report 402, Met Office Forecasting Research.
- Schubert, D. and Suarez, M. (1989). Dynamical predictability in a simple general circulation model: average error growth. *J. Atmos. Sci.*, **46**, 353–370.

- Shi, L. (2001). Retrieval of atmospheric temperature profiles from AMSU-A measurement using a neural network approach. *J. Atmos. Ocean. Tech.*, **18**, 340–347.
- Smagorinsky, J. (1963). General circulation experiments with the primitive equations. I. The basic experiment. *Mon. Wea. Rev.*, **91**, 99–164.
- Smagorinsky, J. (1969). Problems and promises of deterministic extended range forecasting. *Bull. Amer. Meteor. Soc.*, **50**, 286–311.
- Smith, R. (1990). A scheme for predicting layer clouds and their water content in a general circulation model. *Quart. J. Roy. Meteor. Soc.*, **116**, 435–460.
- Staniforth, A., White, A., Wood, N., Thuburn, J., Zerroukat, M., Cordero, E., and Davies, T. (2003). Joy of UM5.5 - Model Formulation. Unified Model Documentation Paper 15, Met Office Forecasting Research.
- Stein, E. and Shakarchi, R. (2003). *Fourier analysis: An Introduction (Princeton Lectures in Analysis S.)*. Princeton University Press.
- Stirling, A. and Petch, J. (2004). The impacts of spatial variability on the development of convection. *Quart. J. Roy. Meteor. Soc.*, **130**, 3189–3206.
- Stroe, R. and Royer, J. (1993). Comparison of different error growth formulas and predictability estimation in numerical extended-range forecasts. *Ann. Geophysicae*, **11**, 296–316.
- Tan, Z., Zhang, F., Rotunno, R., and Snyder, C. (2004). Mesoscale predictability of moist baroclinic waves: Experiments with parameterized Convection. *J. Atmos. Sci.*, **61**, 1794–1804.
- Thompson, P. (1957). Uncertainty of initial state as a factor in the predictability of large scale atmospheric flow patterns. *Tellus*, **9**, 275–295.
- Toth, Z. and Kalnay, E. (1993). Ensemble forecasting at NMC - The generation of perturbations. *Bull. Amer. Meteor. Soc.*, **74**(12), 2317–2330.
- Toth, Z. and Kalnay, E. (1997). Ensemble forecasting at NCEP and the breeding method. *Mon. Wea. Rev.*, **125**(12), 3297–3319.
- Toth, Z., Szunyogh, I., Kalnay, E., and Iyengar, G. (1999). Comments on: "Notes on the appropriateness of "bred modes" for generating initial perturbations used in ensemble prediction". *Tellus*, **51**(3), 442–449.

- Tribbia, J. and Baumhefner, D. (2004). Scale interactions and Atmospheric Predictability: An Updated Perspective. *Mon. Wea. Rev.*, **132**, 703–713.
- Vallis, G., Shutts, G., and Gray, M. (1997). Balanced mesoscale motion and stratified turbulence forced by convection. *Quart. J. Roy. Meteor. Soc.*, **123**, 1621–1652.
- Vukicevic, T. and Errico, R. (1990). The influence of artificial and physical factors upon predictability estimates using a complex limited-area model. *Mon. Wea. Rev.*, **118**, 1460–1482.
- Weckworth, T. (2000). The effect of small-scale moisture variability on thunderstorm initiation. *Mon. Wea. Rev.*, **128**, 4017–4030.
- Weckworth, T., Horst, T., and Wilson, J. (1999). An observational study of the evolution of horizontal convective rolls. *Mon. Wea. Rev.*, **127**, 2160–2179.
- Weisman, M., Skamarock, W., and Klemp, J. (1997). The resolution dependence of explicitly modeled convective systems. *Mon. Wea. Rev.*, **125**, 527–548.
- Wilson, D. and Ballard, S. (1999). A microphysically based precipitation scheme for the UK Meteorological Office Unified Model. *Quart. J. Roy. Meteor. Soc.*, **125**, 1607–1636.
- Wilson, J. and Schreiber, W. (1986). Initiation of convective storms at radar-observed boundary-layer convergence lines. *Mon. Wea. Rev.*, **114**, 2516–2536.
- WMO (1983). *Guide to meteorological instruments and methods of observation*. World Meteorol. Organiz., Geneva, 5th edition. WMO-No.8.
- Zhang, F., Snyder, C., and Rotunno, R. (2002). Mesoscale predictability of the “surprise” snowstorm of 24-25 January 2000. *Mon. Wea. Rev.*, **130**, 1617–1632.
- Zhang, F., Snyder, C., and Rotunno, R. (2003). Effects of moist convection on mesoscale predictability. *J. Atmos. Sci.*, **60**, 1173–1185.